INVESTIGATION OF GASEOUS SECONDARY INJECTION THRUST VECTOR CONTROL CONSIDERING PRIMARY NOZZLE OVEREXPANSION, FREQUENCY RESPONSE, AND INJECTION ANGLE

N 68-17081

(ACCESSION NUMBER)   (THRU)

(PAGES)   (CODE)

CR-66533

(NASA CR OR TMX OR AD NUMBER)   (CATEGORY)

FACILITY FORM 602

INVESTIGATION OF GASEOUS SECONDARY INJECTION THRUST VECTOR

CONTROL CONSIDERING PRIMARY NOZZLE OVEREXPANSION,

FREQUENCY RESPONSE, AND INJECTION ANGLE

JANUARY, 1968

LANGLEY RESEARCH CENTER

NATIONAL AERONAUTICS AND SPACE ADMINISTRATION

ABSTRACT

The performance characteristics of gaseous secondary injection thrust vector control in overexpanded primary nozzles are investigated under sea-level conditions. Nitrogen gas is used in both the primary and secondary systems. Four interchangeable primary nozzles with 6.79, 10.72, 16.56, and 25.00 area ratios provide a wide range of test conditions. Data plots incorporating the effects of total and differential flow rates from two opposed injection nozzles provide criteria for predicting performance of a vehicle whose primary nozzle is overexpanded relative to the ambient pressure.

Frequency response and injection angle characteristics are determined for secondary injection thrust vector control in a primary nozzle with sea-level expansion.

FOREWORD

This report describes the results of the work accomplished

under NASA Contract NAS 1-7154 entitled "Investigation of

Gaseous Secondary Injection Thrust Vector Control Consider-

ing Primary Nozzle Overexpansion, Frequency Response, and

Injection Angle". The test data obtained serves to extend

the information obtained under previous contracts (NAS 1-2962

and NAS 1-4102).

The contract was performed at the Troy, Michigan, facility of

the Vickers Division of Sperry Rand Corporation under the

technical cognizance of Mr. John Riebe, Langley Research

Center.

TABLE OF CONTENTS

LIST OF FIGURES

NOMENCLATURE

Symbol	Definition	Units
A_e	Primary nozzle exit area	m^2
A_{j*}	Injection nozzle throat area	m^2
A_j	Injection nozzle exit area	m^2
A_o	Area of primary nozzle in plane of injection	m^2
A_*	Nozzle throat area	m^2
D_e	Diameter of primary nozzle in exit plane	m
D_o	Diameter of primary nozzle at plane of injection	m
F	Axial thrust of system	n
F_j	Measured side force	n
g	Gravitational constant	m/sec^2
h	Accommodation height: distance of penetration of the secondary jet perpendicular to the primary nozzle axis in the plane of the injectors	m
I	Primary specific impulse	sec
I_j	Injectant gas specific impulse	sec
L_o	Distance from injection plane to nozzle exit plane parallel to nozzle axis	m
M_e	Primary nozzle exit Mach number	
M_j	Injection nozzle Mach number	

Symbol	Definition	Units
M_o	Primary stream Mach number at injection plane	
$\dot{m}$	Primary gas mass flow rate	kg/sec
$\dot{m}_j$	Mass flow rate through one injection nozzle	kg/sec
$\Delta\dot{m}_j$	Differential injection nozzle flow	kg/sec
$\dot{m}_{jt}$	Total secondary system mass flow rate in tests using two injection ports	kg/sec
nsma	Abbreviation for pressure unit of newtons per square meter absolute	
P	Pressure	nsma
P_a	Ambient pressure	nsma
P_c	Primary chamber pressure	nsma
P_e	Theoretical exit pressure for full-flowing nozzle	nsma
P_j	Injection nozzle exit pressure	nsma
P_{jc}	Injection nozzle chamber pressure	nsma
ΔP_{jc}	Difference in injector chamber pressure	nsma
P_o	Primary stream pressure at plane of injection port	nsma
P_s	Boundary layer separation pressure	nsma
$\bar{P}_s$	Average pressure in separated region	nsma

Symbol	Definition	Units
R	Gas constant	m/°K
T	Gas total temperature	°K
X/L	Throat to injection plane distance divided by throat to exit plane distance	
α	Primary nozzle half-angle	degrees
γ	Specific heat ratio	
ε	Angle between injection nozzle centerline and a line perpendicular to the motor nozzle axis - upstream angle defined as positive	degrees
θ	Shock angle	degrees
Φ_e	Azimuth of shock on nozzle wall at exit plane	degrees
Φ_o	Azimuth of shock on nozzle wall in injection plane	degrees
ψ	Effective shock angle along nozzle wall	degrees

SECTION 1

INTRODUCTION

1.1 Program Objectives

The primary objective of this investigation was to gain a better qualitative and quantitative understanding of secondary injection thrust vectoring in overexpanded primary nozzles. Data obtained under a number of overexpansion conditions using nitrogen gas in both primary and secondary systems can provide design criteria for adapting separated-flow secondary injection thrust vector control (SITVC) to operational vehicles.

The program also had two secondary objectives. First was an investigation of the dynamics of SITVC by frequency response testing. Second was an investigation of the effects on the thrust vectoring force produced by varying the angle of the injection nozzles. Both of these investigations were performed in sea-level nozzles with nitrogen gas used in both primary and secondary systems.

1.2 Previous Testing

Under contract NAS 1-4102 with NASA Langley, three tests of warm gas SITVC were conducted under simulated altitude conditions at

the Allegany Ballistics Laboratory. During portions of each test, the pressure within the altitude cabin rose above the design limits. When this occurred, the primary nozzle became overexpanded relative to ambient conditions, and the primary flow separated from the nozzle wall. The specific impulse measured for the secondary system under separated-flow conditions was significantly greater than that obtained when the primary nozzle was flowing full.

The potential benefits of this increase in SITVC specific impulse warranted further study of separated-flow systems. Greater specific impulse would be obtained at the lower altitudes when the primary nozzle is highly overexpanded. The fuel weight saved by using a separated-flow SITVC system at the lower altitudes would allow use of an overexpanded primary nozzle which, in turn, becomes more efficient with increasing altitude. Proper matching of primary and secondary systems could reduce the number of stages in a vehicle.

1.3 Description of Experimental Hardware

In an effort to verify and expand the separated-flow results of NAS 1-4102 testing, experimental hardware was designed to represent a wide range of overexpansion conditions. The

primary nozzle on which all three-dimensional testing for this program was performed consisted of a single mixing chamber and four interchangeable nozzle extensions. The primary nozzle (throat diameter = 0.739 inch = 0.01877 meter) passed a nominal 6 lb/sec (2.72 kg/sec) of nitrogen gas at 600 psia (4.14×10^6 nsma) chamber pressure. Each primary nozzle extension contained two opposed secondary injectors at an X/L location of 0.75. In each extension ten pressure taps were located in the nozzle wall. Each secondary nozzle (throat diameter = 0.234 inch = 0.00594 meter) passed a nominal 0.6 lb/sec (0.272 kg/sec) of nitrogen gas at 600 psia (4.14×10^6 nsma) chamber pressure. Injector exit areas were sized to match exhaust pressure to the expected pressure under the shock in the primary nozzle when the injector was passing 0.3 lb/sec (0.136 kg/sec) of nitrogen gas. Other system parameters are given in Figure 1.1.

The primary and secondary systems were mounted on a thrust stand capable of measuring axial thrust and side force in the plane of injection. Nitrogen flow to the injectors was controlled by a proportional pneumatic valve mounted on the base of the stand. Photographs of the thrust stand assembly are presented in Figures 1.2 and 1.3.

In addition to the three-dimensional testing, a two-dimensional model of gaseous SITVC in an overexpanded nozzle was constructed. The flow structure in this model was photographed with Schlieren equipment. Different degrees of overexpansion were simulated by varying the primary chamber pressure. Schlieren test conditions and photographs are presented in Section 4.1.

1.4 Test Program

A total of ninety-eight tests were performed. Tests 1 to 84 (see Figure 1.4) provide the inter-relationships of side force, primary nozzle overexpansion, total secondary system gas flow, and differential gas flow between the opposed injectors. Tests 85 to 98 are listed in Figure 1.5. Tests 85 to 87 determine the frequency response characteristics of the TVC fluid mechanism. Tests 88 to 98 employed a number one primary nozzle extension modified to hold a single swivelled injector. Effects on side force of varying the injection angle can be studied under sea-level conditions.

In tests in which nitrogen was flowing through both injection ports, the command signal to the proportional valve was provided by the tape-recorded program shown in Figure 1.6. For single-port tests, step and ramp signals were applied manually.

Outputs from all pressure transducers, load cells, and turbine flowmeters were recorded on an oscillograph for all tests. Oscillograph paper speed for the frequency response tests was 0.1 meter per second; for other tests a 0.01 meter per second paper speed was used.

The test program was performed at the Vickers Administrative and Engineering Center in Troy, Michigan.

FIGURE 1.1 - SYSTEM PARAMETERS

	1	2	3	4
Primary nozzle extension				
Theoretical exit Mach number with full-flowing primary stream, M_e	3.5	4.0	4.5	5.0
Primary exit/throat area ratio, A_e/A^*	6.79	10.72	16.56	25.00
Primary exit diameter, D_e (m)	0.0489	0.0615	0.0765	0.0940
Theoretical full-flowing primary exit/chamber pressure ratio, P_e/P_c	0.01311	0.00659	0.00346	0.00189
Full-flowing P_e (given $P_c = 4.14 \times 10^6$ nsma), (nsma)	54,200	27,300	14,310	7,820
Ratio of atmospheric pressure to P_e:				
P_e/P_a (given $P_c = 4.83 \times 10^6$ nsma)	0.641	0.323	0.1698	0.0926
P_e/P_a (given $P_c = 4.14 \times 10^6$ nsma)	0.535	0.269	0.1414	0.0772
P_e/P_a (given $P_c = 3.45 \times 10^6$ nsma)	0.459	0.230	0.1212	0.0661
Injector exit Mach number, M_j	2.03	2.40	2.77	3.14
Injector exit/throat area ratio, A_j/A_j^*	1.736	2.40	3.40	4.84
Injector exit diameter, D_j (m)	0.00782	0.00919	0.01095	0.01308
Injector exit/chamber pressure ratio, P_j/P_{jc}	0.1215	0.0687	0.0387	0.0221

Primary and secondary expansion angles: 15°   Injector X/L location: 0.75 $\varepsilon = 0°$
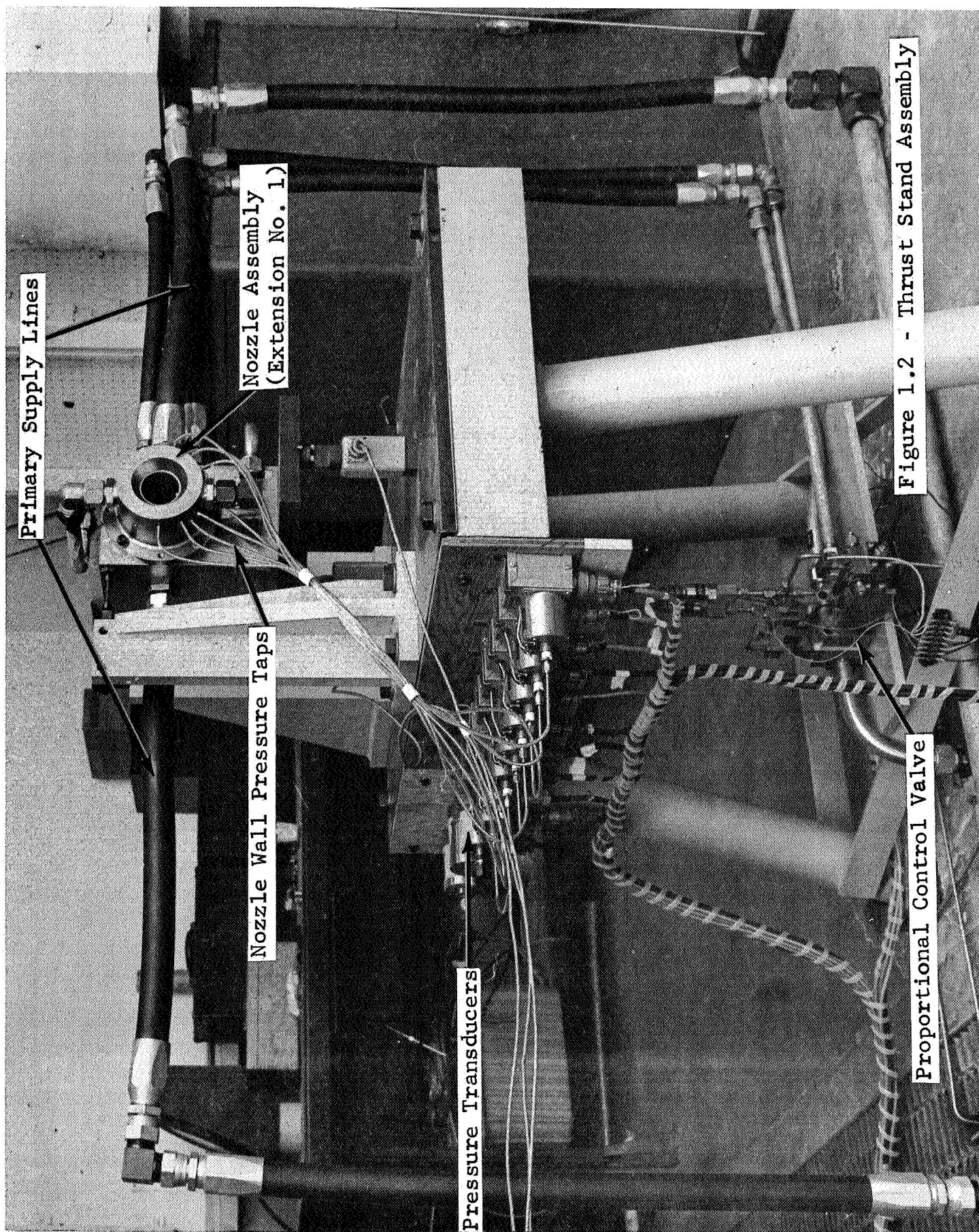
Primary Supply Lines

Nozzle Assembly
(Extension No. 1)

Nozzle Wall Pressure Taps

Pressure Transducers

Proportional Control Valve

Figure 1.2 – Thrust Stand Assembly

Secondary Injector Axis

Secondary Injector Supply Lines

Yaw Stabilizing Flexure

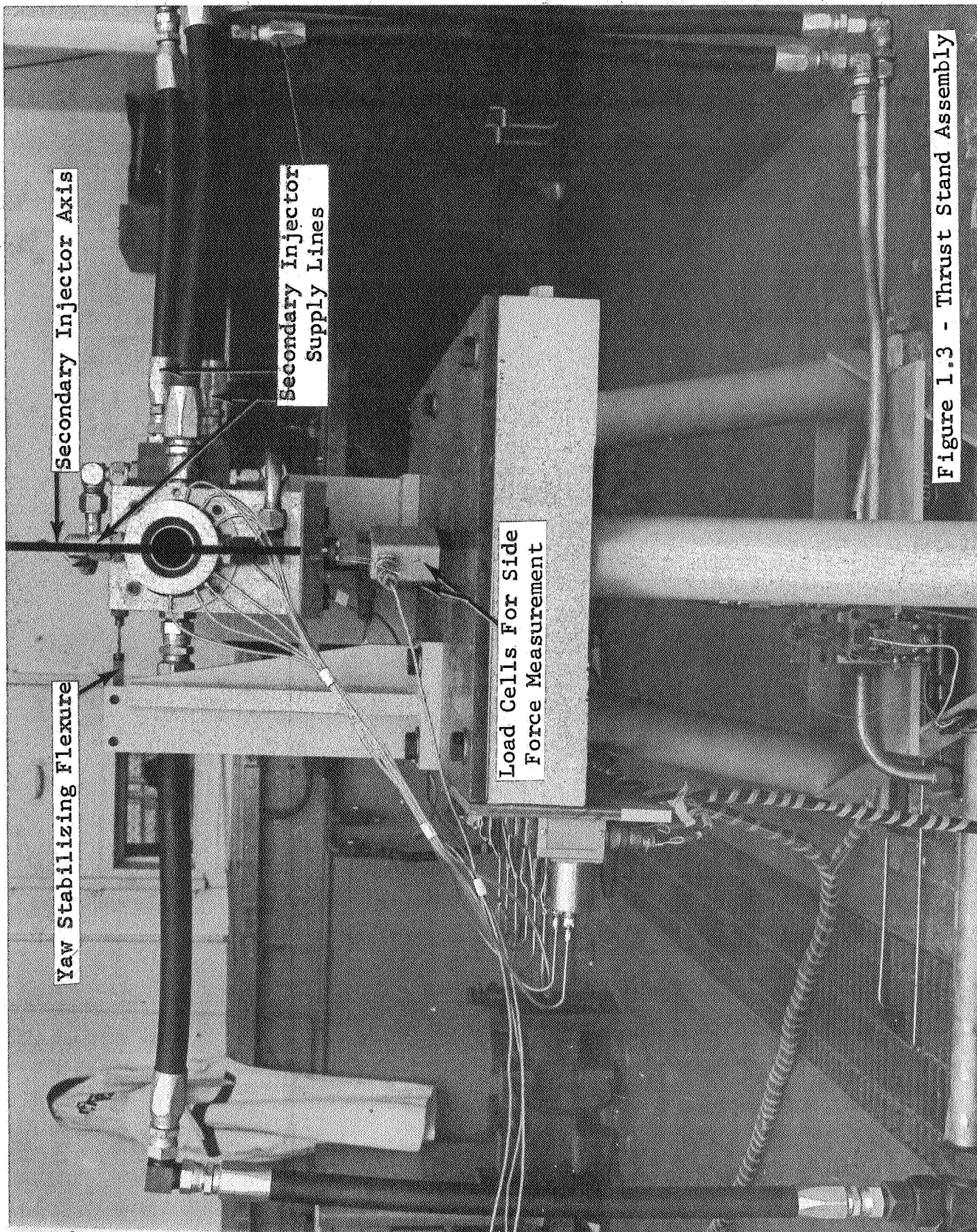Load Cells For Side Force Measurement

Figure 1.3 - Thrust Stand Assembly

1-8

FIGURE 1.4 - SEPARATED-FLOW TEST CONDITIONS

Test	Extension	Primary Flow (kg/sec.)	Total Secondary Flow (kg/sec.)
1	1	3.18	.272
2	1	3.18	.227
3	1	3.18	.181
4	1	3.18	.136
5	1	3.18	.091
6	1	3.18	.045
7	1	2.72	.272
8	1	2.72	.227
9	1	2.72	.181
10	1	2.72	.136
11	1	2.72	.091
12	1	2.72	.045
13	1	2.27	.272
14	1	2.27	.227
15	1	2.27	.181
16	1	2.27	.136
17	1	2.27	.091
18	1	2.27	.045
19*	1	3.18	0-0.272
20*	1	2.72	0-0.272
21*	1	2.27	0-0.272

Tests 22-42:   Same as Tests 1-21 except using extension 2.
Tests 43-63:   Same as Tests 1-21 except using extension 3.
Tests 64-84:   Same as Tests 1-21 except using extension 4.

* Tests to be performed with one injection port blocked and
  the flow to the other port varied.

FIGURE 1.5 - FREQUENCY RESPONSE AND VARIED
INJECTION ANGLE TEST CONDITIONS

Test	Extension	Primary Flow (kg/sec.)	Total Secondary Flow (kg/sec.)	Special Condition
85	1	2.72	.272	Frequency Response
86	1	2.72	.181	Frequency Response
87	1	2.72	.091	Frequency Response
88*	1	2.72	0-0.272	30° Downstream Injection Angle
89*	1	2.72	0-0.272	22½° Downstream Injection Angle
90*	1	2.72	0-0.272	15° Downstream Injection Angle
91*	1	2.72	0-0.272	7½° Downstream Injection Angle
92*	1	2.72	0-0.272	0° Injection Angle
93*	1	2.72	0-0.272	7½° Upstream Injection Angle
94*	1	2.72	0-0.272	15° Upstream Injection Angle
95*	1	2.72	0-0.272	22½° Upstream Injection Angle
96*	1	2.72	0-0.272	30° Upstream Injection Angle
97*	1	2.72	0-0.272	37½° Upstream Injection Angle
98*	1	2.72	0-0.272	45° Upstream Injection Angle

* Tests to be performed with one injection port blocked and
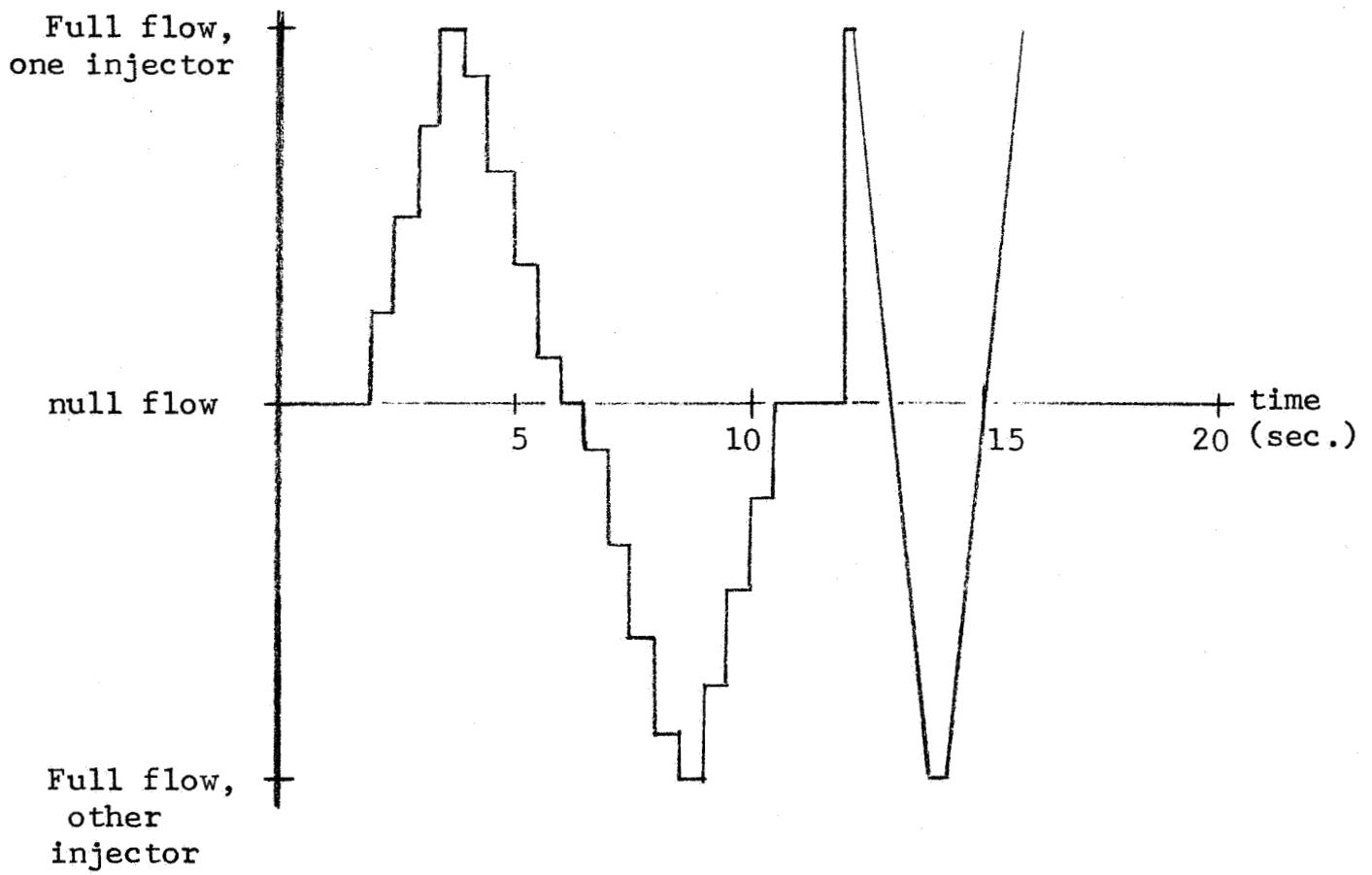the flow to the other port varied.

Figure 1.6   Command Signal to Proportional Valve

SECTION 2

THEORETICAL ANALYSIS

2.1 Calculation of Accommodation Height

The first step in analyzing a SITVC system is calculation of
the accommodation height. The accommodation height, h, is
defined as the distance of penetration of the secondary jet
perpendicular to the primary nozzle axis in the plane of the
injectors. The approach used in calculating h begins with pri-
mary and secondary flow and momentum equations across the plane
of the injectors. For identical primary and secondary gases:

$$M_o A_o P_o \sqrt{1+\tfrac{1}{2}(\gamma-1) M_o^2} = M_3 A_3 P_3 \sqrt{1+\tfrac{1}{2}(\gamma-1) M_3^2}$$

$$M_j A_j P_j \sqrt{1+\tfrac{1}{2}(\gamma-1) M_j^2} = M_4 A_4 P_4 \sqrt{1+\tfrac{1}{2}(\gamma-1) M_4^2}$$

$$P_o A_o (1+\gamma M_j^2) = P_3 A_3 (1+\gamma M_3^2) + \bar{P}_s A_4$$

$$\bar{P}_s A_4 = P_4 A_a (1+\gamma M_4^2)$$

The subscripts refer to the following flow conditions:

   o, primary stream at injection plane with no injection

   3, primary stream at injection plane with injection

   4, secondary stream at injection plane

j, secondary stream at injector exit

The average pressure in the separation region, $\bar{P}_s$, is approximated as

$$\bar{P}_s \cong \frac{1}{3}\,(P_j + 2P_s),$$

where separation pressure P_s is obtained as a function of M_o, P_o, and γ from oblique conical shock tables.

By geometry

$$A_o = A_3 + A_4,$$

and as a boundary condition approximation

$$P_3 \cong P_4.$$

This provides a system of seven equations with seven unknowns $(M_3, A_3, P_3, M_4, A_4, P_4, \bar{P}_s)$, which can be solved for A_4. With an additional approximation that the secondary flow area is a half-circle, $h = \sqrt{\dfrac{2A_4}{\pi}}$.

This approach was applied to the test conditions obtained in three-dimensional testing. Representative results obtained for 4.14×10^6 nsma primary chamber pressure and 2.72 kg/sec nitrogen flow rate are:

Extension No.	1	2	3	4	
h, at $\dot{m}_j$ = 0.136 kg/sec	0.01410	0.01872	0.0255	0.0319	meter
h, at $\dot{m}_j$ = 0.272 kg/sec	0.01788	0.0224	0.0299	0.0396	meter

A sizing procedure for the injection nozzles is implied in the set of equations presented above. For any given primary system, values of M_O and P_O can be used to obtain P_S directly from oblique conical shock tables. In order to match the injectors to the separation pressure under the shock, the injector exit pressure, P_j, is set equal to P_S by obtaining the proper combination of secondary chamber pressure and exit Mach number.

2.2 Determination of Shock Location

When the gas from the secondary system is injected into the primary stream, an oblique shock is produced. Pressures on the primary nozzle wall under this shock both upstream and downstream of the injection port are increased. This provides a significant addition to the side force produced by the momentum of the injected gas. For this reason, the injector should be located as far upstream as possible in order to increase the area under the shock. The limitation to upstream injector placement is the azimuth of the shock on the nozzle wall at the exit plane. When this azimuth (Φ_e in Figure 2.1)

approaches or exceeds 90°, a large portion of the excess pressure distribution under the shock is either wasted on a portion of the wall at right angles to the desired direction of side force or even creates a negative side force component. A design selection of Φ_e equal to 75 or 80 degrees at the maximum injector flow rate is desirable. This provides a small safety factor in case the actual TVC system produces a Φ_e greater than the design value.

An empirically determined equation (See referenced Vickers reports, particularly NAS 1-4102 Phase I report.) for exit plane shock azimuth is

$$\Phi_e = 2 \arcsin \left[\frac{L_o}{D_e} \tan (\psi - \alpha) + \frac{L_o}{D_e} \tan \alpha + \frac{D_o}{D_e} \sin \frac{\Phi_o}{2} \right]$$

where L_o is the axial distance from injection plane to primary exit plane, D_e is the primary nozzle exit diameter, ψ is the effective shock angle along the wall (approximately 7° greater than the oblique shock, α is the 15° expansion half-angle, D_o is the primary nozzle diameter at the injection plane, and Φ_o is the shock azimuth in the injection plane. The Φ_o shock azimuth is approximated as

$$\Phi_o \cong 2 \arcsin \frac{h}{D_o} + 7°$$

where h is the secondary jet accommodation height whose method

of computation is shown in Section 2.1.

This method of determining the shock outline assumes that the secondary jet presents an effective half-circle of obstruction (with radius h) to the primary stream. Experimental evidence has shown that an additional "filling" effect along the nozzle wall extends the shock influence another 7°. Under full-flowing conditions in the primary stream, this flow structure is maintained through to the primary exit plane (see Figure 2.1). Under moderate separated-flow conditions, this basic flow structure still exists. As the degree of separation increases, new flow structures may develop.

An X/L location of 0.75 (see definition of X/L ratio in Nomenclature) was used for the injectors in all four primary nozzle extensions. Application of the shock equations given above produced the following results.

extension	$\dot{m}_j$ (kg/sec)	Φ_o (deg.)	Φ_e (deg.)
1	0.136	47.2	62.2
1	0.272	57.0	73.2
2	0.136	49.8	68.5
2	0.272	58.6	76.4
3	0.136	54.2	75.0
3	0.272	64.2	84.0
4	0.136	57.0	79.0
4	0.272	70.6	91.7

2.3   Thrust Calculations

For a full-flowing nozzle, the axial thrust can be calculated by the equation

$$F = A_e(M_e^2 \gamma P_e + P_e - P_a) .$$

With 6 lb/sec (2.72 kg/sec) of nitrogen gas flowing through extension 1, theoretical F is 373 lb (1659 newtons). In extensions 2, 3, and 4, primary flow separates from the wall. The efficiency loss caused by flow separation reduces the expected thrust to a value below 373 lb.

In tests employing warm gas injection into the hot gas stream of a solid propellant rocket motor, the TVC side force per injector can be calculated by the equation

$$F_j = \frac{2\dot{m}_j M_j}{\cos \varepsilon} \sqrt{\frac{g\gamma RT}{1 + \frac{1}{2}(\gamma - 1) M_j^2}} \qquad\qquad 0 \leq \varepsilon \leq 30° .$$

This equation is merely the injector momentum equation multiplied by $2/\cos \varepsilon$. The factor of 2 reflects the magnification of side thrust brought about by the TVC phenomenon. The $\cos \varepsilon$ term reflects the increase in side thrust as the secondary gas is injected upstream.

2-6

With secondary injection, a nitrogen flow rate of 0.6 lb/sec (0.272 kg/sec), injection angle $\varepsilon = 0°$, and secondary total temperature of 40°F (278°K), the calculated value of F_j for extension 1 is 62.5 lb (278 newtons). Calculated specific impulse is 104 seconds.

Side force produced under the separated flow conditions encountered in extensions 2, 3, and 4 cannot be calculated with the F_j equation. The primary objective of this program is to determine the separated-flow SITVC forces experimentally.

main shock with conical angle θ

nozzle exit plane

Φ_e
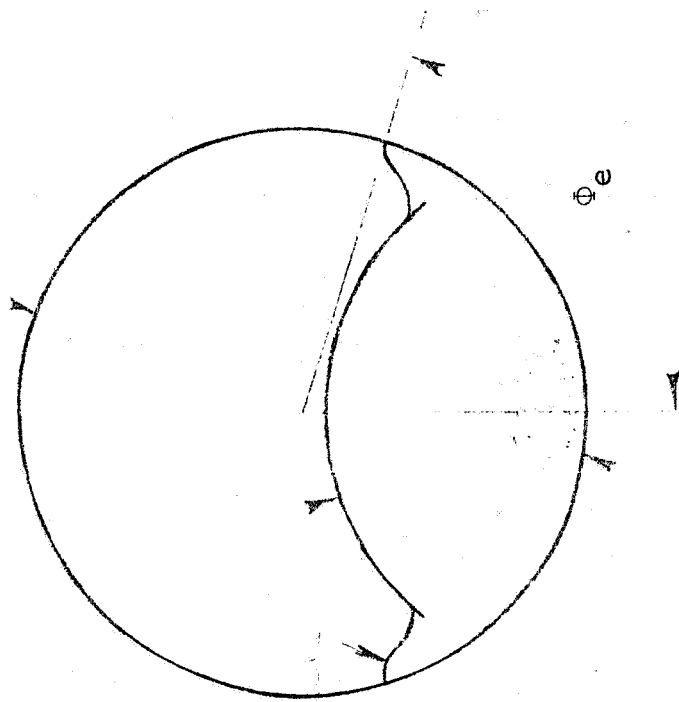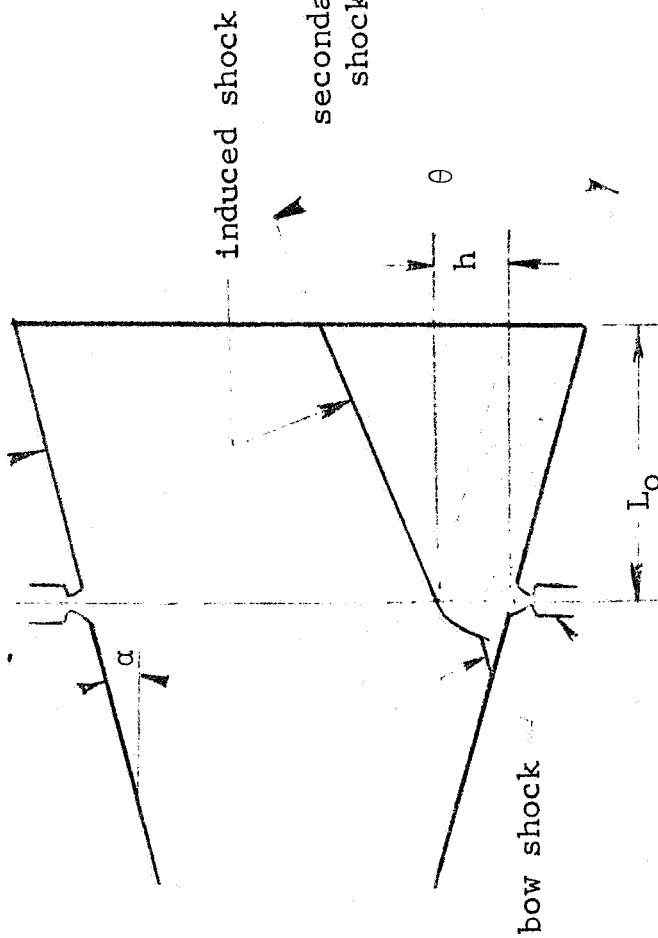
inner core of secondary gas

primary nozzle

induced shock

secondary shock

θ

h

L_o

injection nozzle

bow shock

α

Figure 2.1 SITVC Shock Structure

2-8

SECTION 3

TEST RESULTS: THRUST MEASUREMENTS

3.1 Opposed Injector Testing

Of the 98 tests in the entire program, 72 of these were performed with the thrust vector control flow coming from two opposed injection ports. Results of these tests are presented in Figures 3.1 through 3.18. Each figure presents the data obtained for the four nozzle extensions under nominally identical primary and secondary flow rates and chamber pressures. The data points were obtained at various steps commanded of the TVC system by the tape-recorded input program (Figure 1.6). Data points obtained for steps of increasing differential secondary flow are differentiated from those of decreasing differential flow. In drawing curves through the data points for each test, consideration was given to the shape of the TVC force oscillograph traces relative to the injector chamber pressures during the ramp portion of the input program.

As would be expected, a good deal of scatter is sometimes found in the I_j data points at the low differential flow levels. Since

$$I_j = \frac{F_j}{g \, \Delta \dot{m}_j} \quad ,$$

the limitation on precision in measuring or calculating dif-
ferential flow and side force when both are near zero can
cause large percentage variations in I_j.

For all tests shown in Figures 3.1 through 3.18, a value for
the pressure ratio P_e/P_a is given. In this ratio, P_e is a
theoretical value for primary stream exit pressure when the
primary stream is flowing full. In most of the tests the pri-
mary stream was separated from the nozzle wall, but use of this
theoretical P_e value in a ratio with measured atmospheric
pressure P_a provides a scale by which relative overexpansion
can be measured. Each secondary flow condition was tested in
four primary nozzle extensions at three different primary
chamber pressures. Thus twelve values of P_e/P_a are available
for each secondary condition.

The data for the secondary flow conditions are plotted in a
non-dimensionalized form of specific impulse ratio, I_j/I,
versus P_e/P_a in Figures 3.19 through 3.30. This plotting for-
mat simulates the specific impulse characteristics for a given
SITVC system in an ascending vehicle (theoretical full-flowing
P_e is constant, P_a decreases, therefore P_e/P_a increases with
altitude). Two sets of specific impulse characteristics are

presented. In the first set (Figures 3.19 through 3.24), a family of curves for various differential flows are given for the six total secondary flow rates tested. Differential and total secondary flow data are presented as ratios to primary flow in order to simplify application of the curves to other systems. As can be seen in Figure 3.19 for example, the curves for the lower differential flows coincide over the entire range of overexpansion. For the same total secondary flow rate, the curves for higher differential flows fall below the others at the lower values of P_e/P_a. In the second set (Figures 3.25 through 3.30), curve families of total flow rate are presented for each of six differential rates.

3.2 Single Port Testing

Twelve tests were run with one of the two injection ports blocked to make sure that the separated-flow side forces were not affected by interaction of the primary stream with any leakage flow from the second injector. Individual curves for each test are plotted in Figures 3.31, 3.32, and 3.33 in a manner similar to that of the opposed port tests. Each of these tests produced a relatively constant secondary specific impulse over the secondary flow range. When the I_j/I ratio for each of the twelve tests is plotted according to its

P_e/P_a ratio, the curve given in Figure 3.34 results.

3.3 Axial Thrust

Average values for specific impulse produced by the primary

thrust for each extension are as follows:

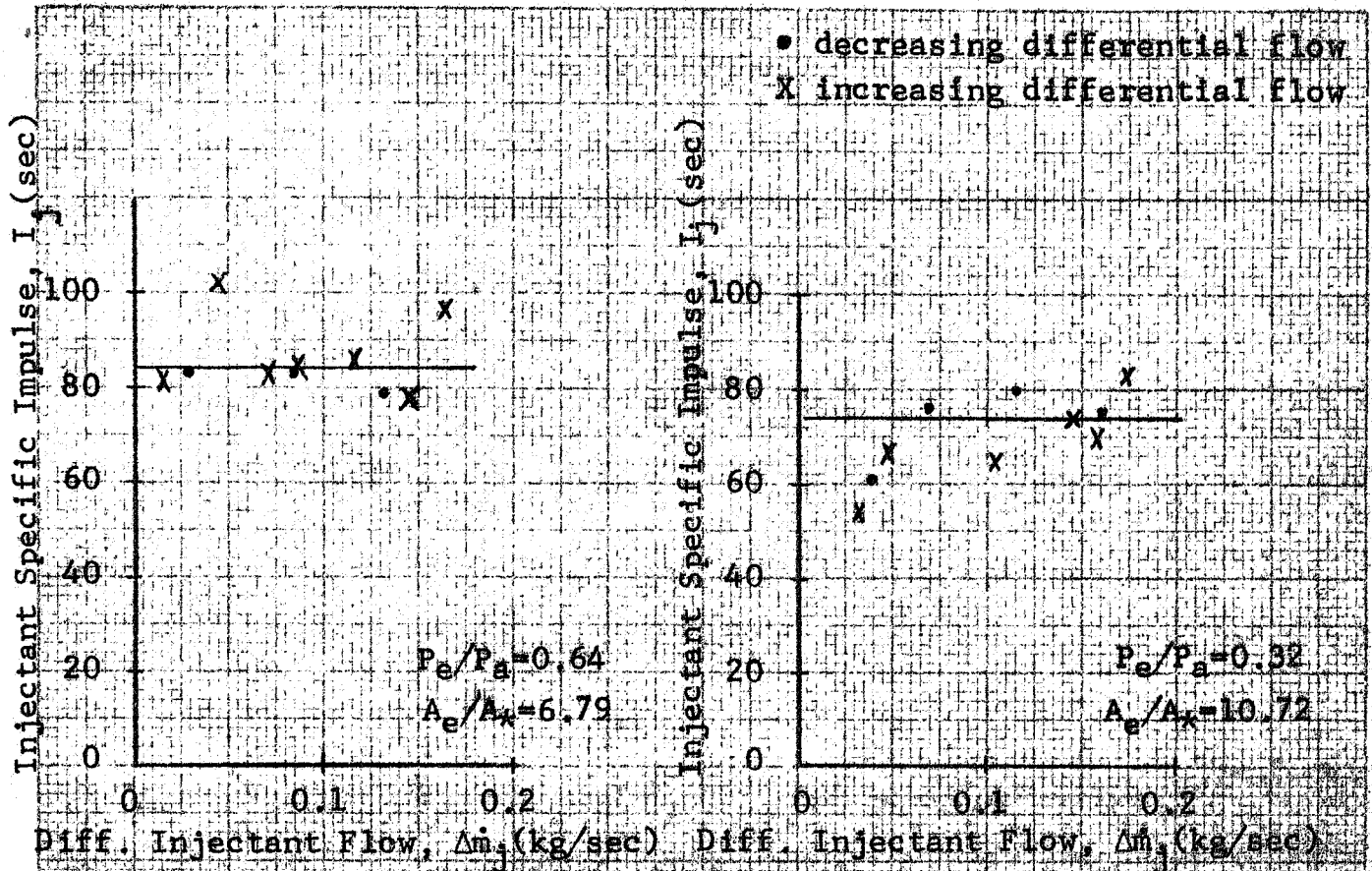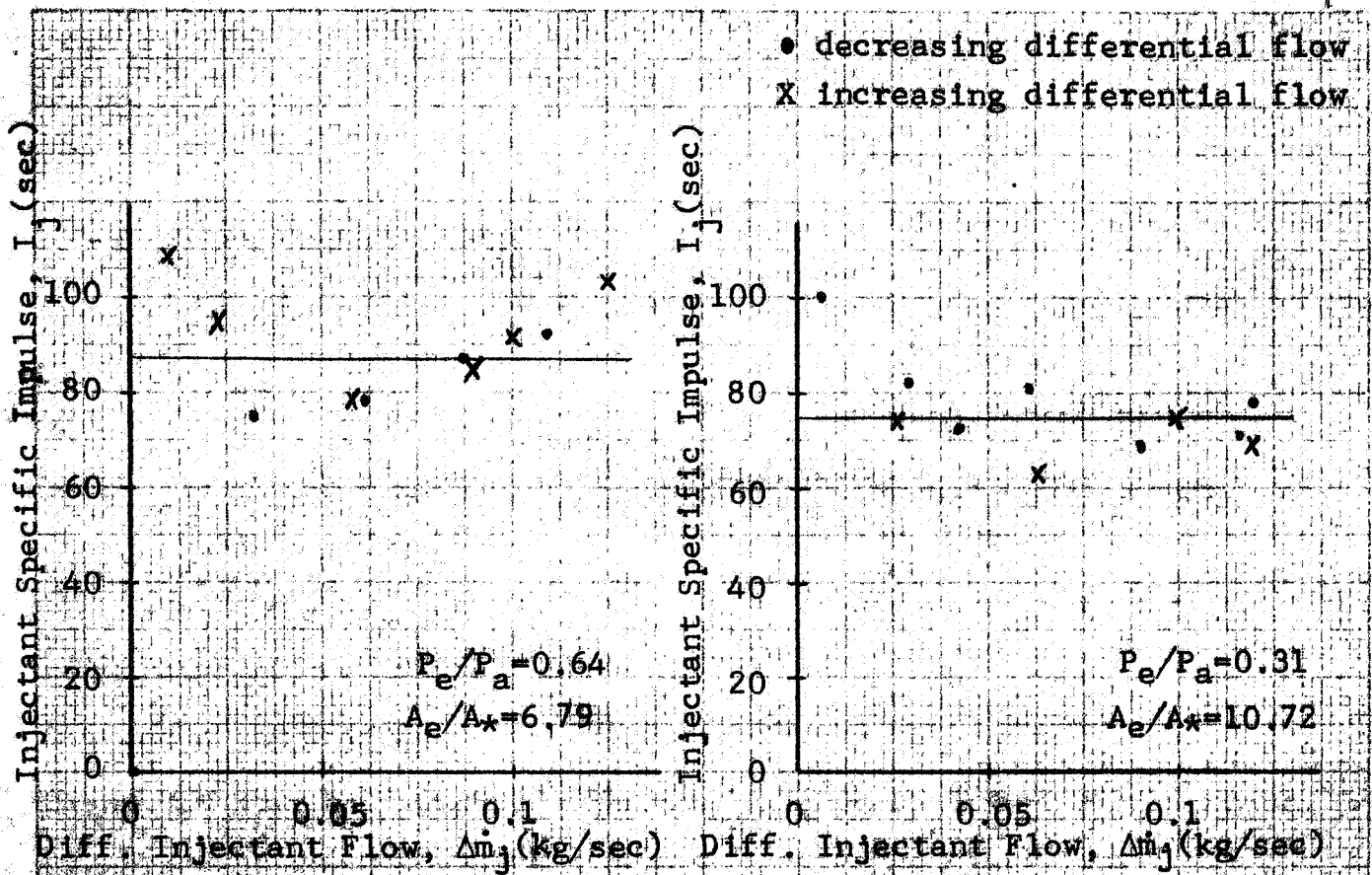| Extension	1	2	3	4
Specific impulse, I (sec)	62	60	56	56

Fig. 3.1a Test 1   I=63 sec
$\dot{m}$=2.81 kg/sec $\dot{m}_{jt}$=0.27 kg/sec
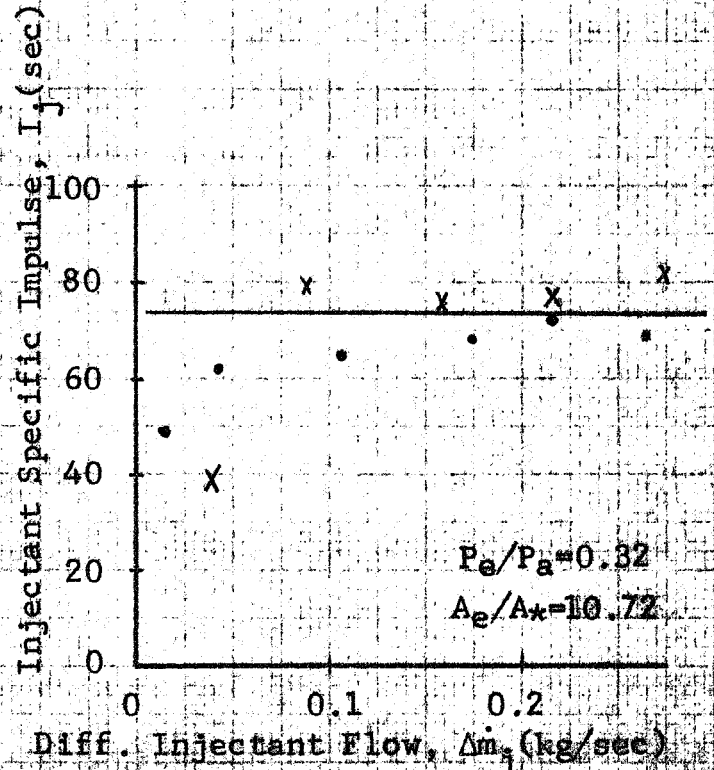
Fig. 3.1b Test 22   I=60 sec
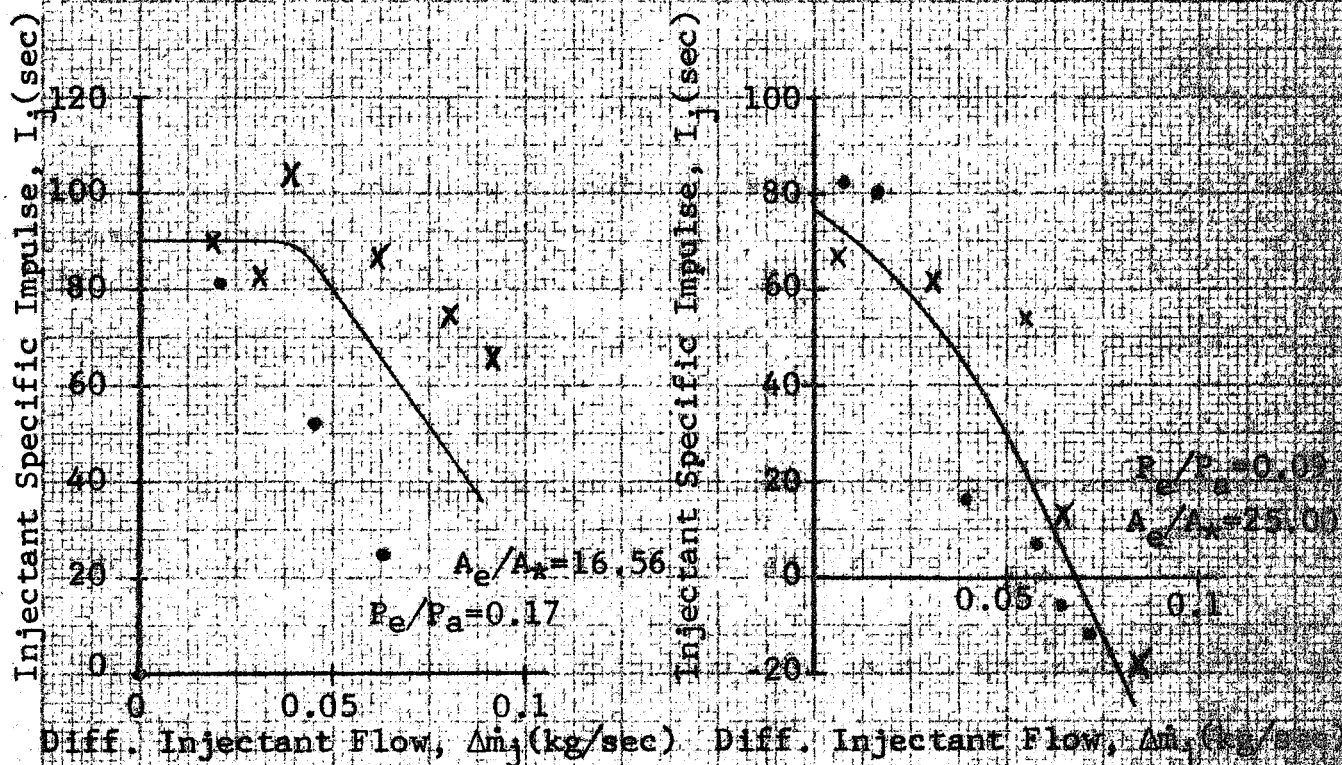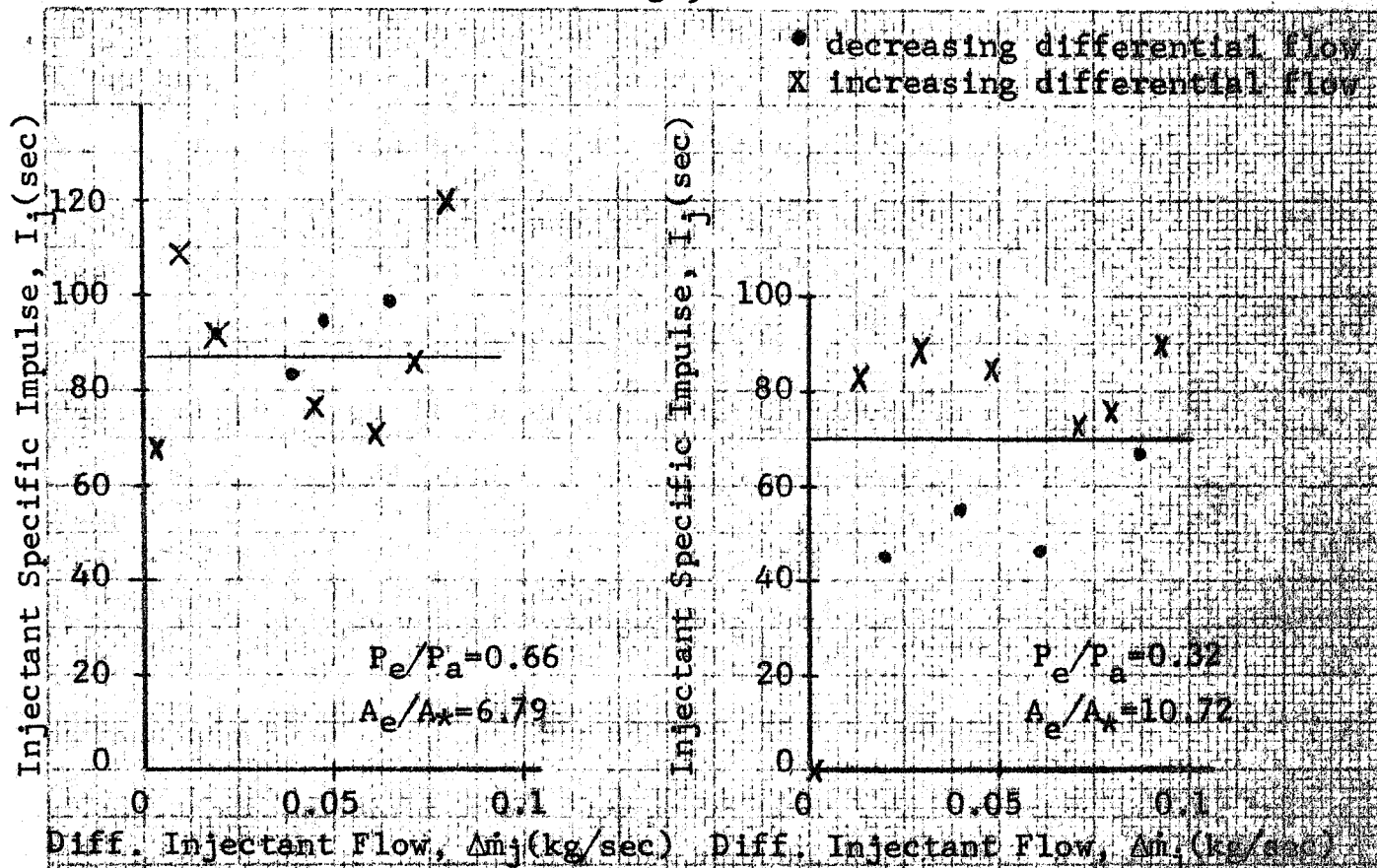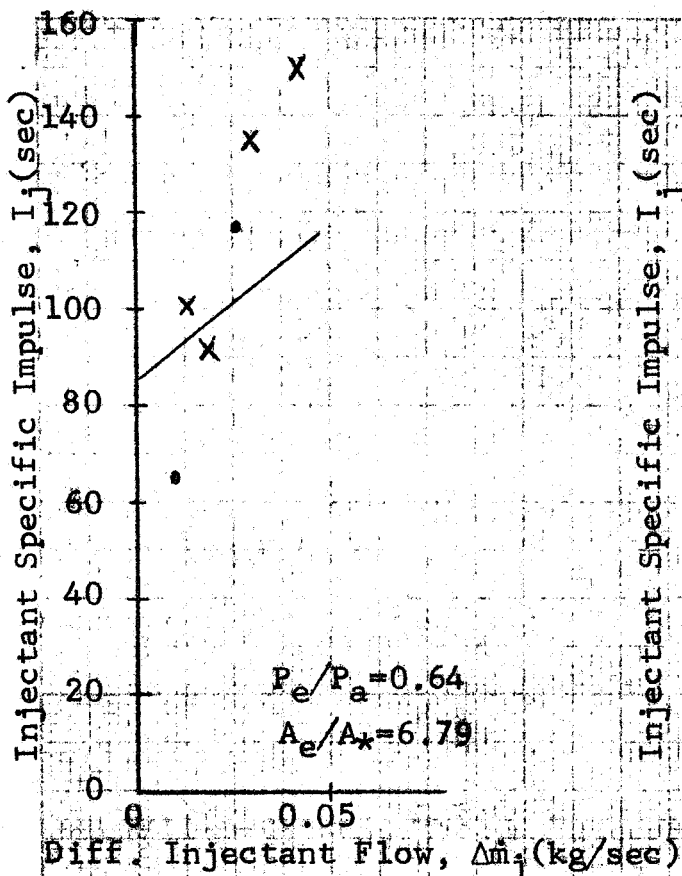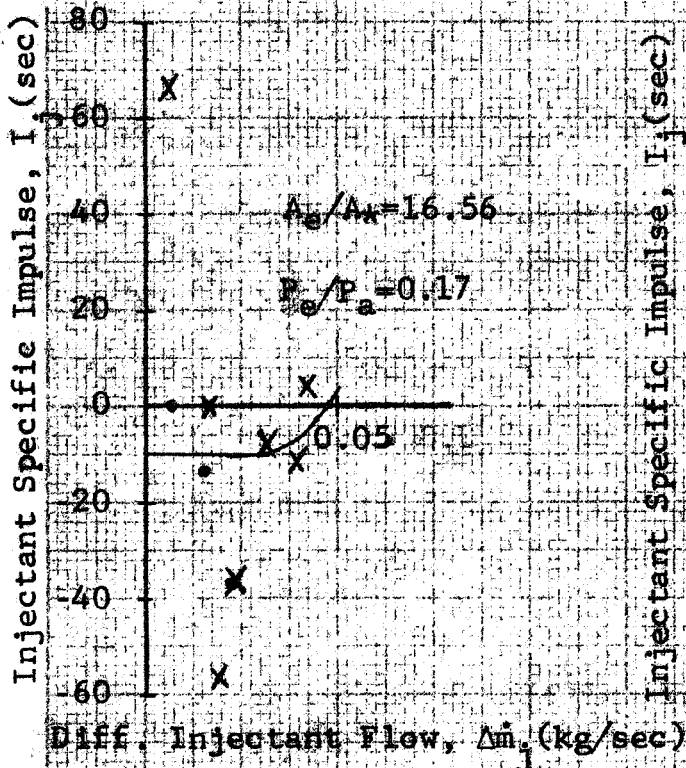$\dot{m}$=2.96 kg/sec $\dot{m}_{jt}$=0.28 kg/sec
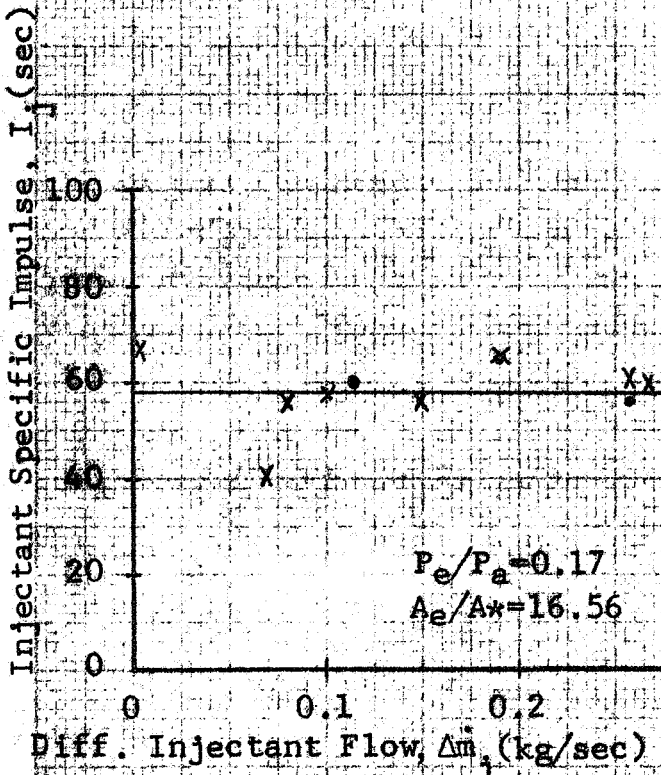
Fig. 3.1c Test 43   I=56 sec
$\dot{m}$=2.89 kg/sec $\dot{m}_{jt}$=0.275 kg/sec
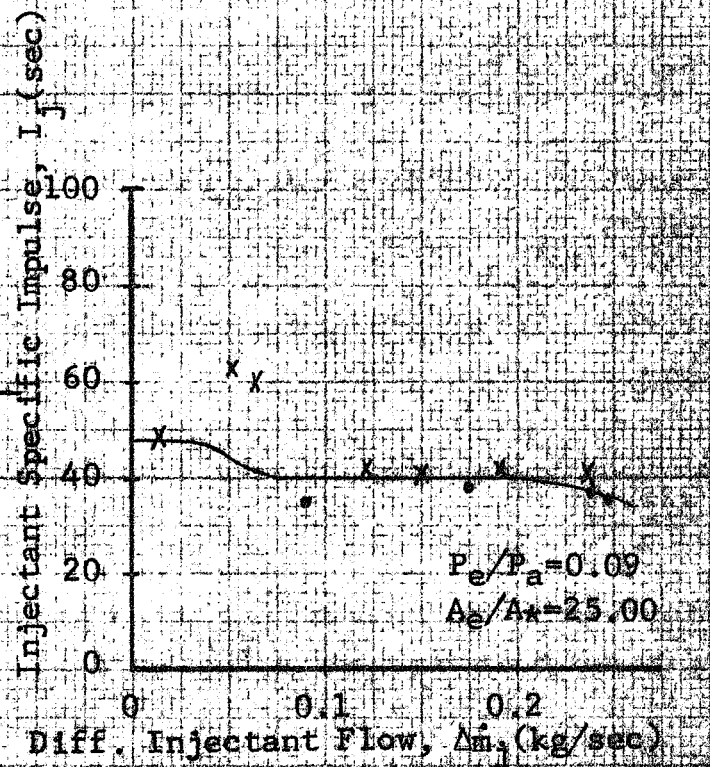
Fig. 3.1d Test 64 I=56 sec
$\dot{m}$=2.89 kg/sec $\dot{m}_{jt}$=0.25 kg/sec

Fig. 3.2a   Test 2   I=63 sec
$\dot{m}$=2.85 kg/sec $\dot{m}_{jt}$=0.22 kg/sec

Fig. 3.2b   Test 23   I=60 sec
$\dot{m}$=2.93 kg/sec $\dot{m}_{jt}$=0.22 kg/sec

Fig. 3.2c   Test 44   I=56 sec
$\dot{m}$=2.92 kg/sec $\dot{m}_{jt}$=0.21 kg/sec

Fig. 3.2d   Test 65   I=56 sec
$\dot{m}$=2.90 kg/sec $\dot{m}_{jt}$=0.215 kg/sec

Fig. 3.3a Test 3   I=63 sec
$\dot{m}$=2.89 kg/sec $\dot{m}_{jt}$=0.18 kg/sec

Fig. 3.3b Test 24   I=60 sec
$\dot{m}$=2.89 kg/sec $\dot{m}_{jt}$=0.18 kg/sec

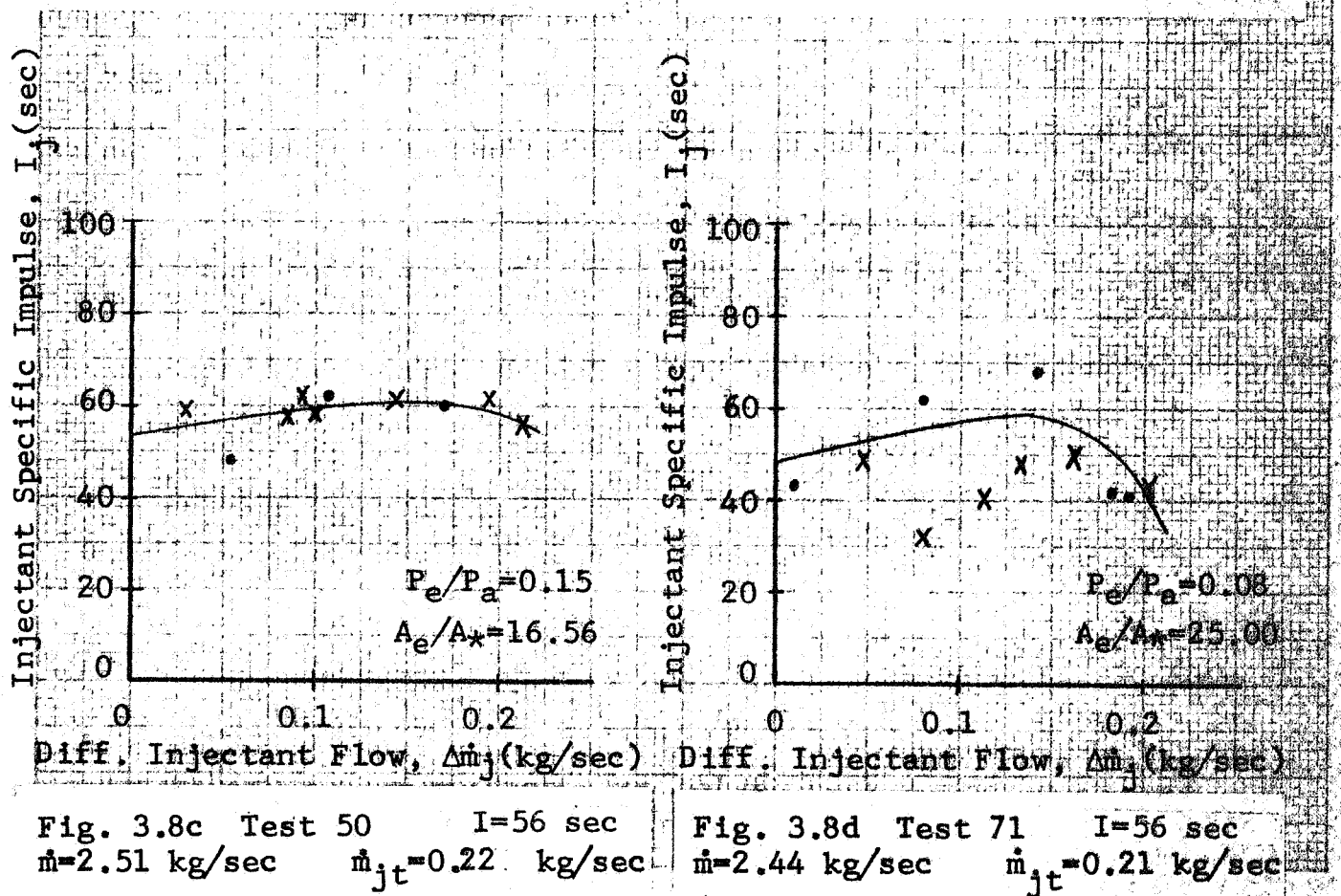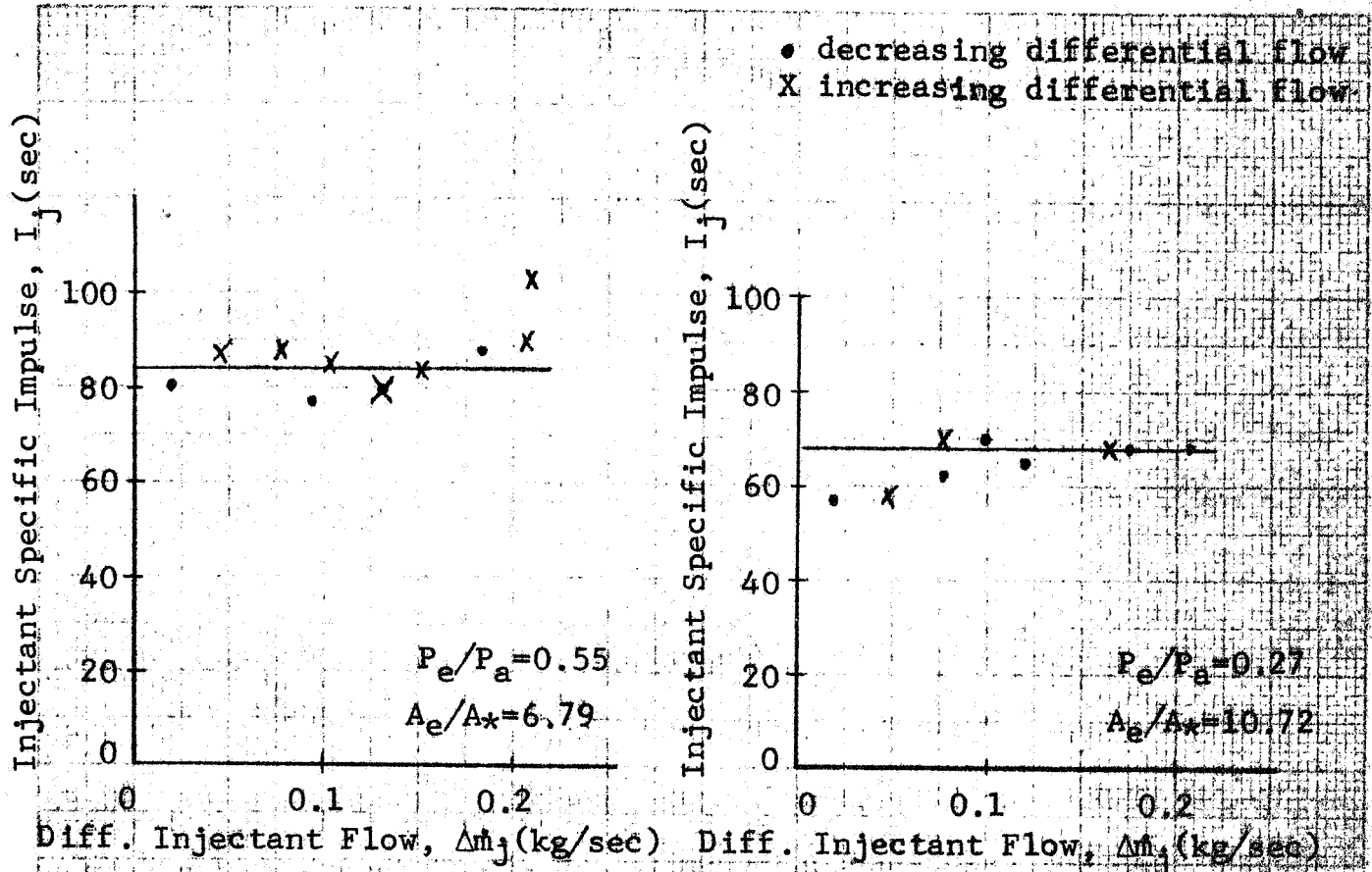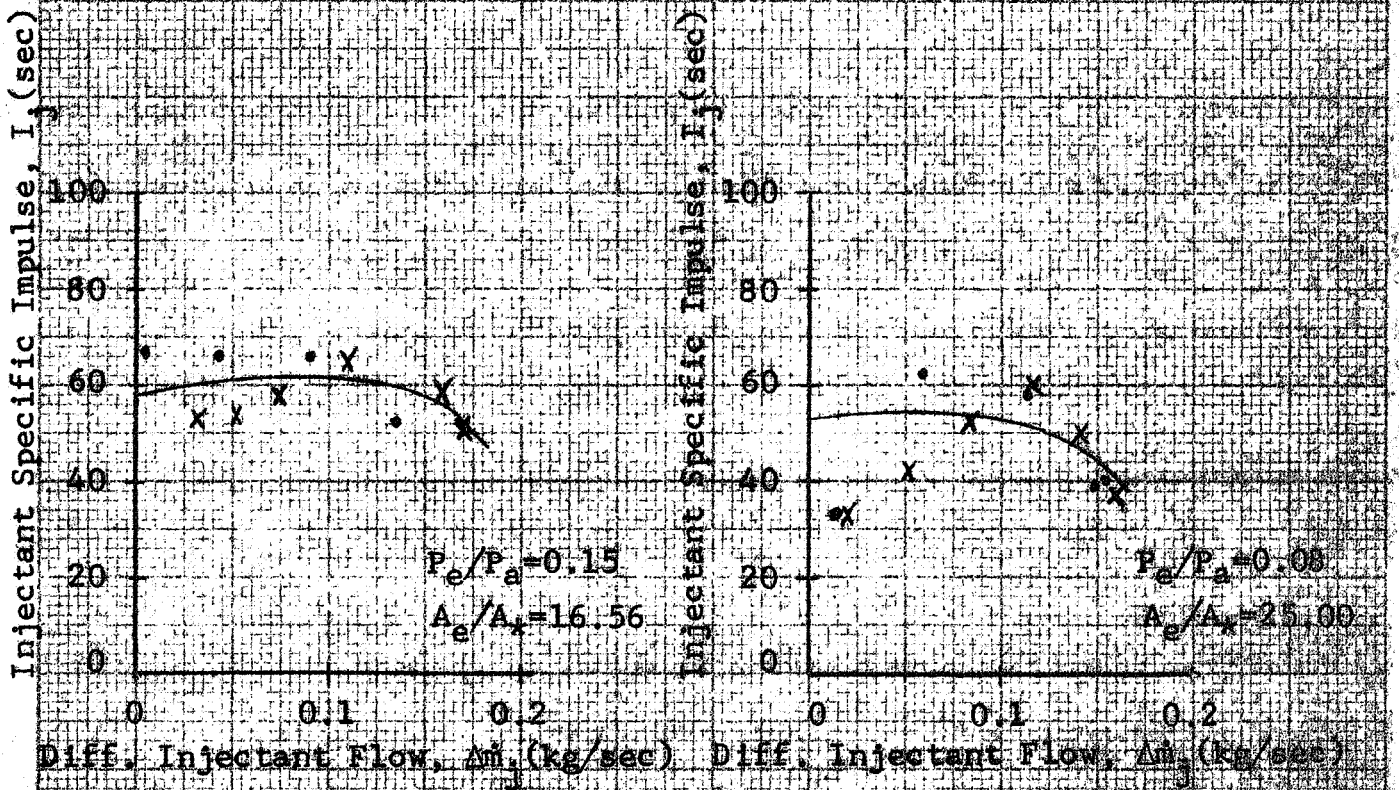Fig. 3.3c Test 45   I=56 sec
$\dot{m}$=2.92 kg/sec $\dot{m}_{jt}$=0.18 kg/sec

Fig. 3.3d Test 66   I=56 sec
$\dot{m}$=2.90 kg/sec $\dot{m}_{jt}$=0.17 kg/sec

● decreasing differential flow
X increasing differential flow

Fig. 3.4a   Test 4   I=63 sec
$\dot{m}$=2.87 kg/sec $\dot{m}_{jt}$=0.13 kg/sec

Fig. 3.4b   Test 25   I=60 sec
$\dot{m}$=2.82 kg/sec $\dot{m}_{jt}$=0.13 kg/sec
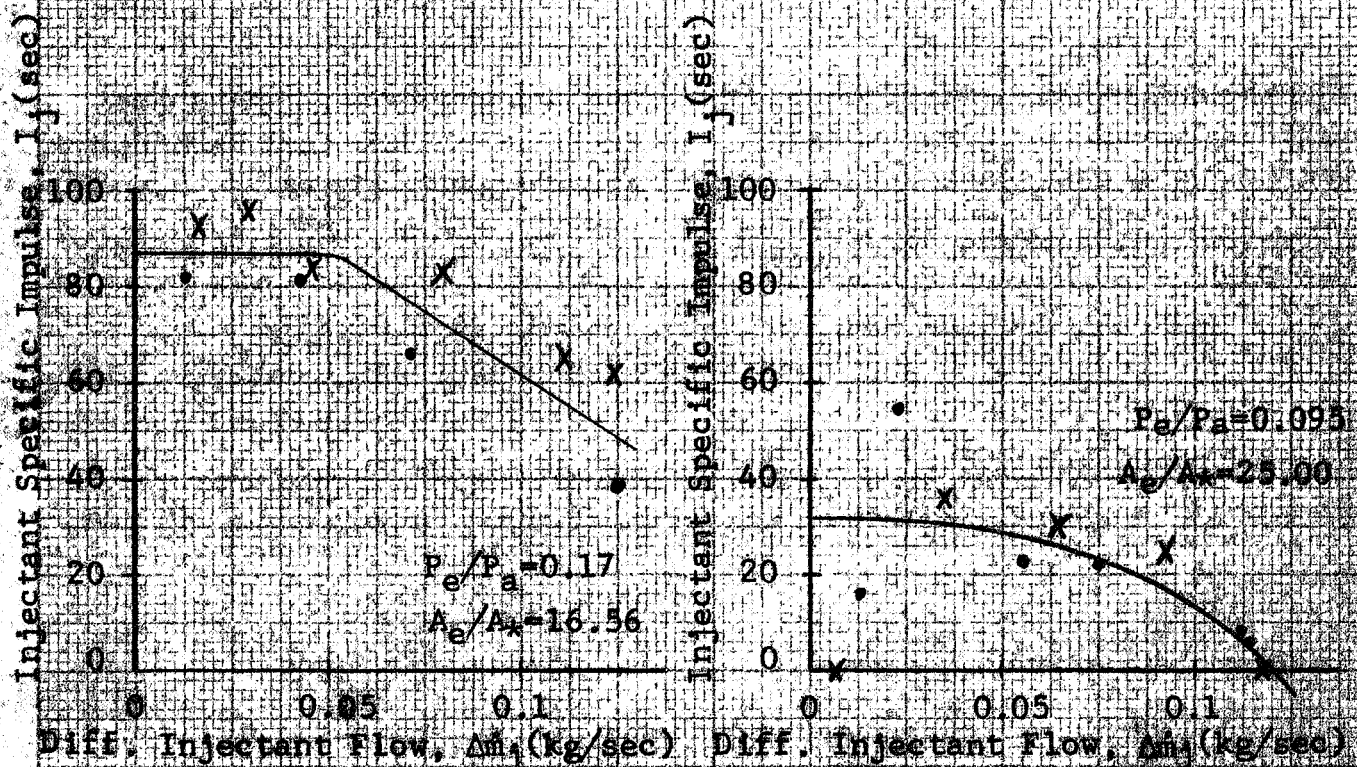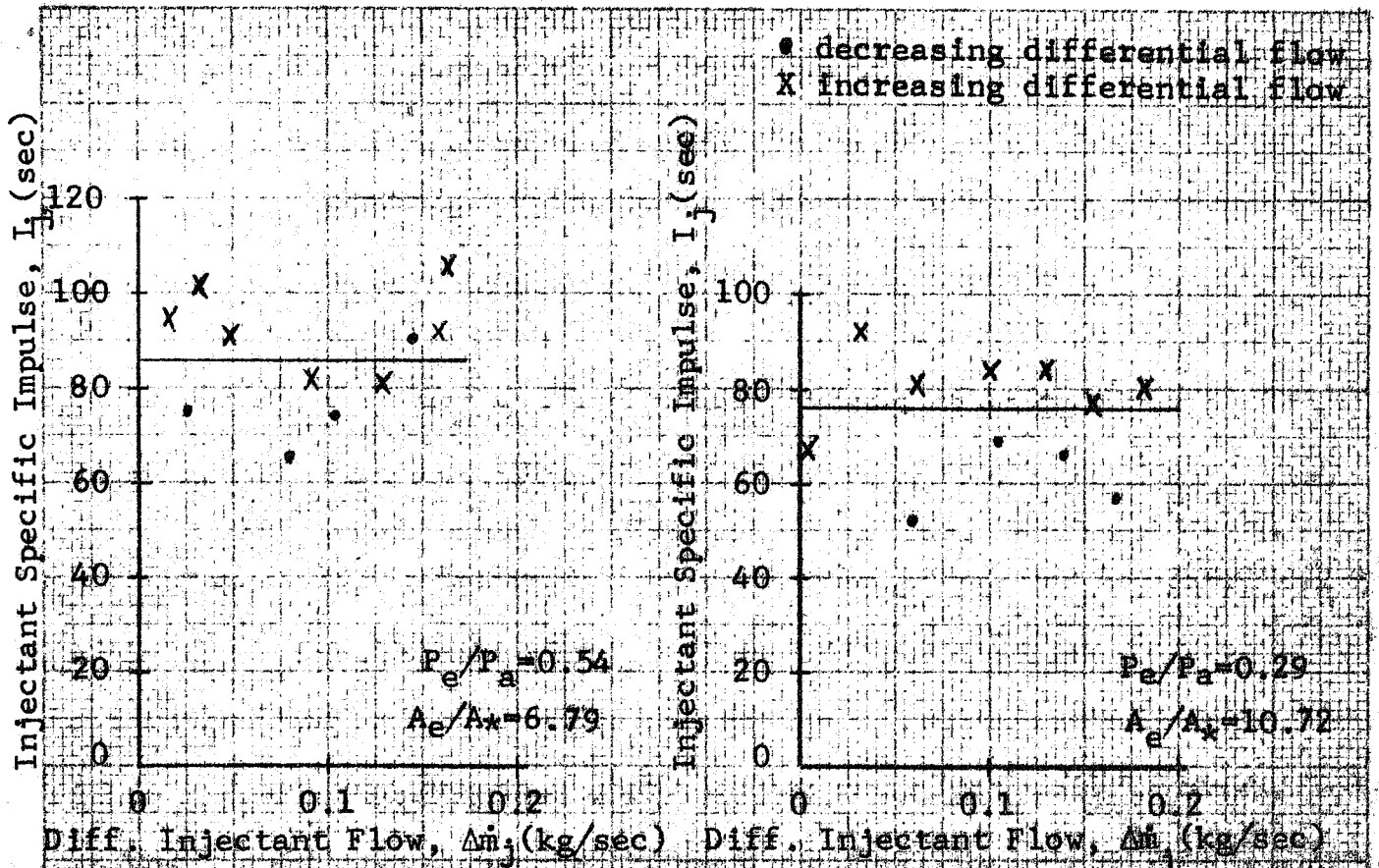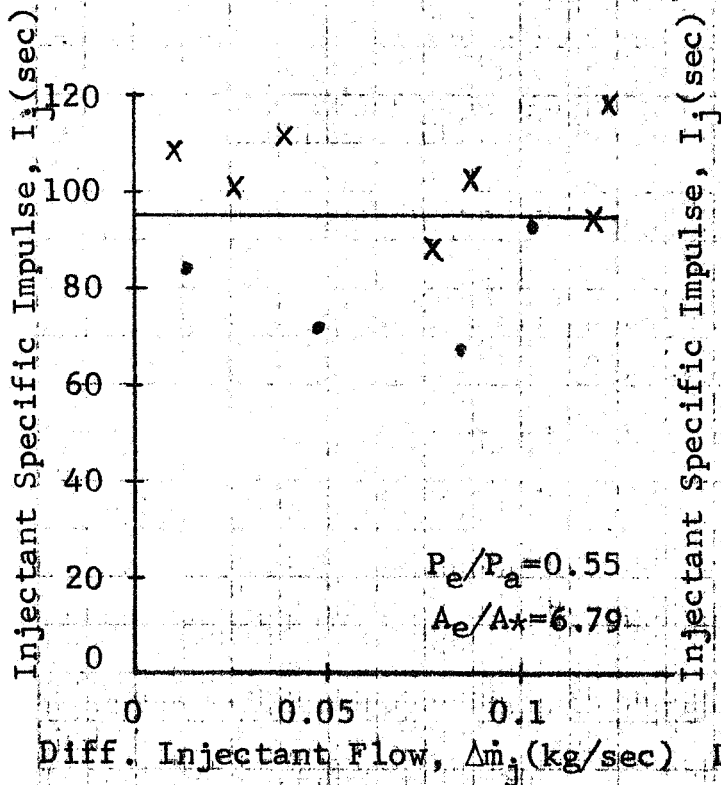
Fig. 3.4c   Test 46   I=56 sec
$\dot{m}$=2.89 kg/sec $\dot{m}_{jt}$=0.13 kg/sec

Fig. 3.4d   Test 67   I=56 sec
$\dot{m}$=2.86 kg/sec $\dot{m}_{jt}$=0.13 kg/sec

Fig. 3.5a   Test 5   I=63 sec
$\dot{m}$=2.91 kg/sec $\dot{m}_{jt}$=.085 kg/sec

Fig. 3.5b   Test 26   I=60 sec
$\dot{m}$=2.95 kg/sec $\dot{m}_{jt}$=0.09 kg/sec

Fig. 3.5c   Test 47   I=56 sec
$\dot{m}$=2.92 kg/sec $\dot{m}_{jt}$=0.09 kg/sec

Fig. 3.5d   Test 68   I=56 sec
$\dot{m}$=2.80 kg/sec $\dot{m}_{jt}$=0.085 kg/sec

Fig. 3.6a Test 6   I=63 sec
ṁ=2.83 kg/sec   ṁ_jt=0.05 kg/sec
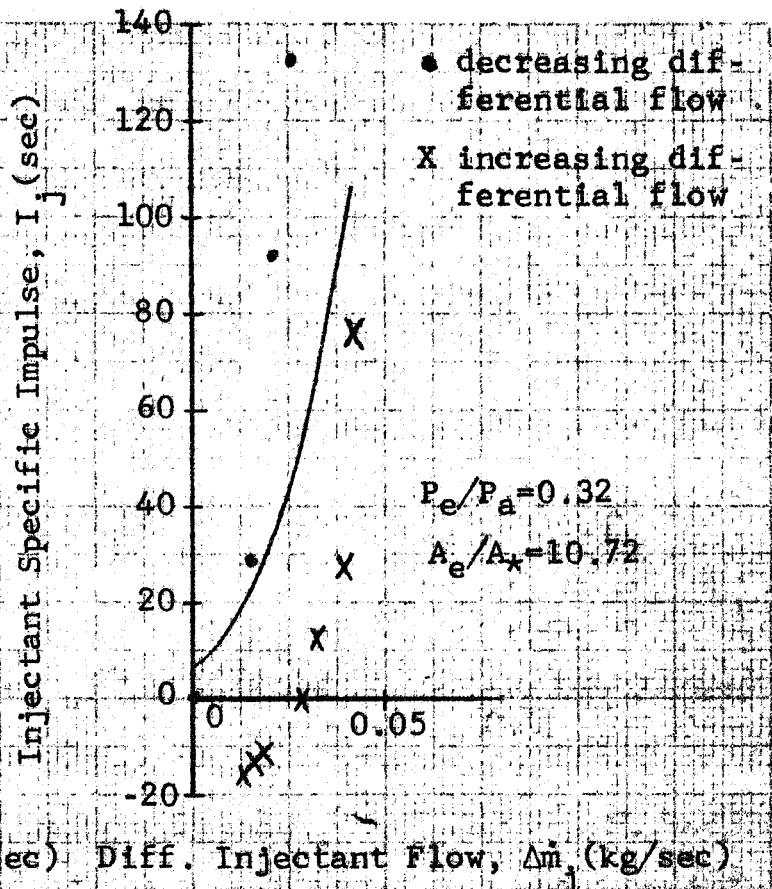
Fig. 3.6b Test 27   I=60 sec
ṁ=2.92 kg/sec   ṁ_jt=0.04 kg/sec

Fig. 3.6c Test 48   I=56 sec
ṁ=2.89 kg/sec   ṁ_jt=0.04 kg/sec
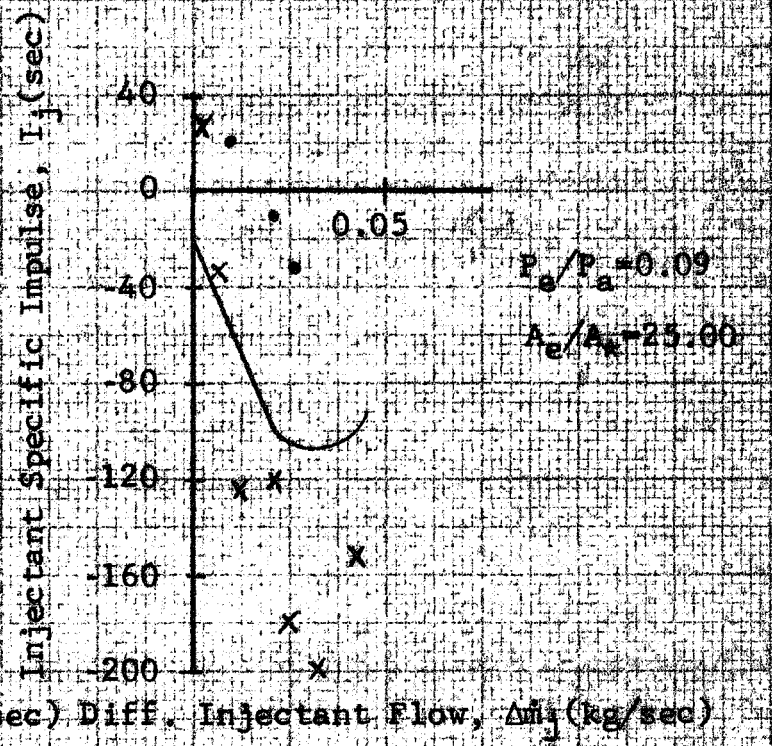
Fig. 3.6d Test 69   I=56 sec
ṁ=2.78 kg/sec   ṁ_jt=0.04 kg/sec
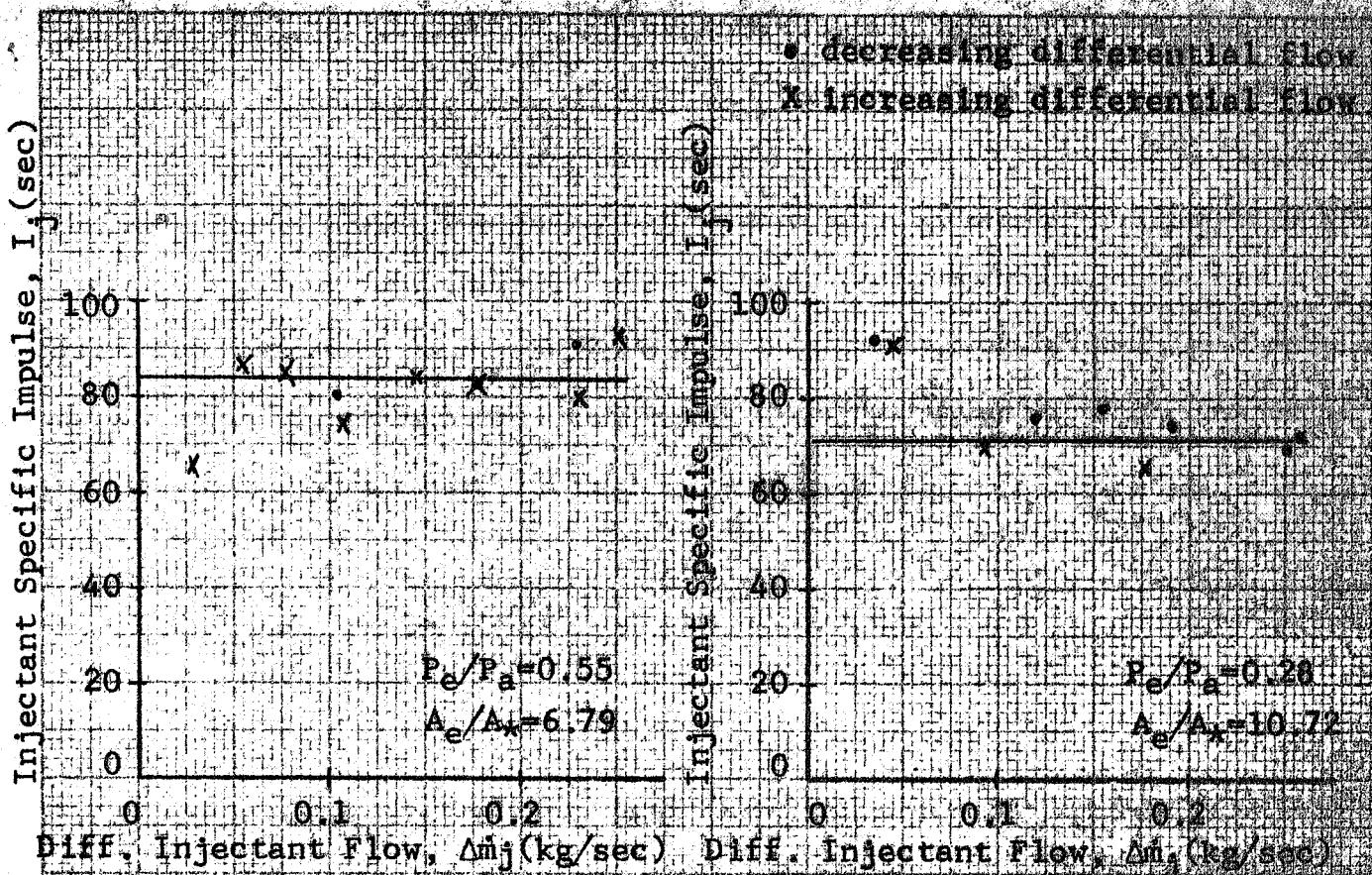
Fig. 3.7a   Test 7   I=62 sec
$\dot{m}$=2.41 kg/sec $\dot{m}_{jt}$=0.27 kg/sec

Fig. 3.7b   Test 28   I=59 sec
$\dot{m}$=2.56 kg/sec $\dot{m}_{jt}$=0.26 kg/sec
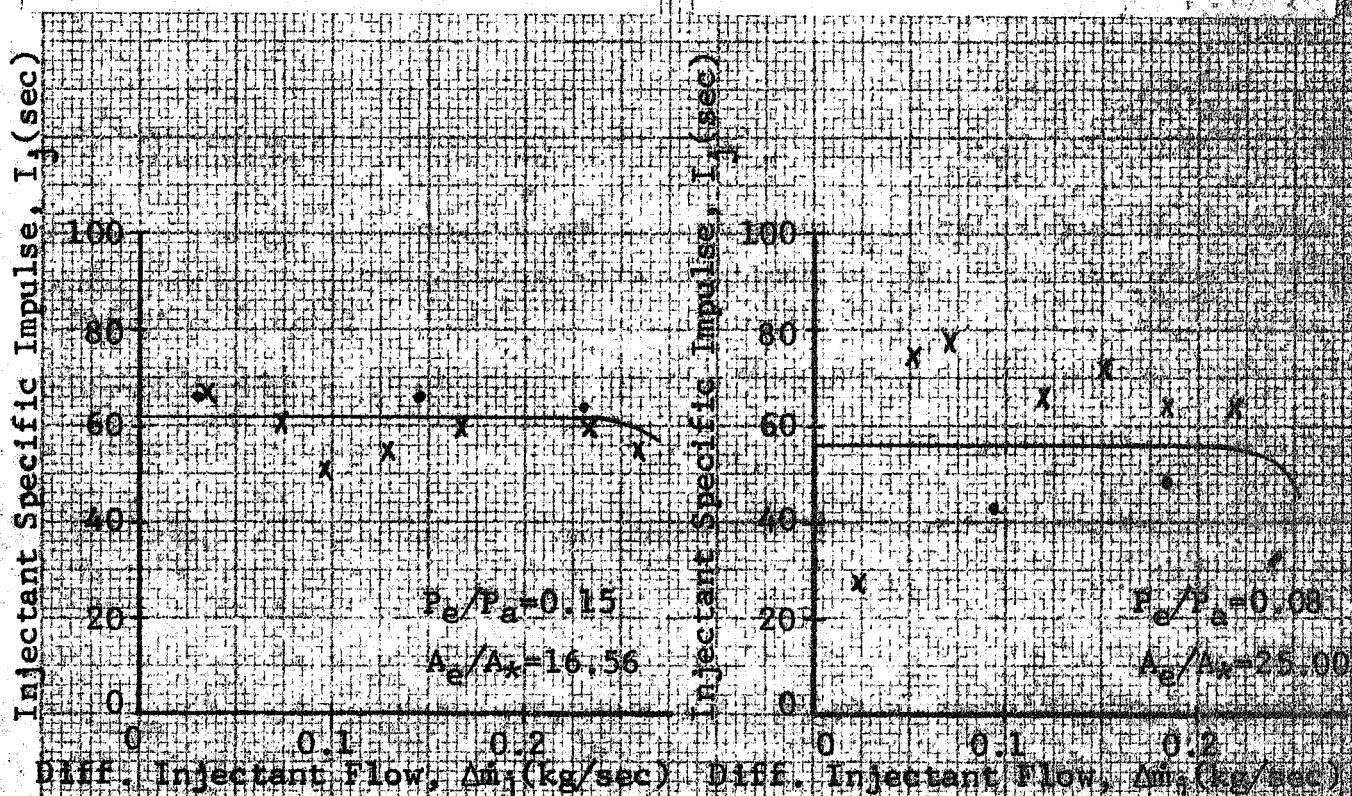
Fig. 3.7c   Test 49   I=56 sec
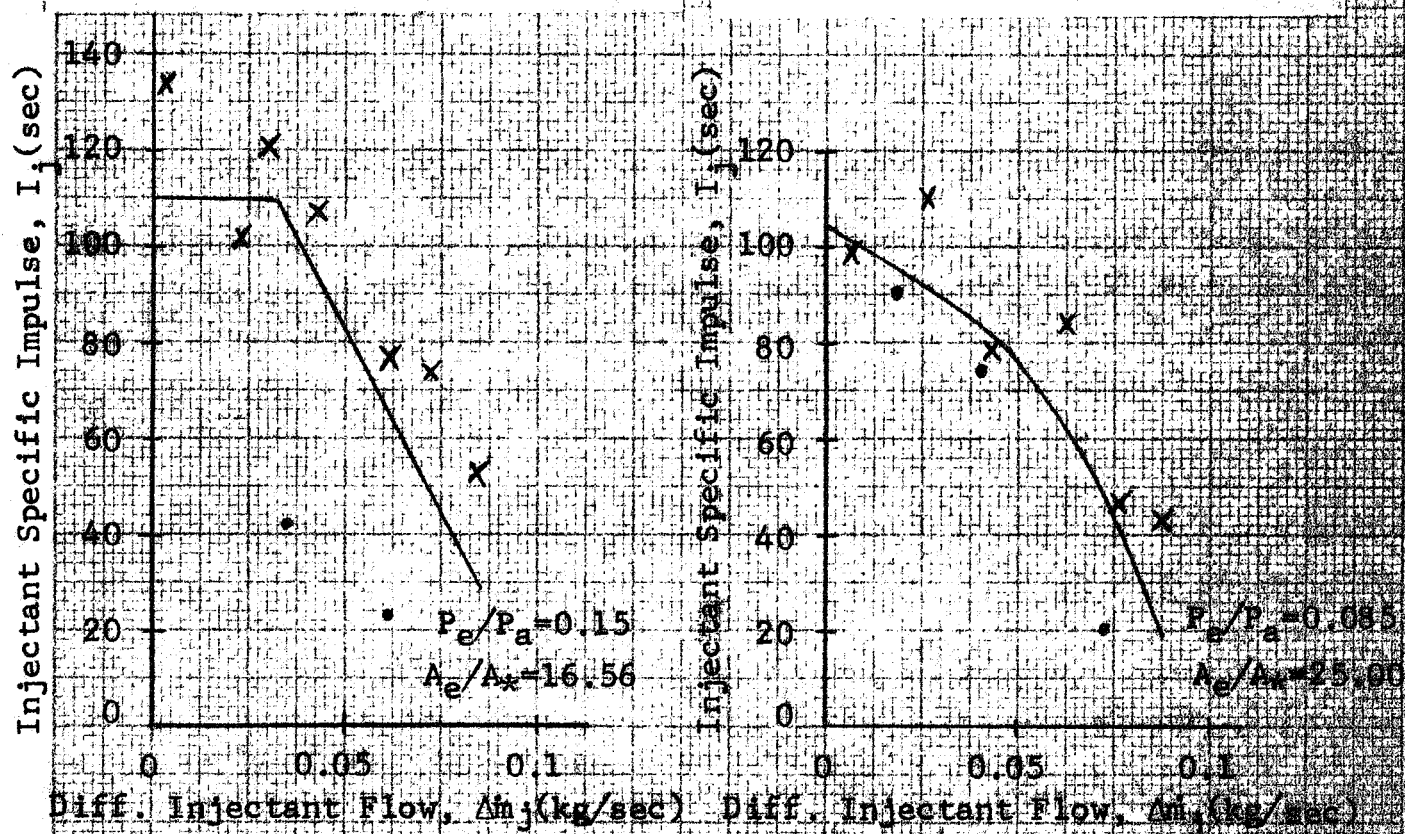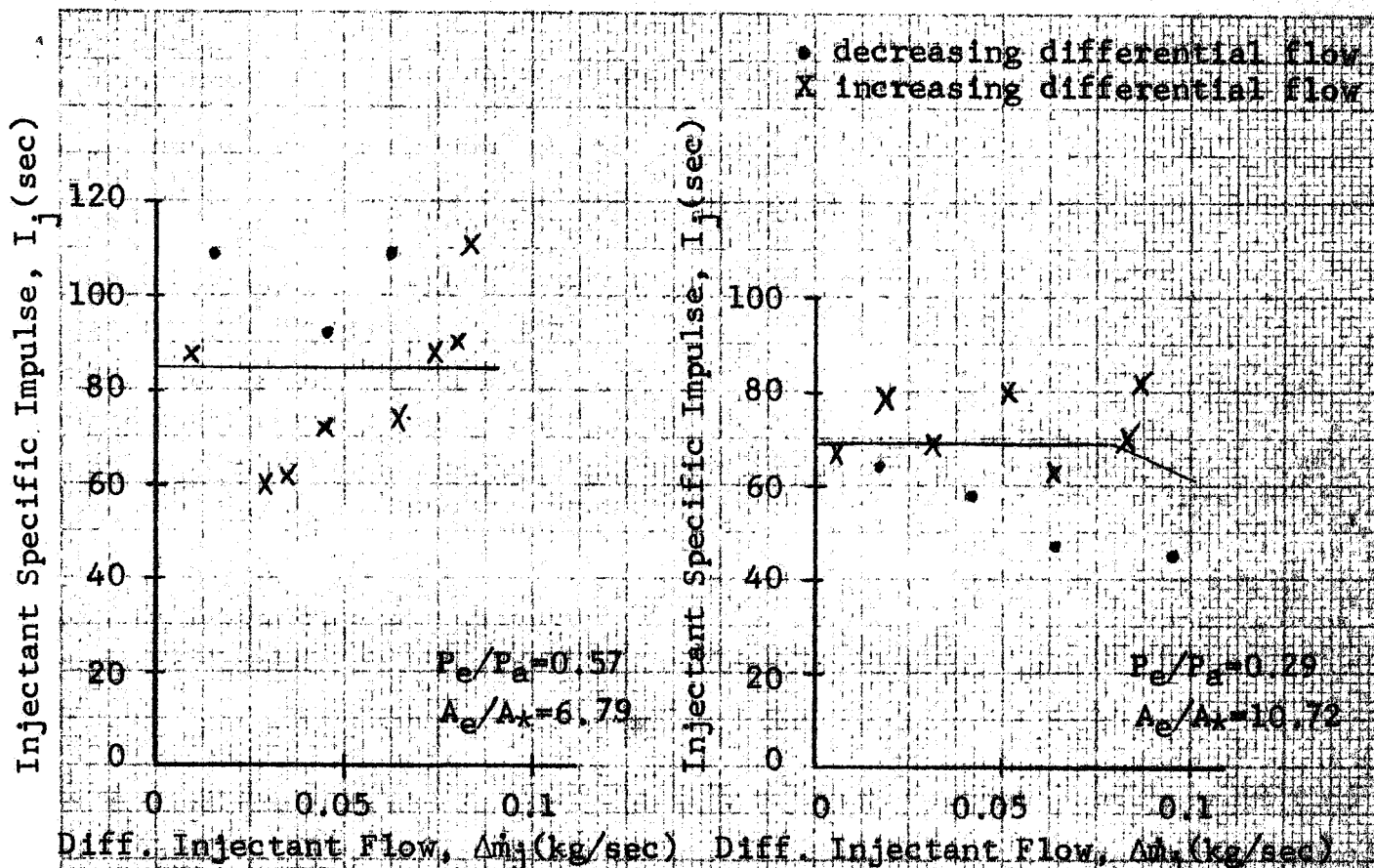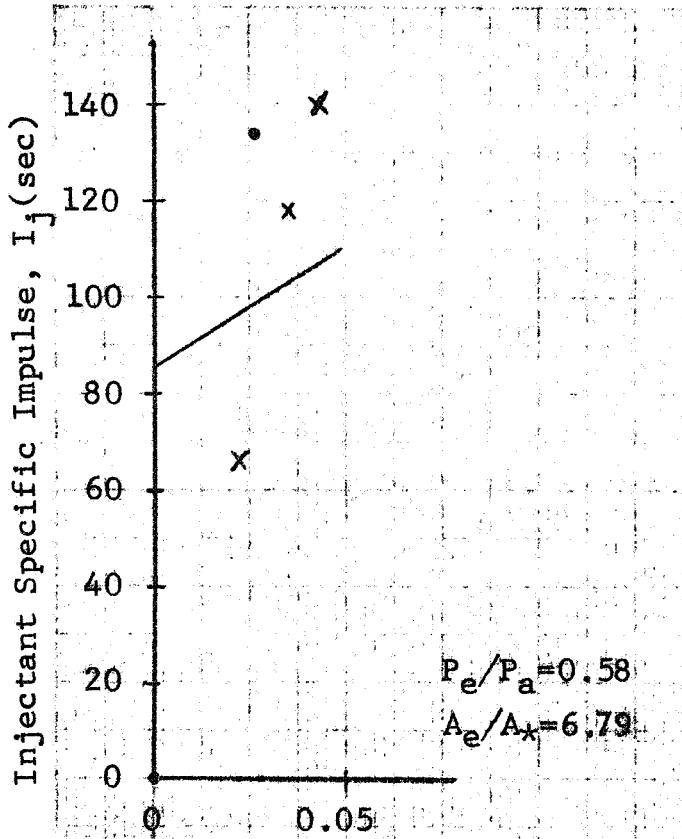$\dot{m}$=2.545 kg/sec $\dot{m}_{jt}$=0.275 kg/sec

Fig. 3.7d   Test 70   I=56 sec
$\dot{m}$=2.41 kg/sec $\dot{m}_{jt}$=0.25 kg/sec

Fig. 3.8a   Test 8   I=62 sec
ṁ=2.41 kg/sec   ṁ$_{jt}$=0.22 kg/sec

Fig. 3.8b   Test 29   I=59 sec
ṁ=2.42 kg/sec   ṁ$_{jt}$=0.22 kg/sec

Fig. 3.8c   Test 50   I=56 sec
ṁ=2.51 kg/sec   ṁ$_{jt}$=0.22 kg/sec

Fig. 3.8d   Test 71   I=56 sec
ṁ=2.44 kg/sec   ṁ$_{jt}$=0.21 kg/sec

Fig. 3.9a   Test 9   I=62 sec
$\dot{m}$=2.35 kg/sec $\dot{m}_{jt}$=0.18 kg/sec

Fig. 3.9b   Test 30   I=59 sec
$\dot{m}$=2.58 kg/sec $\dot{m}_{jt}$=0.18 kg/sec

Fig. 3.9c   Test 51   I=56 sec
$\dot{m}$=2.48 kg/sec $\dot{m}_{jt}$=0.18 kg/sec

Fig. 3.9d   Test 72   I=56 sec
$\dot{m}$=2.38 kg/sec $\dot{m}_{jt}$=0.175 kg/sec

Fig. 3.10a   Test 10   I=62 sec
ṁ=2.60 kg/sec   ṁ$_{jt}$=0.135 kg/sec
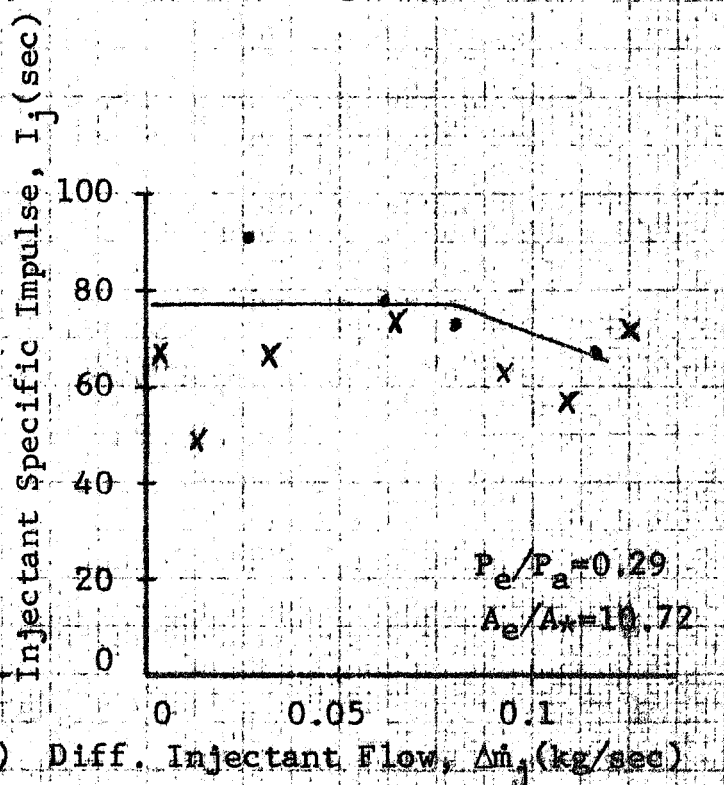
Fig. 3.10b   Test 31   I=59 sec
ṁ=2.52 kg/sec   ṁ$_{jt}$=0.13 kg/sec
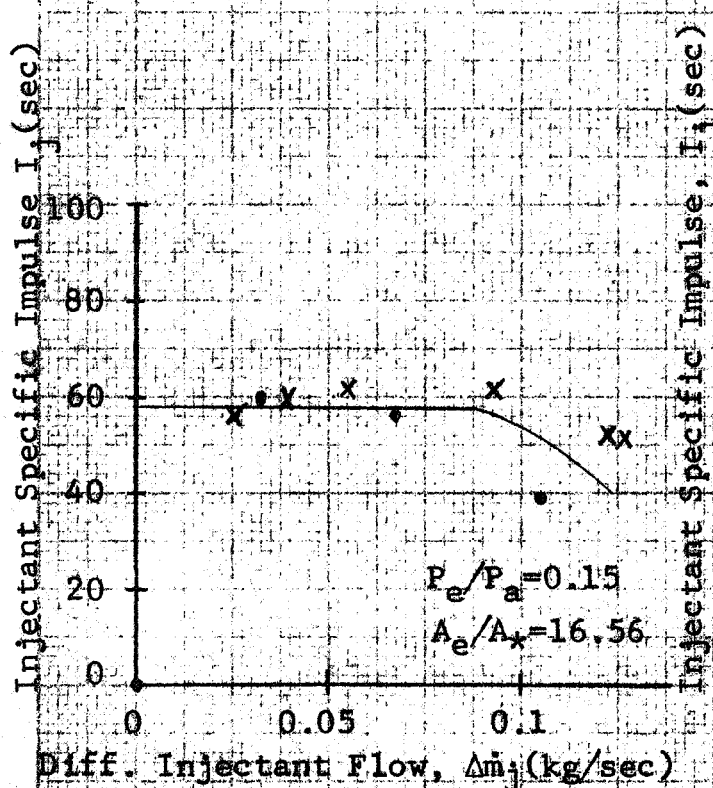
Fig. 3.10c   Test 52   I=56 sec
ṁ=2.45 kg/sec   ṁ$_{jt}$=0.13 kg/sec
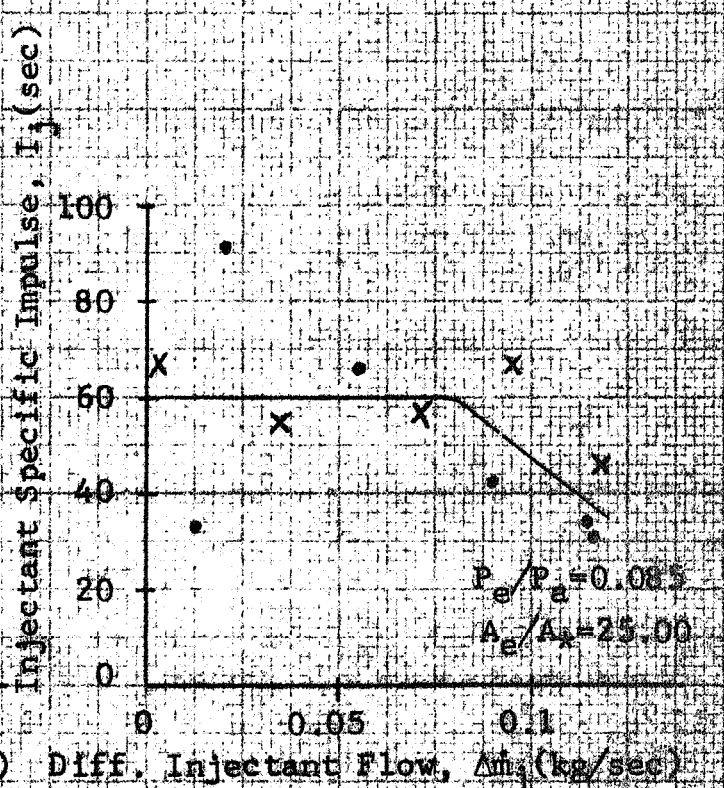
Fig. 3.10d   Test 73   I=56 sec
ṁ=2.60 kg/sec   ṁ$_{jt}$=0.13 kg/sec

Fig. 3.11a   Test 11   I=62 sec
ṁ=2.60 kg/sec   ṁ_jt=0.09 kg/sec

Fig. 3.11b   Test 32   I=59 sec
ṁ=2.56 kg/sec   ṁ_jt=0.09 kg/sec

Fig. 3.11c   Test 53   I=56 sec
ṁ=2.65 kg/sec   ṁ_jt=0.08 kg/sec

Fig. 3.11d   Test 74   I=56 sec
ṁ=2.60 kg/sec   ṁ_jt=0.09 kg/sec
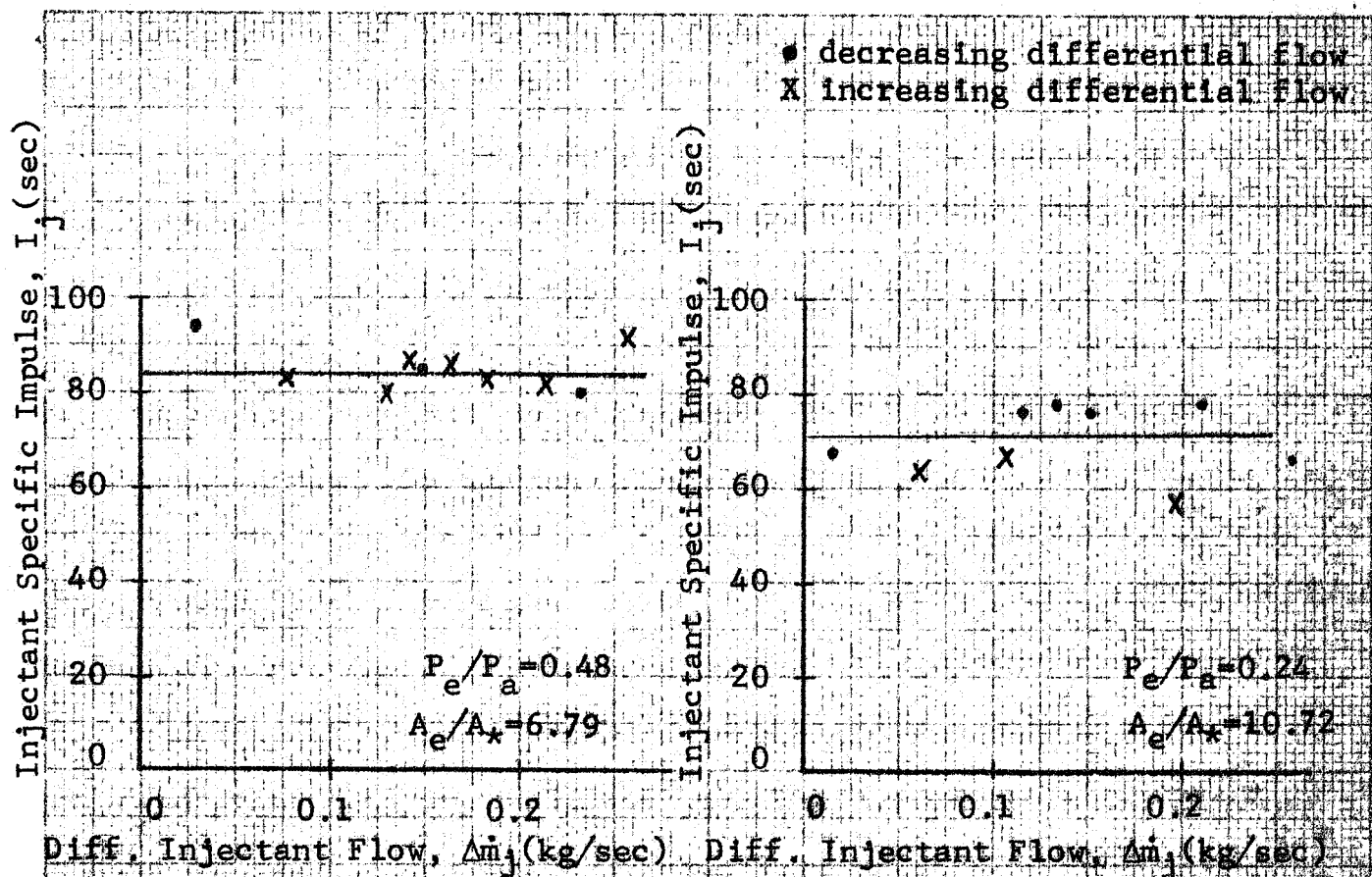
Fig. 3.12a   Test 12   I=62 sec
$\dot{m}$=2.65 kg/sec $\dot{m}_{jt}$=0.05 kg/sec
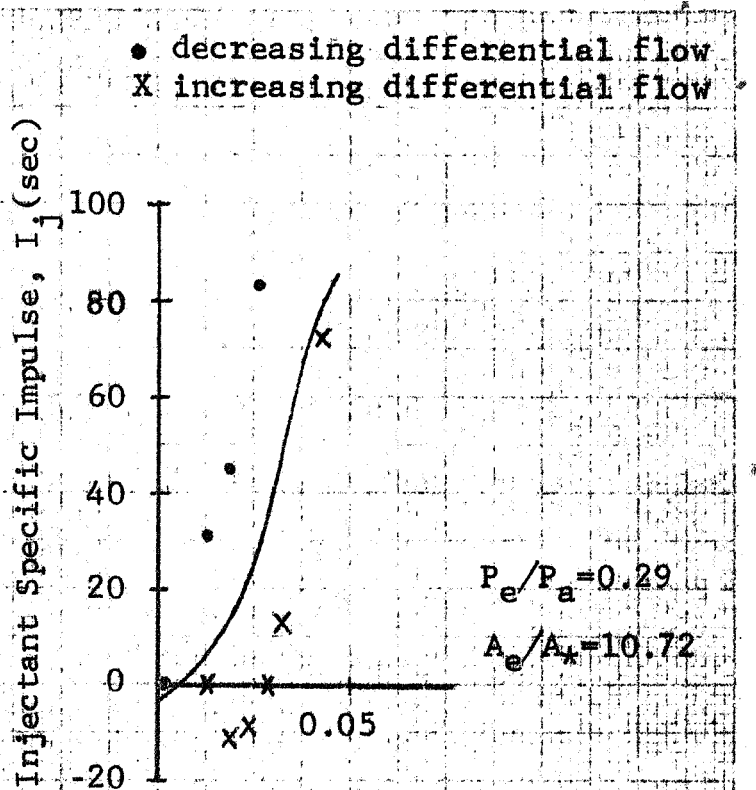
Fig. 3.12b   Test 33   I=59 sec
$\dot{m}$=2.52 kg/sec $\dot{m}_{jt}$=0.04 kg/sec
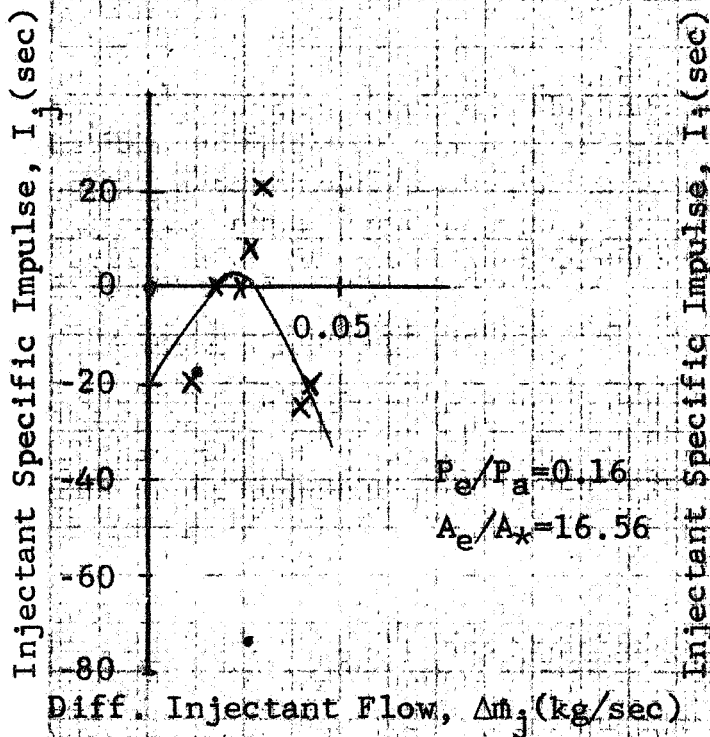
Fig. 3.12c   Test 54   I=56 sec
$\dot{m}$=2.69 kg/sec $\dot{m}_{jt}$=0.04 kg/sec
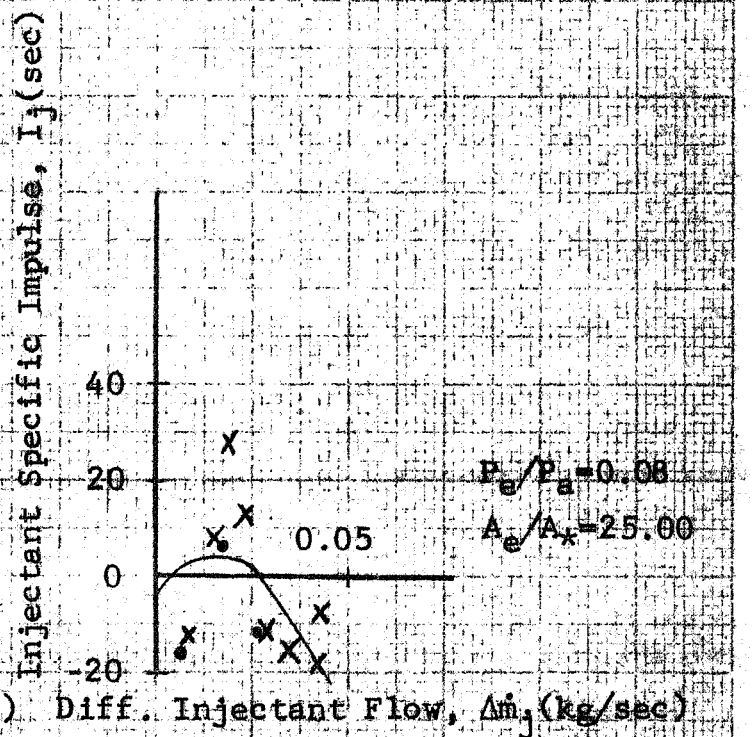
Fig. 3.12d   Test 75   I=56 sec
$\dot{m}$=2.51 kg/sec $\dot{m}_{jt}$=0.04 kg/sec

Fig. 3.13a   Test 13   I=61 sec
$\dot{m}$=2.17 kg/sec $\dot{m}_{jt}$=0.26 kg/sec

Fig. 3.13b   Test 34   I=58 sec
$\dot{m}$=2.12 kg/sec $\dot{m}_{jt}$=0.265 kg/sec

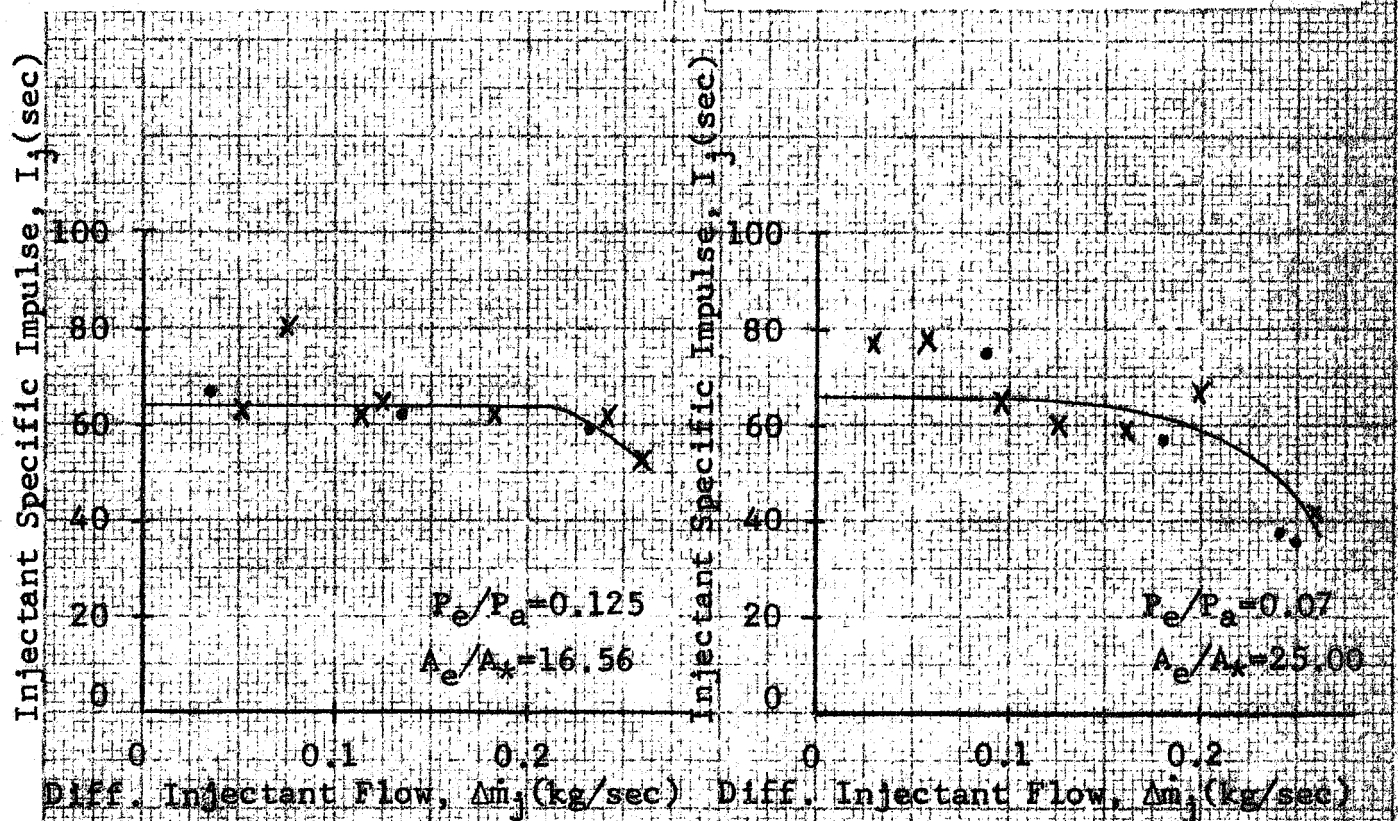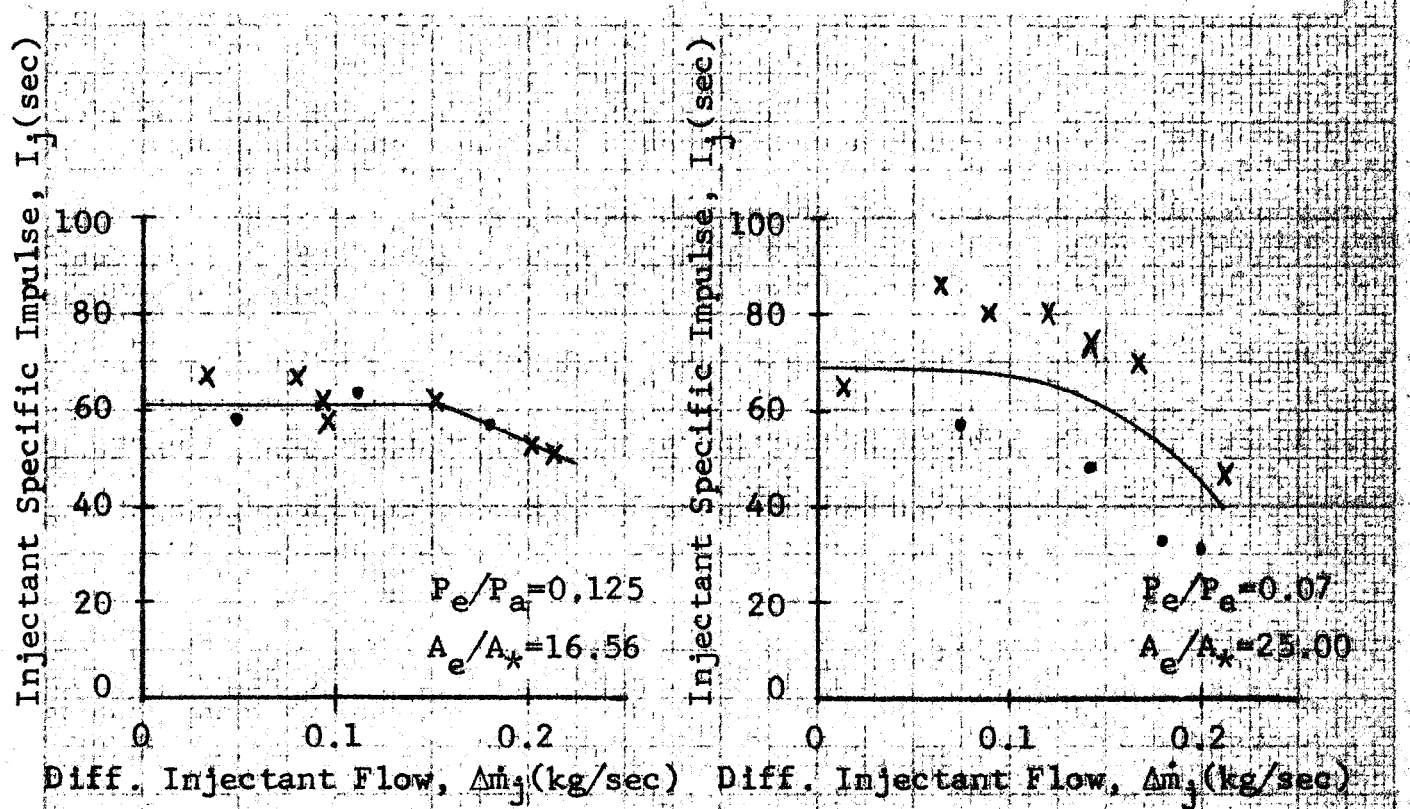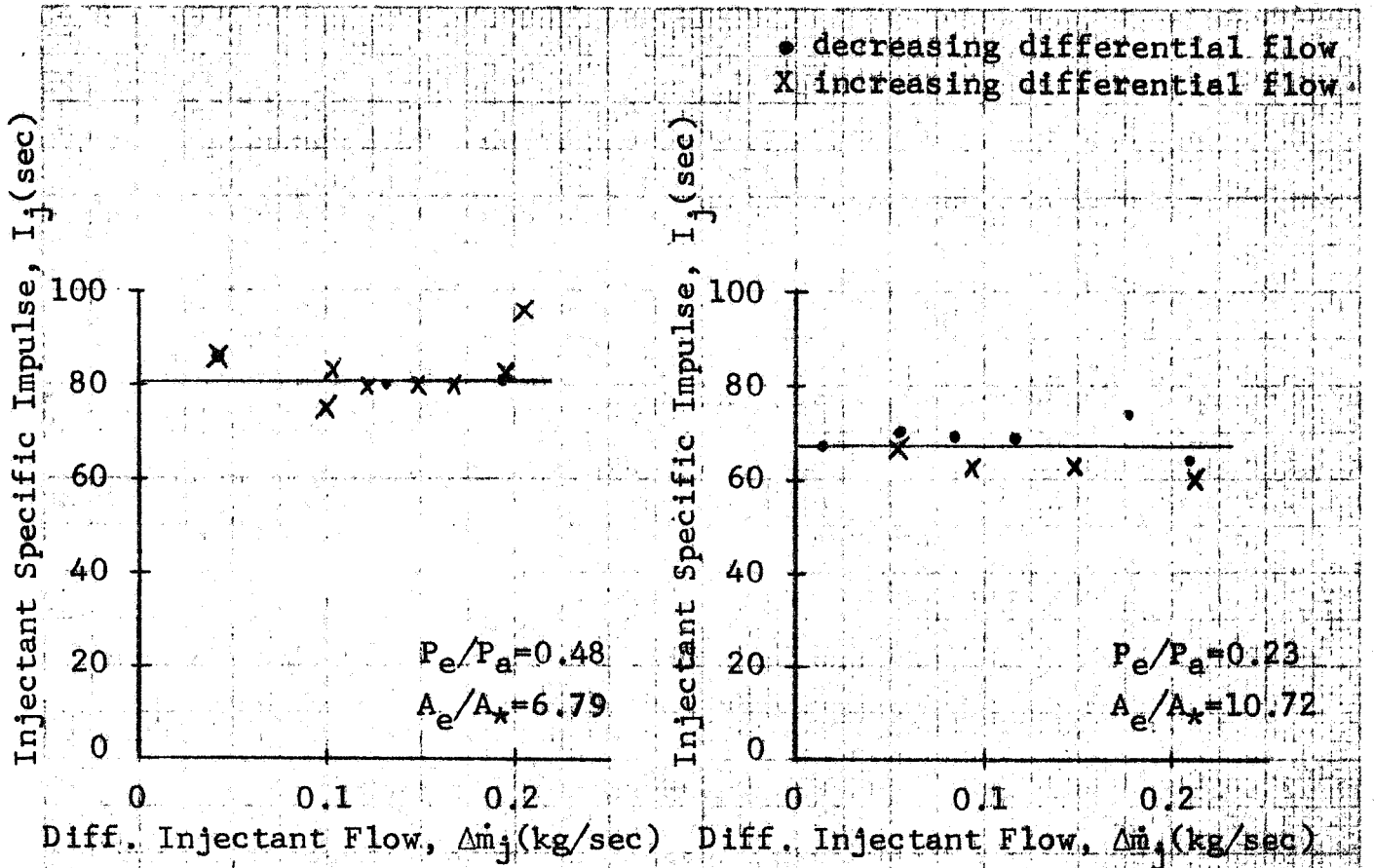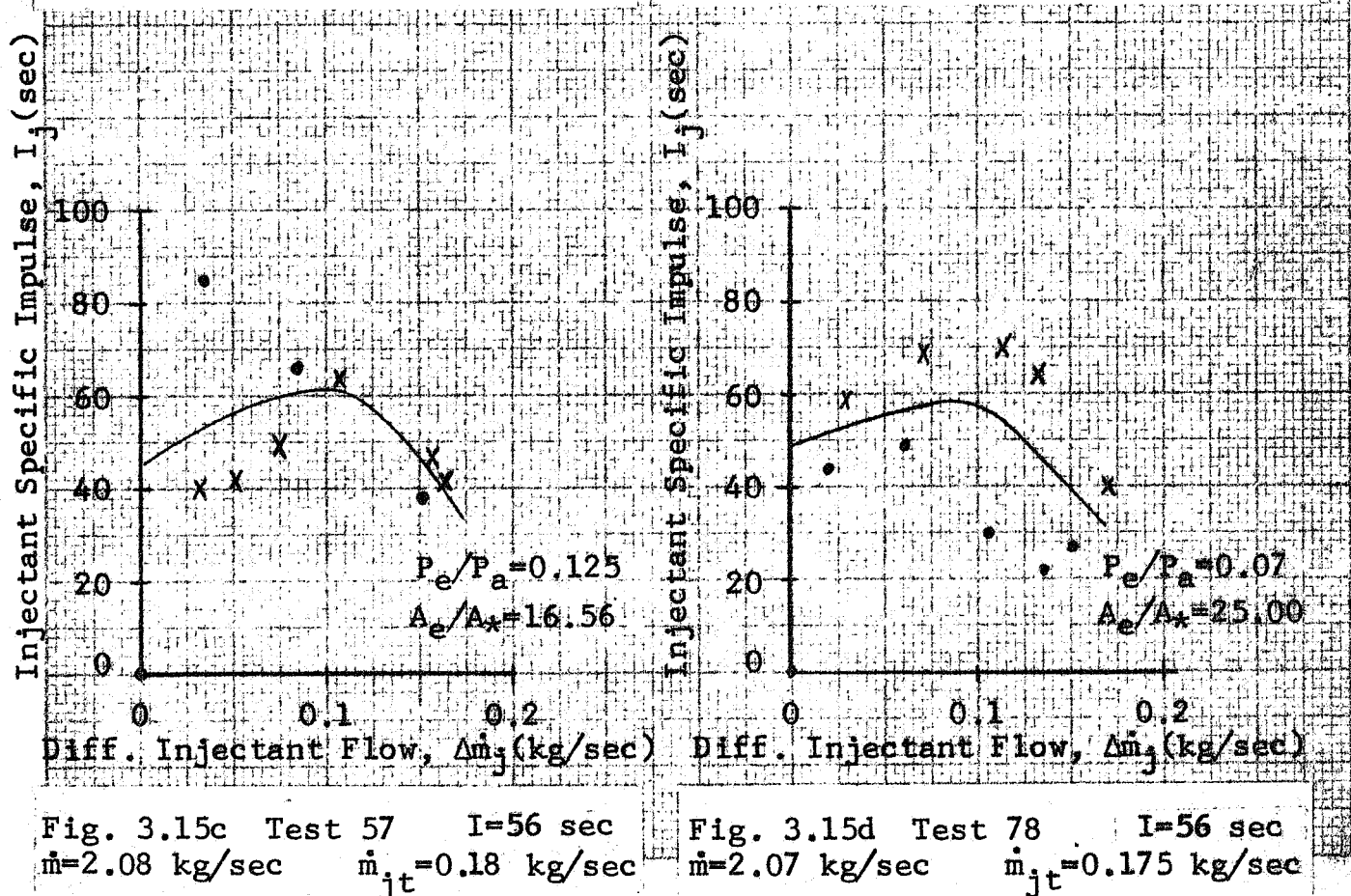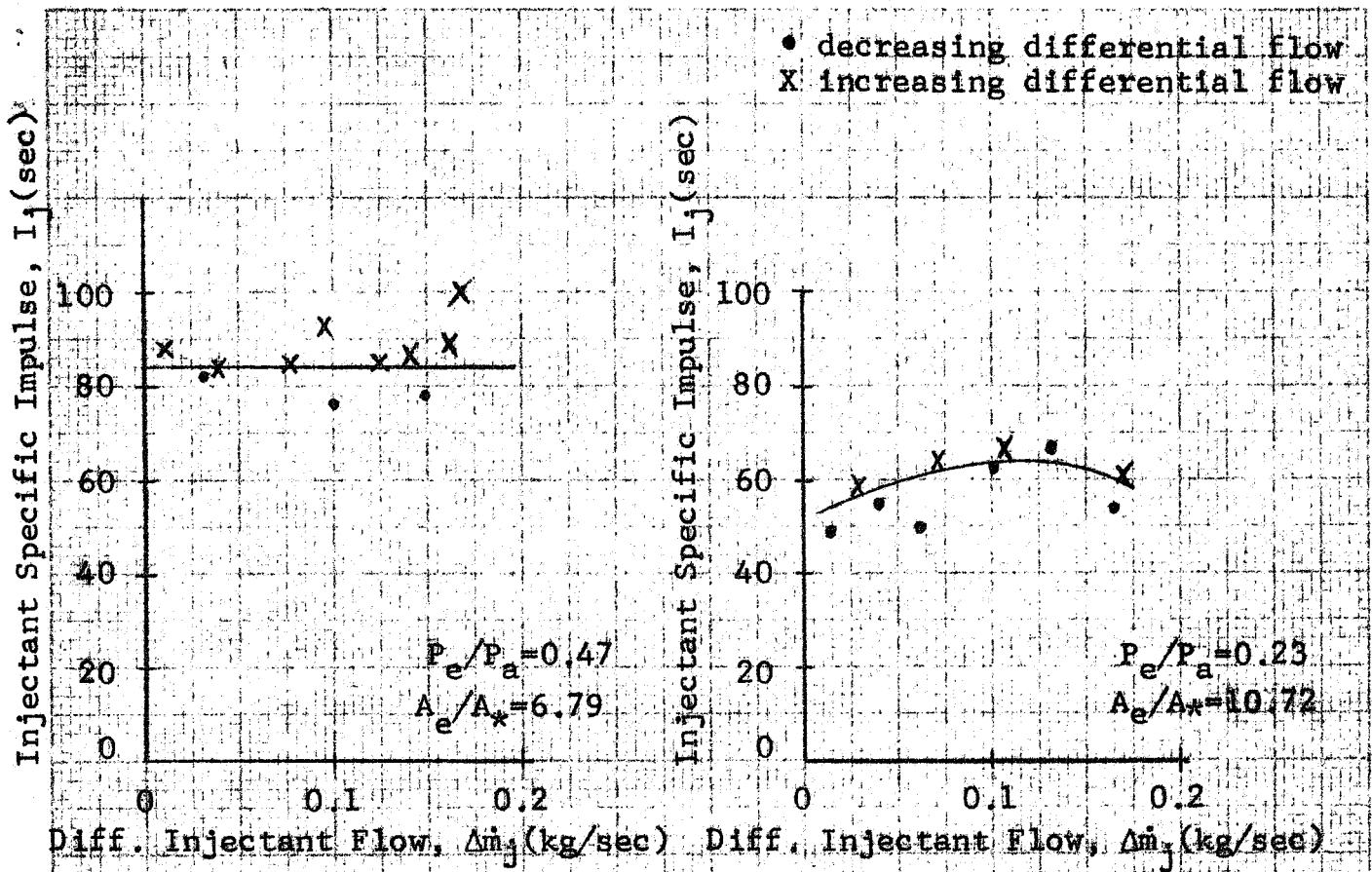Fig. 3.13c   Test 55   I=56 sec
$\dot{m}$=2.14 kg/sec $\dot{m}_{jt}$=0.27 kg/sec

Fig. 3.13d   Test 76   I=56 sec
$\dot{m}$=2.13 kg/sec $\dot{m}_{jt}$=0.27 kg/sec

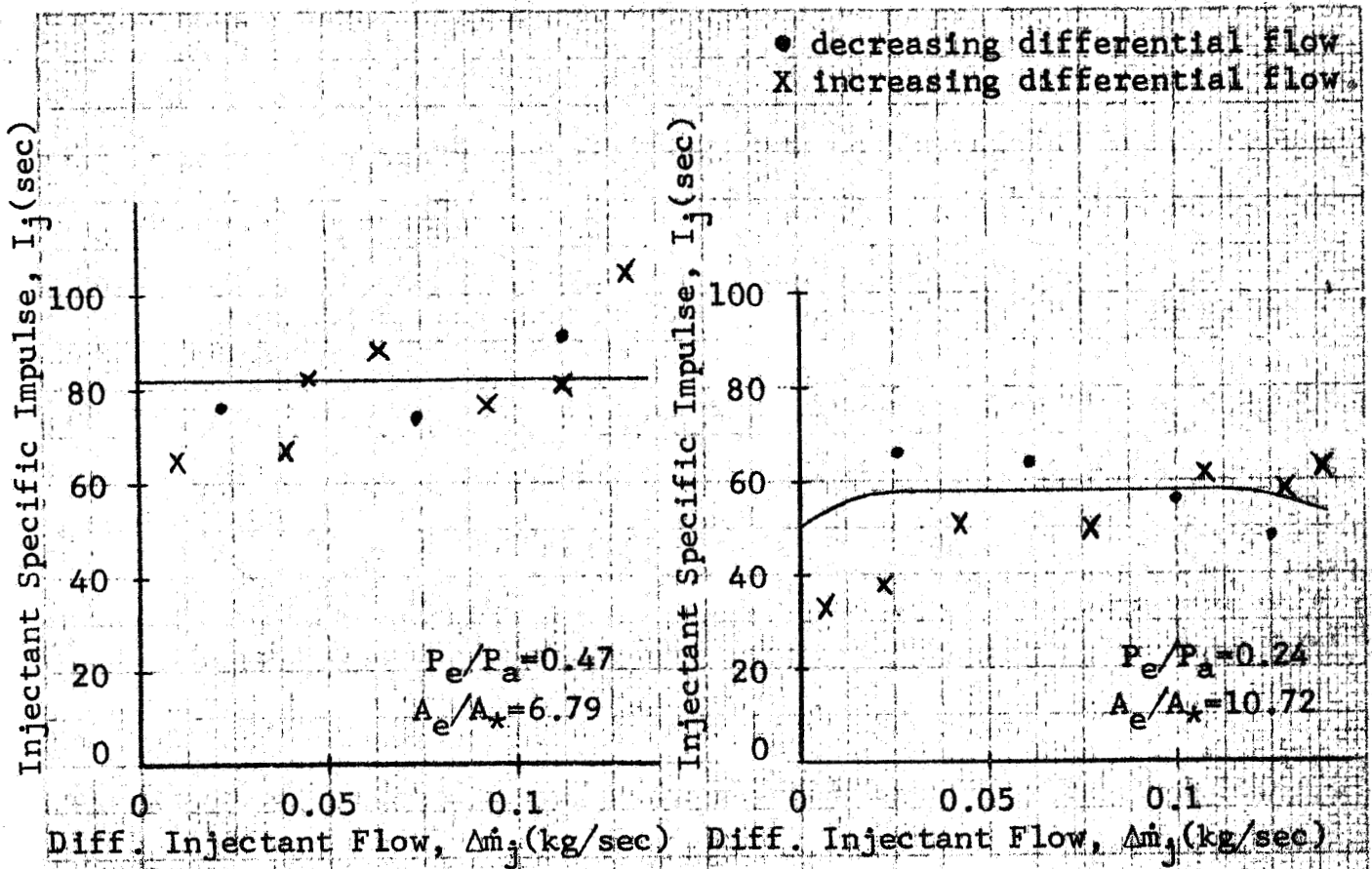Fig. 3.14a Test 14   I=61 sec
$\dot{m}$=2.14 kg/sec $\dot{m}_{jt}$=0.23 kg/sec

Fig. 3.14b Test 35   I=58 sec
$\dot{m}$=2.07 kg/sec $\dot{m}_{jt}$=0.22 kg/sec

Fig. 3.14c Test 56   I=56 sec
$\dot{m}$=2.14 kg/sec $\dot{m}_{jt}$=0.23 kg/sec

Fig. 3.14d Test 77   I=56 sec
$\dot{m}$=2.07 kg/sec $\dot{m}_{jt}$=0.215 kg/sec

Fig. 3.15a   Test 15   I=61 sec
$\dot{m}$=2.11 kg/sec $\dot{m}_{jt}$=0.19 kg/sec

Fig. 3.15b   Test 36   I=58 sec
$\dot{m}$=2.05 kg/sec $\dot{m}_{jt}$=0.175 kg/sec
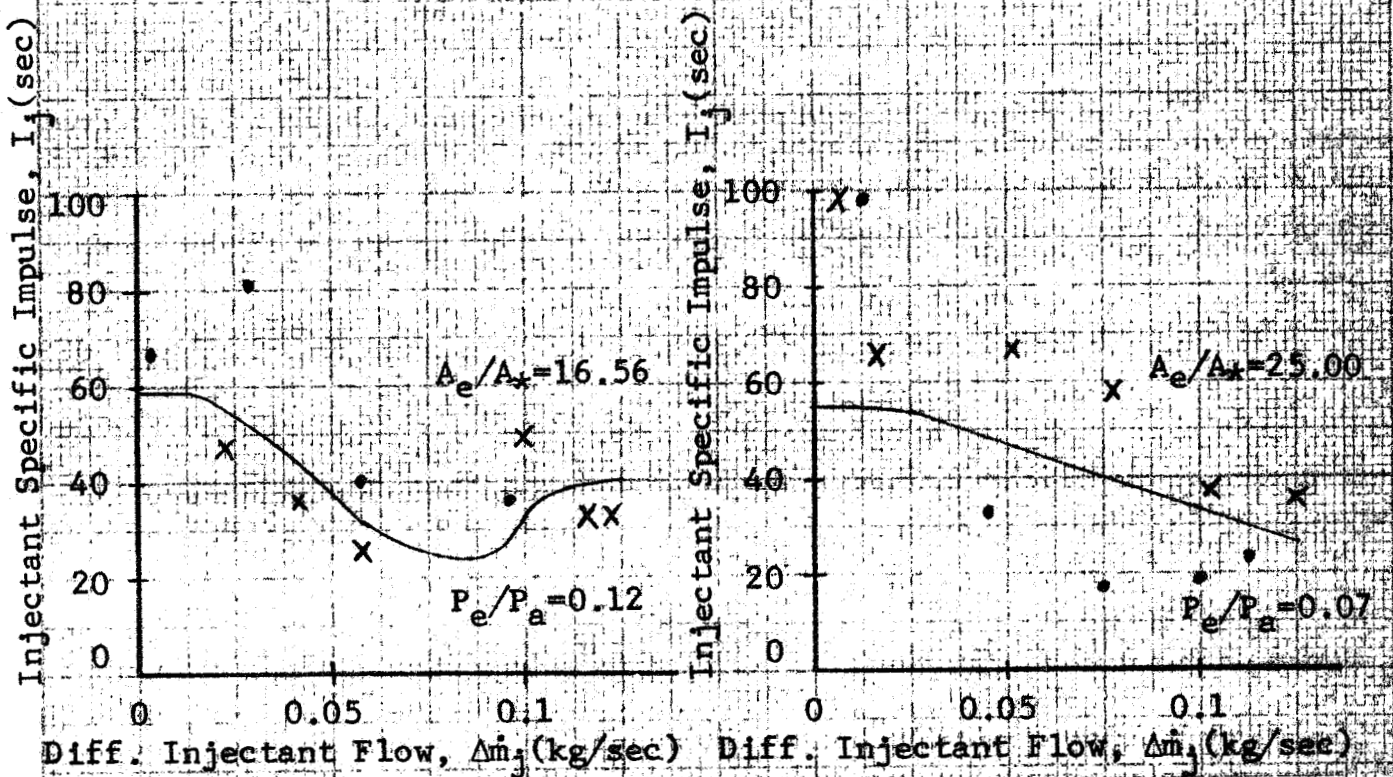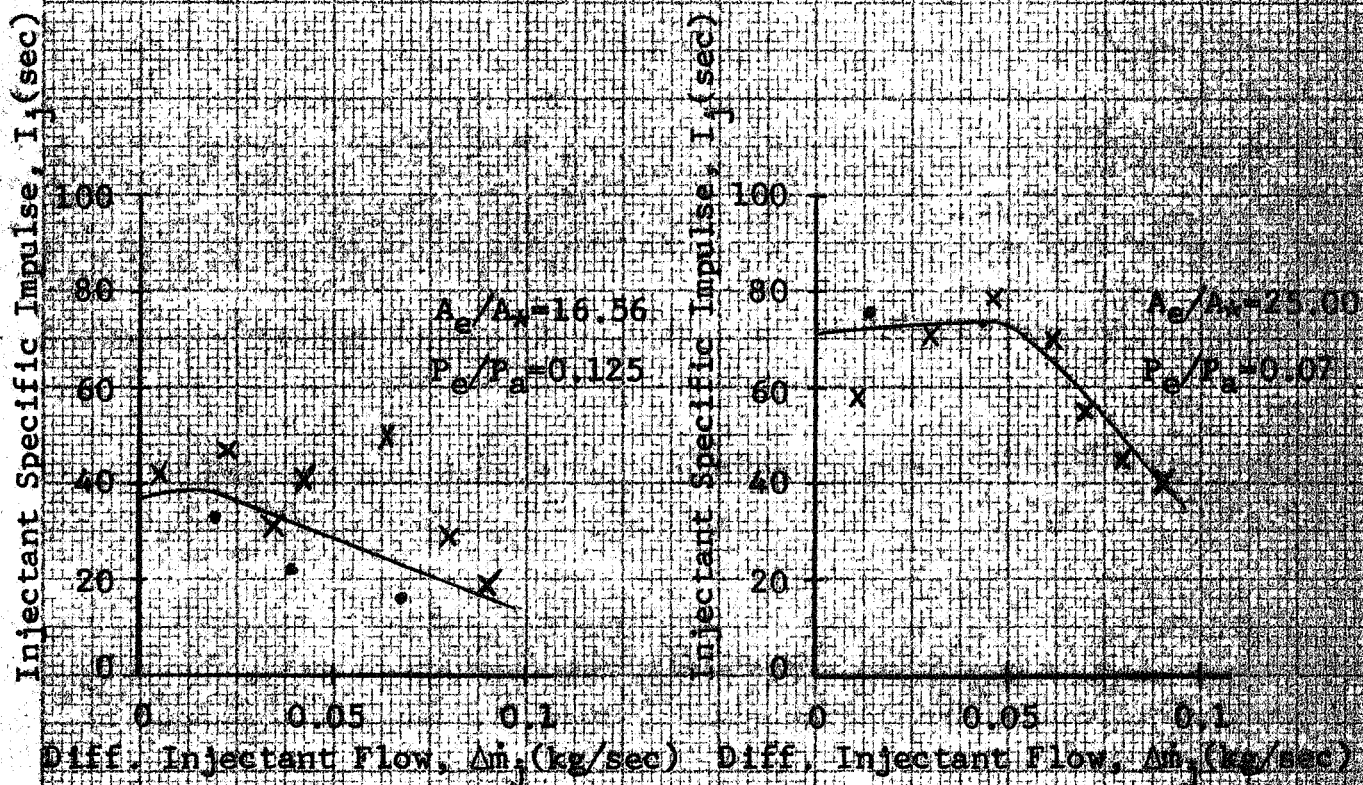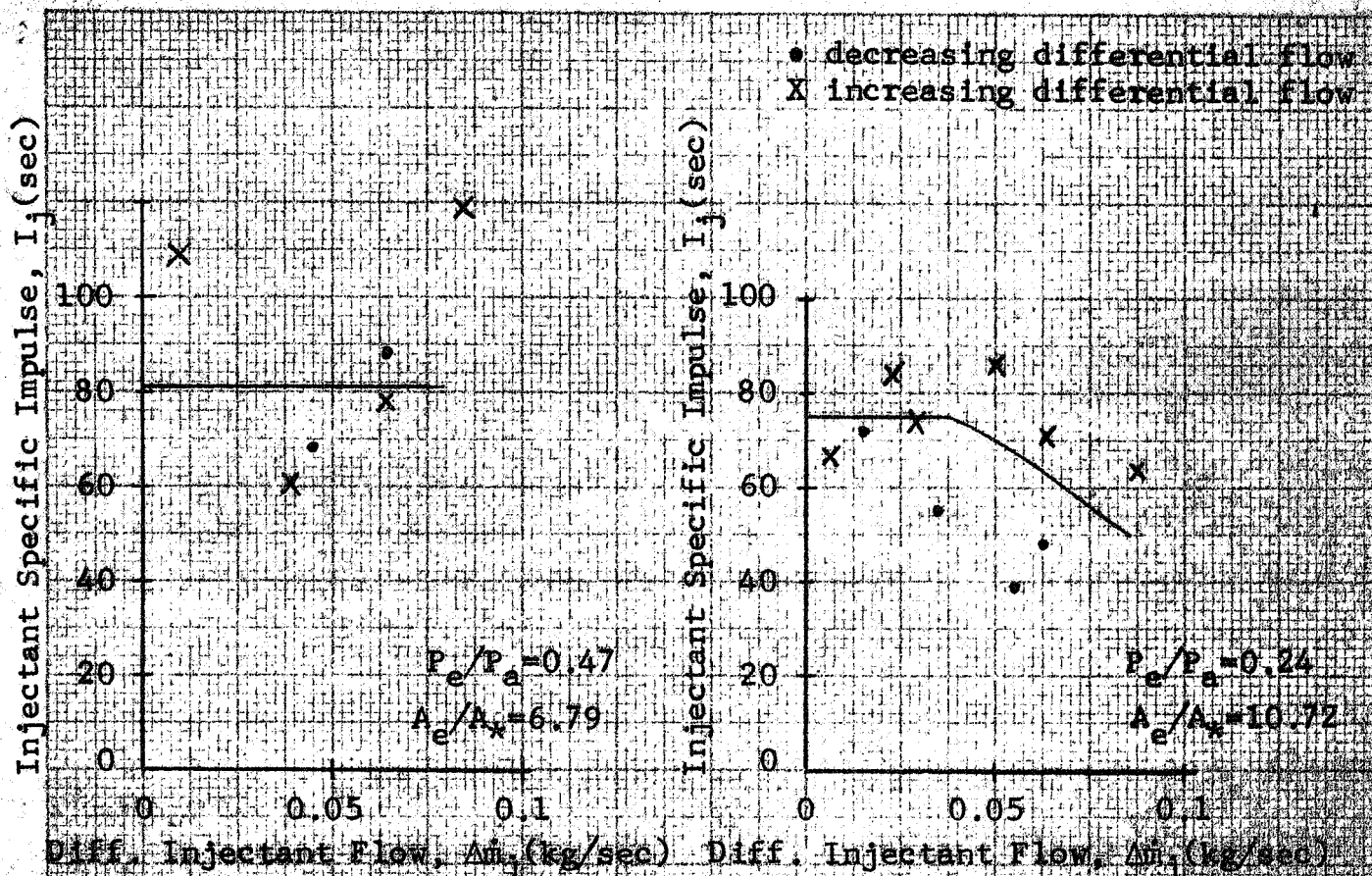
Fig. 3.15c   Test 57   I=56 sec
$\dot{m}$=2.08 kg/sec $\dot{m}_{jt}$=0.18 kg/sec

Fig. 3.15d   Test 78   I=56 sec
$\dot{m}$=2.07 kg/sec $\dot{m}_{jt}$=0.175 kg/sec

Fig. 3.16a Test 16   I=61 sec
ṁ=2.11 kg/sec   ṁ$_{jt}$=0.14 kg/sec

Fig. 3.16b Test 37   I=58 sec
ṁ=2.10 kg/sec   ṁ$_{jt}$=0.14 kg/sec

Fig. 3.16c Test 58   I=56 sec
ṁ=2.05 kg/sec   ṁ$_{jt}$=0.13 kg/sec

Fig. 3.16d Test 79   I=56 sec
ṁ=2.01 kg/sec   ṁ$_{jt}$=0.13 kg/sec

Fig. 3.17a Test 17   I=61 sec
$\dot{m}$=2.11 kg/sec $\dot{m}_{jt}$=0.09 kg/sec

Fig. 3.17b Test 38   I=58 sec
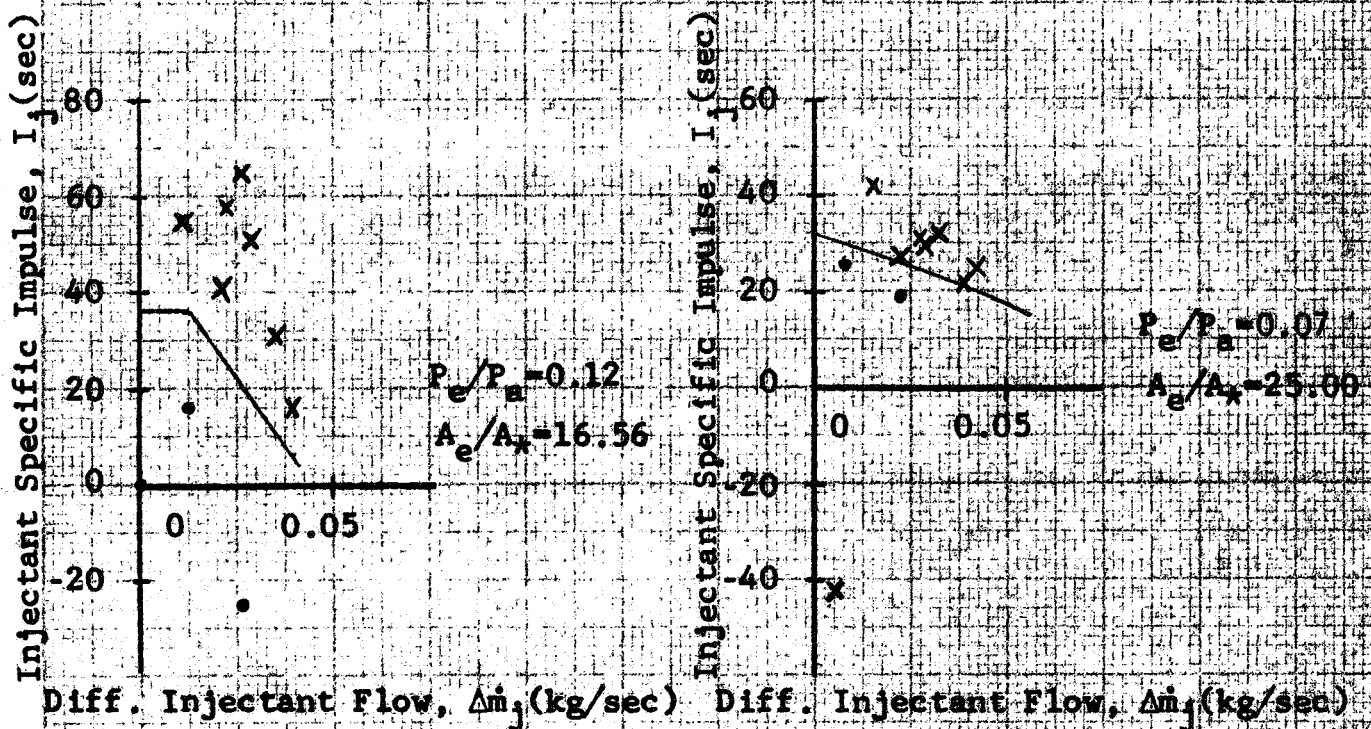$\dot{m}$=2.10 kg/sec $\dot{m}_{jt}$=0.085 kg/sec
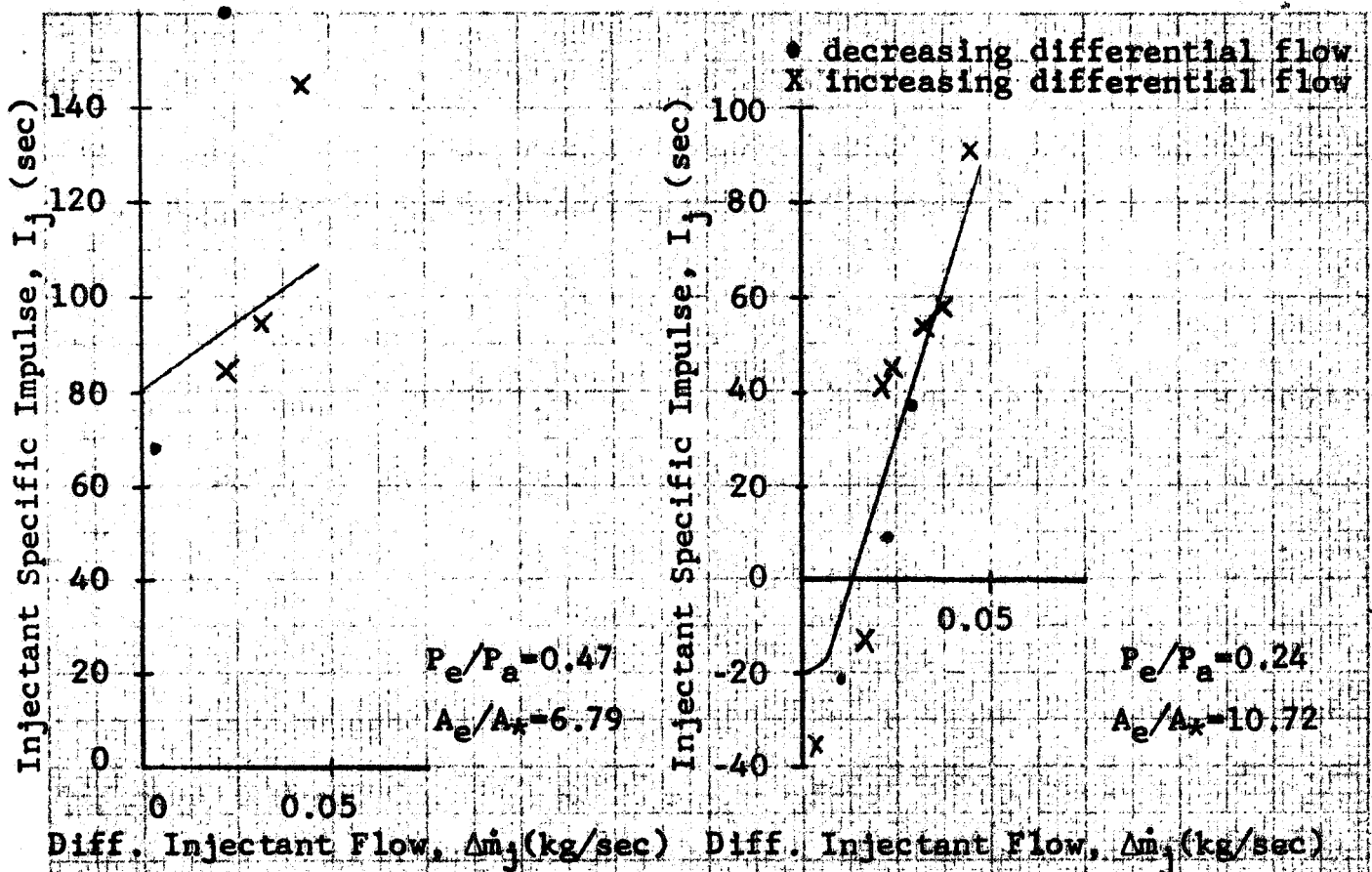
Fig. 3.17c Test 59   I=56 sec
$\dot{m}$=2.15 kg/sec $\dot{m}_{it}$=0.09 kg/sec

Fig. 3.17d Test 80   I=56 sec
$\dot{m}$=2.08 kg/sec $\dot{m}_{jt}$=0.09 kg/sec

Fig. 3.18a Test 18   I=61 sec
$\dot{m}$=2.11 kg/sec $\dot{m}_{jt}$=0.05 kg/sec

Fig. 3.18b Test 39   I=58 sec
$\dot{m}$=2.12 kg/sec $\dot{m}_{jt}$=0.05 kg/sec

Fig. 3.18c Test 60   I=56 sec
$\dot{m}$=2.12 kg/sec $\dot{m}_{jt}$=0.045 kg/sec

Fig. 3.18d Test 81   I=56 sec
$\dot{m}$=2.08 kg/sec $\dot{m}_{jt}$=0.04 kg/sec

Figure 3.19 - Specific Impulse Characteristics With Theoretical Full-Flowing Primary Exit Pressure, $\frac{P_e}{P_a}$, Nominal 0.10 Total Secondary/Primary Flow Ratio
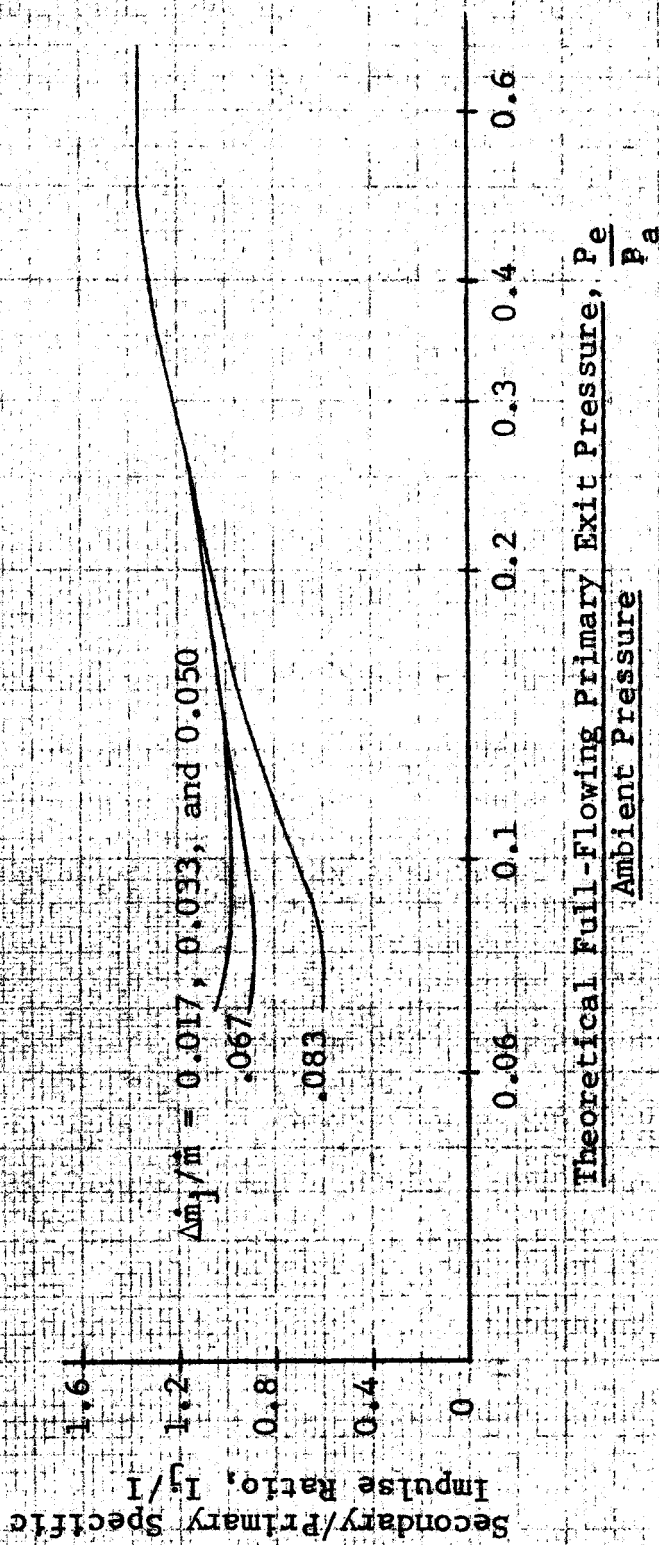
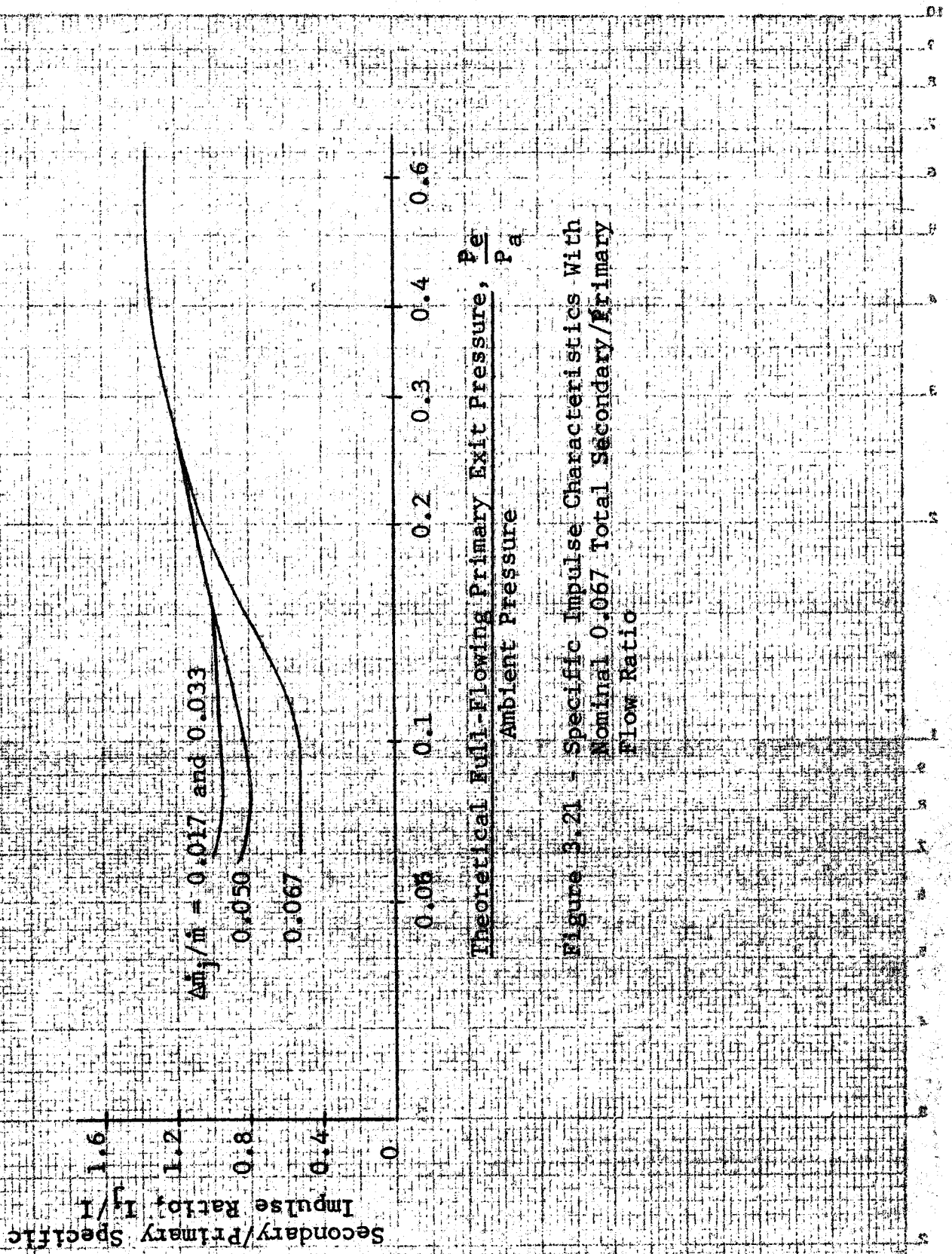Figure 3.20 — Specific Impulse Characteristics With Nominal 0.083 Total Secondary/Primary Flow Ratio

Figure 3.21 - Specific Impulse Characteristics With Nominal 0.067 Total Secondary/Primary Flow Ratio
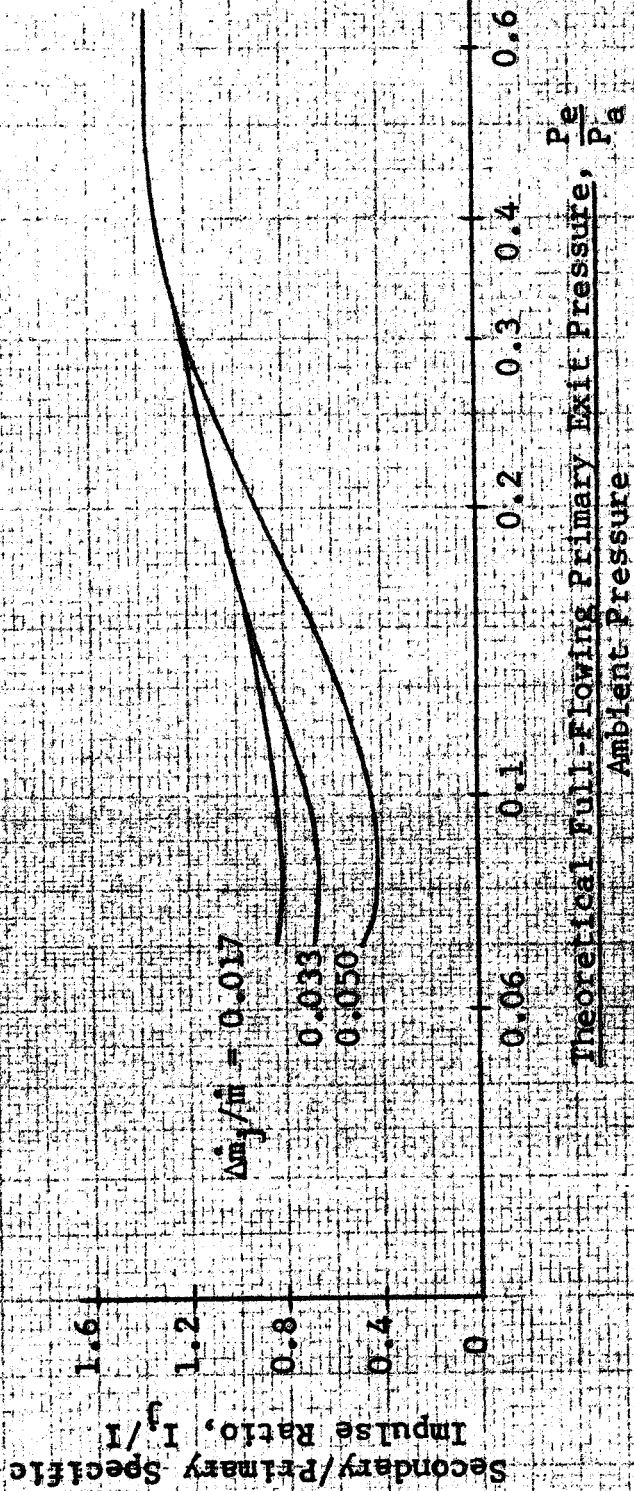
Theoretical Full-Flowing Primary Exit Pressure, $\frac{P_e}{P_a}$

Figure 3.22 - Specific Impulse Characteristics With Nominal 0.050 Total Secondary/Primary Flow Ratio

Figure 3-23 - Specific Impulse Characteristics With Nominal 0.033 Total Secondary/Primary Flow Ratio
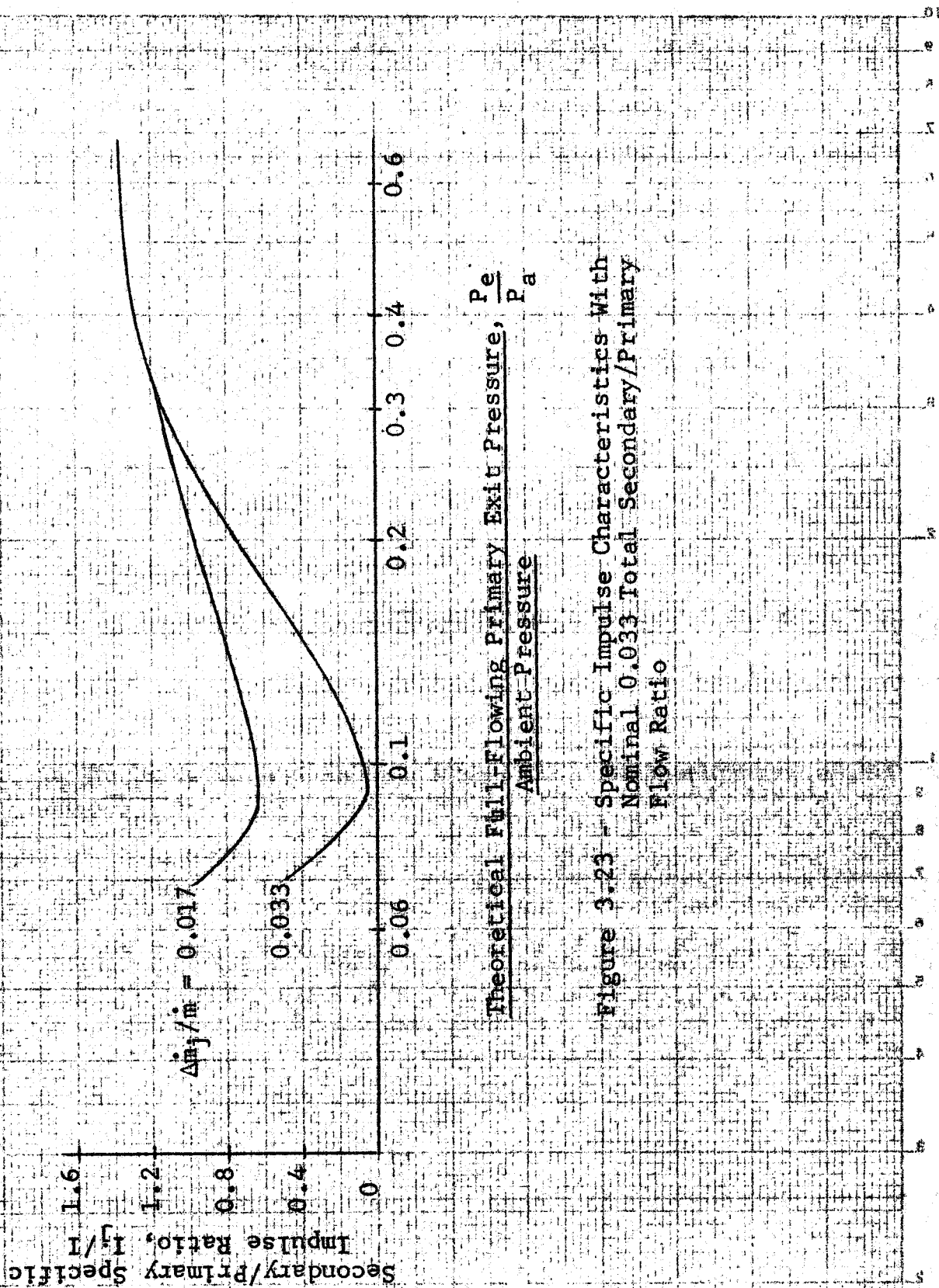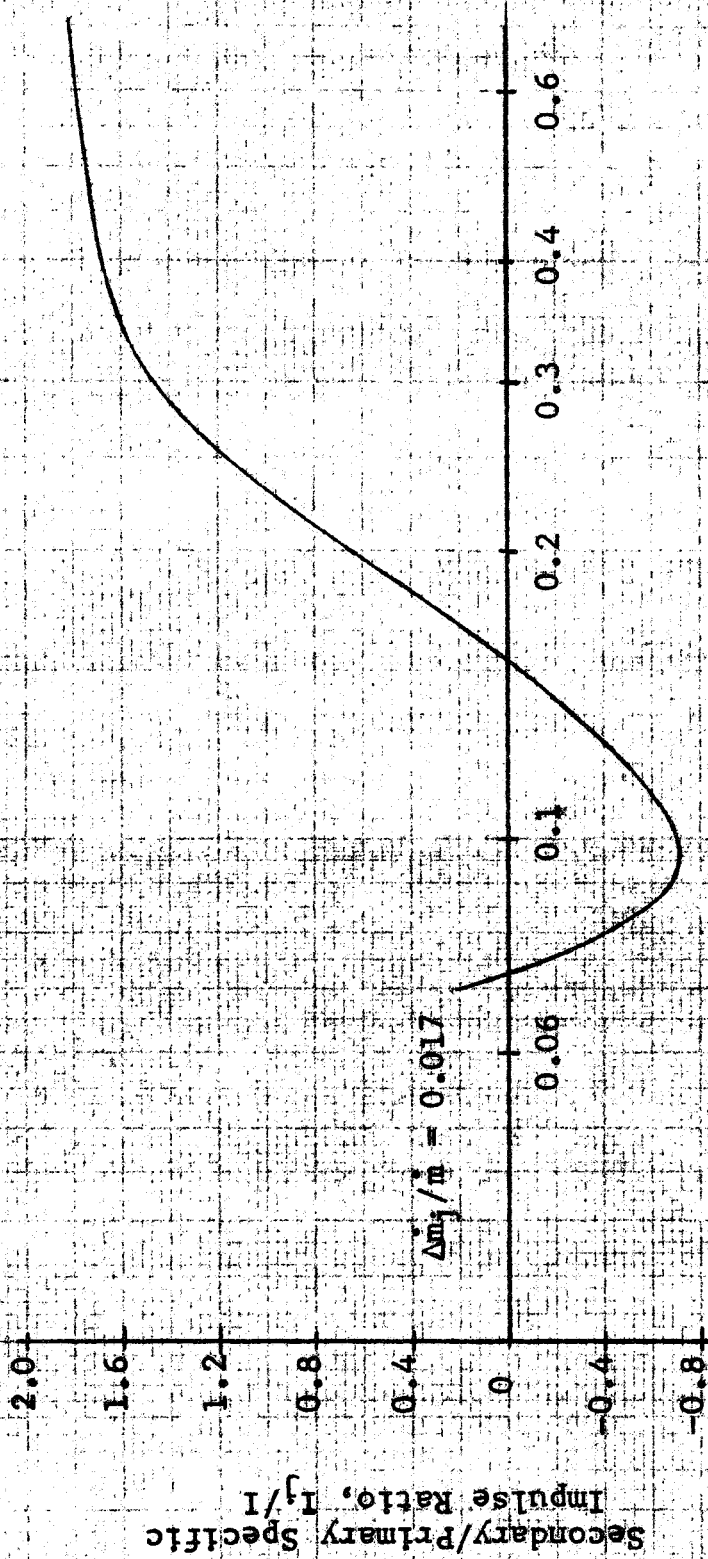
Figure 3.24 — Specific Impulse Characteristics With Nominal 0.017 Total Secondary/Primary Flow Ratio

Theoretical Full-Flowing Primary Exit Pressure, $\frac{P_e}{P_a}$, Ambient Pressure

Theoretical Full-Flowing Primary Exit Pressure, $\frac{P_e}{P_a}$
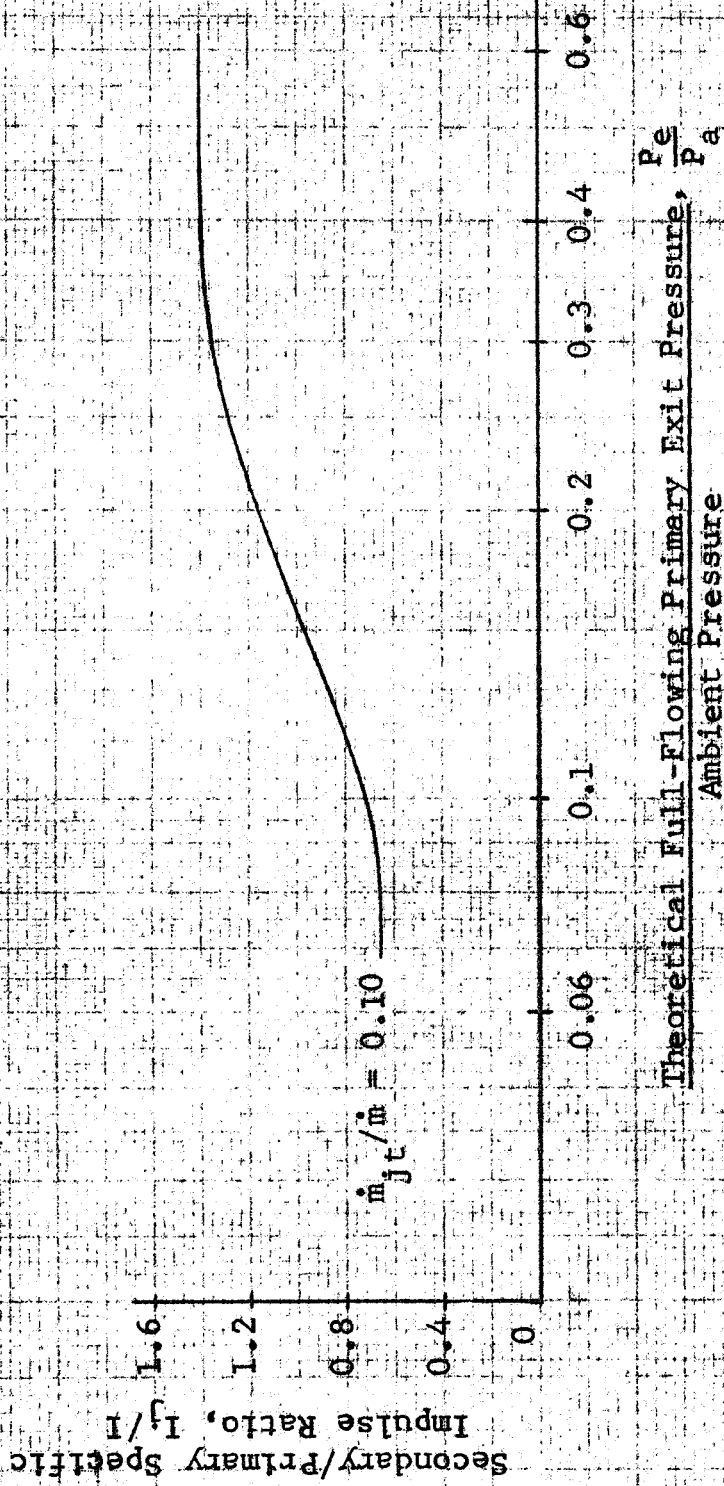Ambient Pressure.

Figure 3.25 - Specific Impulse Characteristics With
Nominal 0.10 Differential Secondary/Primary
Flow Ratio

Figure 3.26 - Specific Impulse Characteristics With Nominal 0.083 Differential Secondary/Primary Flow Ratio.

Theoretical Full-Flowing Primary Exit Pressure, $\frac{P_e}{P_a}$, Ambient Pressure
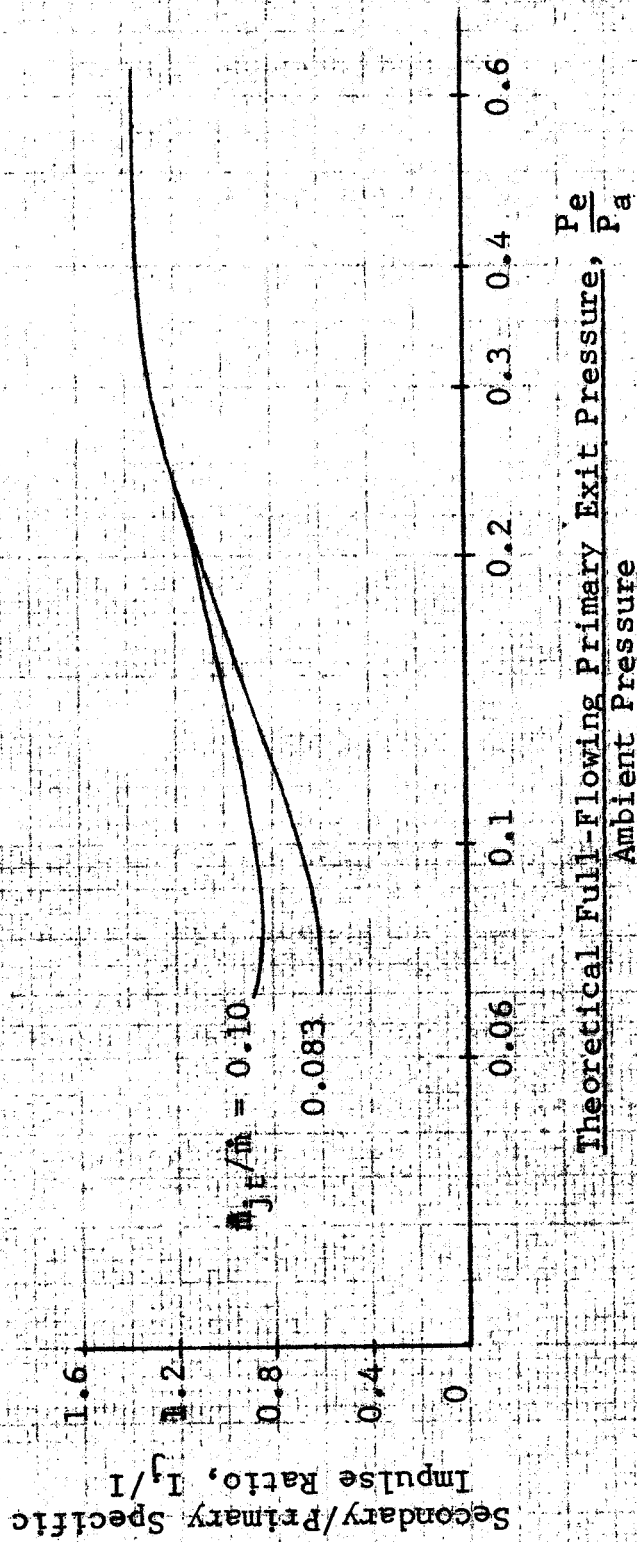
Figure 3.27 . Specific Impulse Characteristics With Nominal
0.067 Differential Secondary/Primary Flow Ratio

Figure 3.28 – Specific Impulse Characteristics With Nominal 0.050 Differential Secondary/Primary Flow Ratio

Figure 3.29.- Specific Impulse Characteristics With Nominal 0.033 Differential Secondary/Primary Flow Ratio
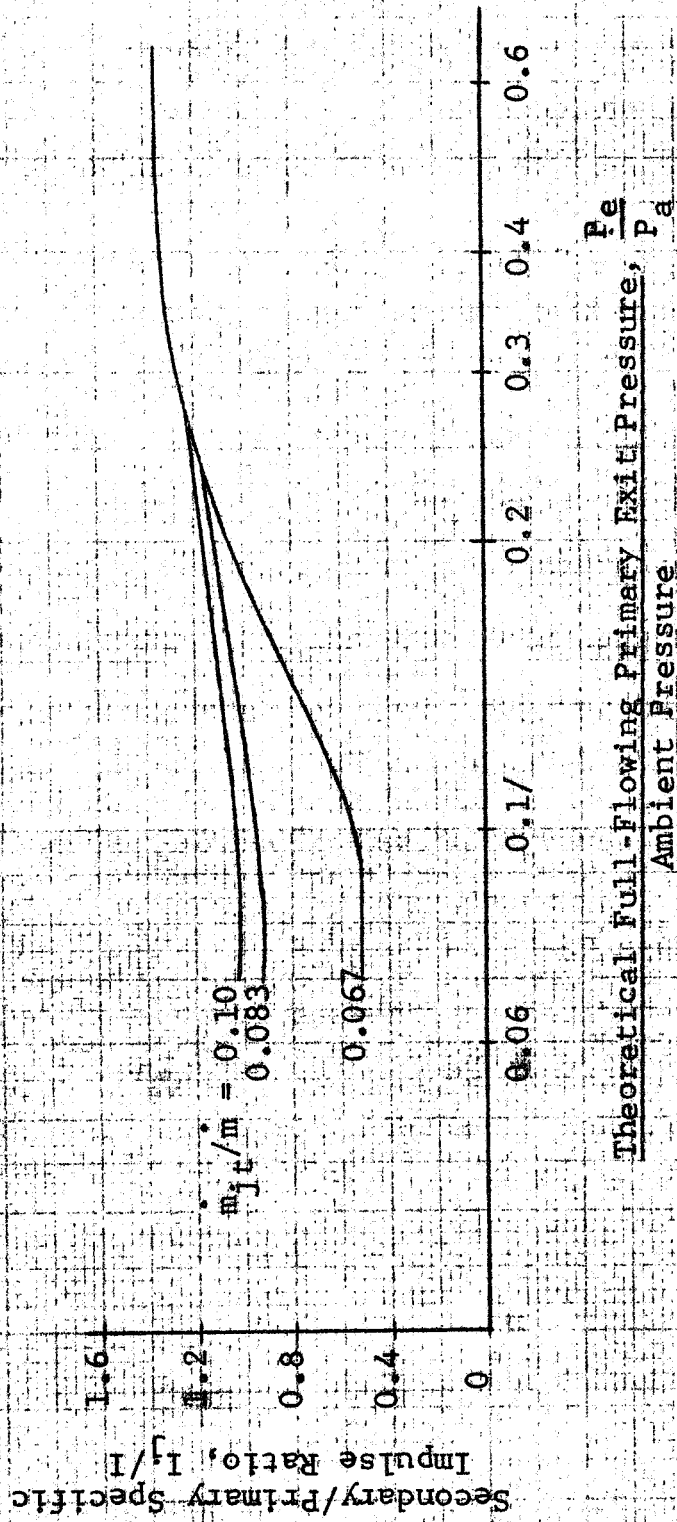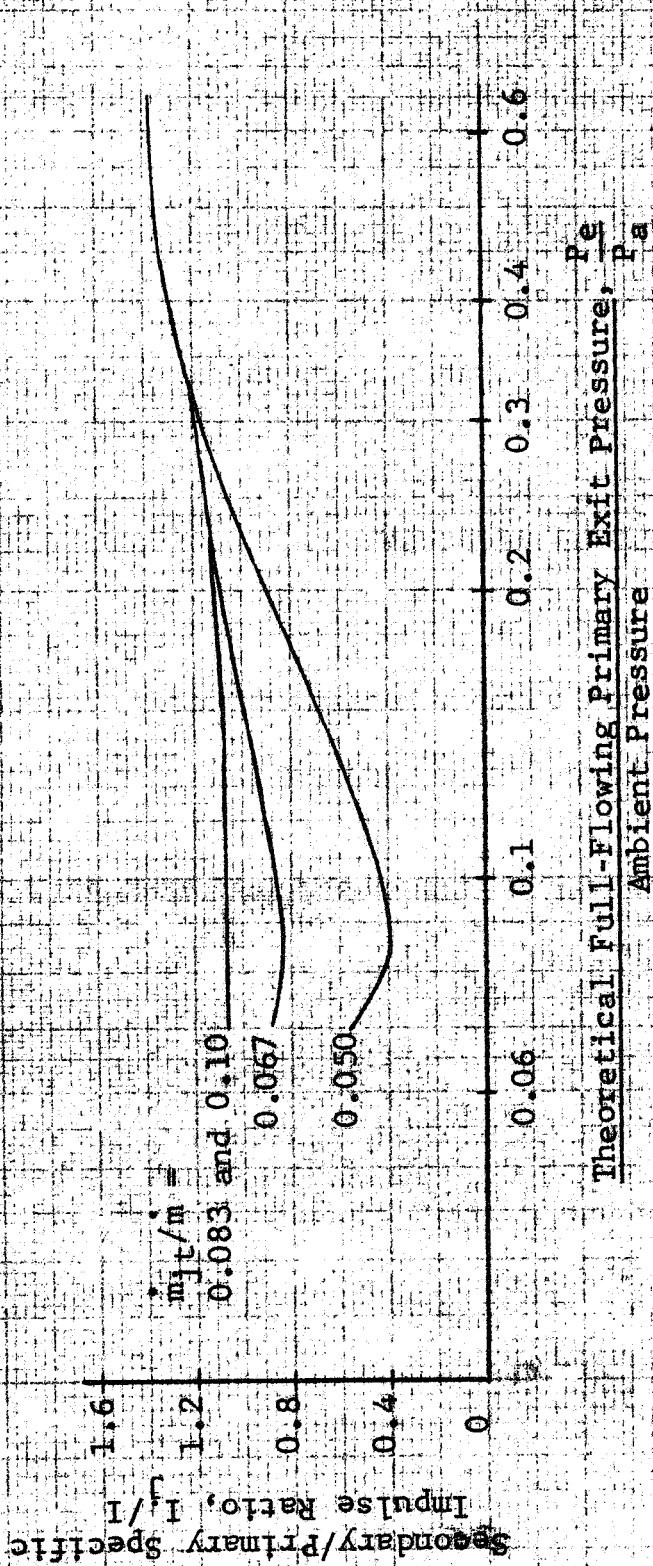
Figure 3.30 - Specific Impulse Characteristics With Nominal
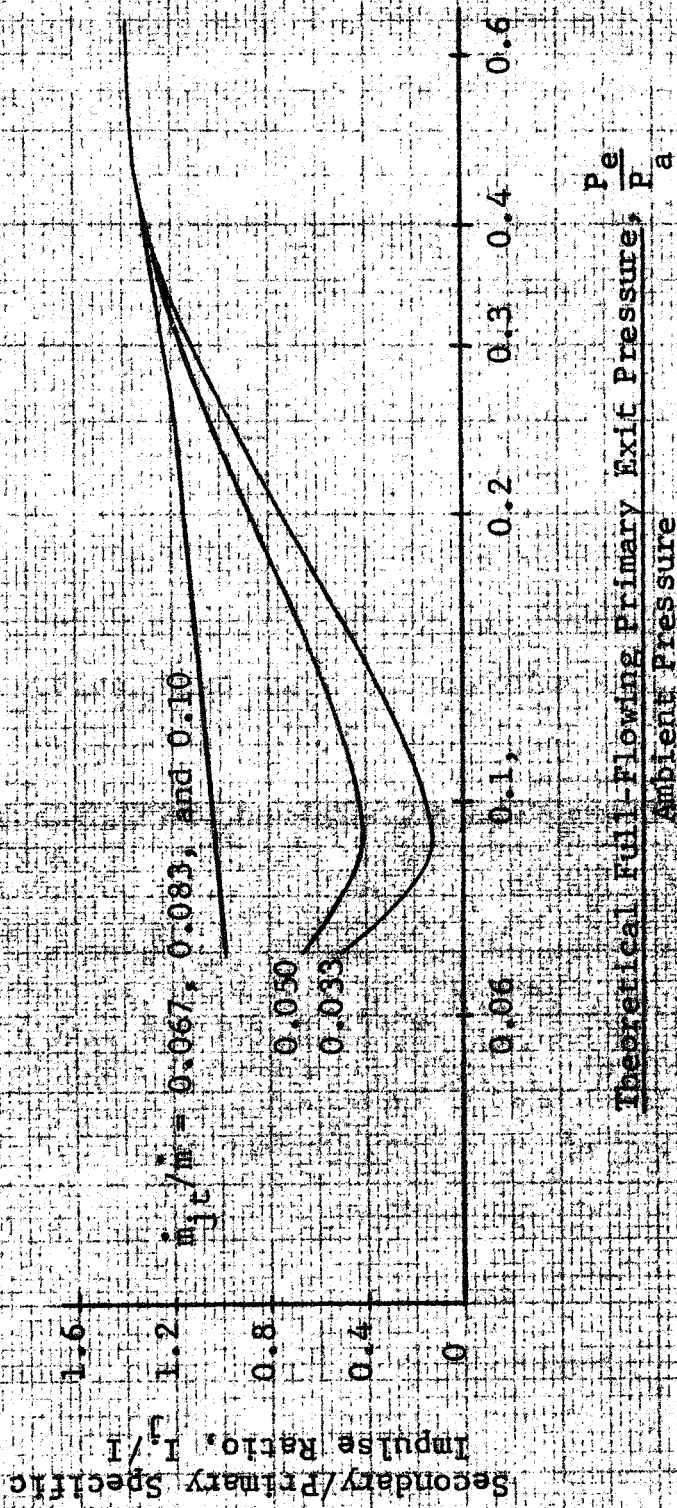0.017 Differential Secondary/Primary Flow Ratio

Fig. 3.31a   Test 19   I=63 sec
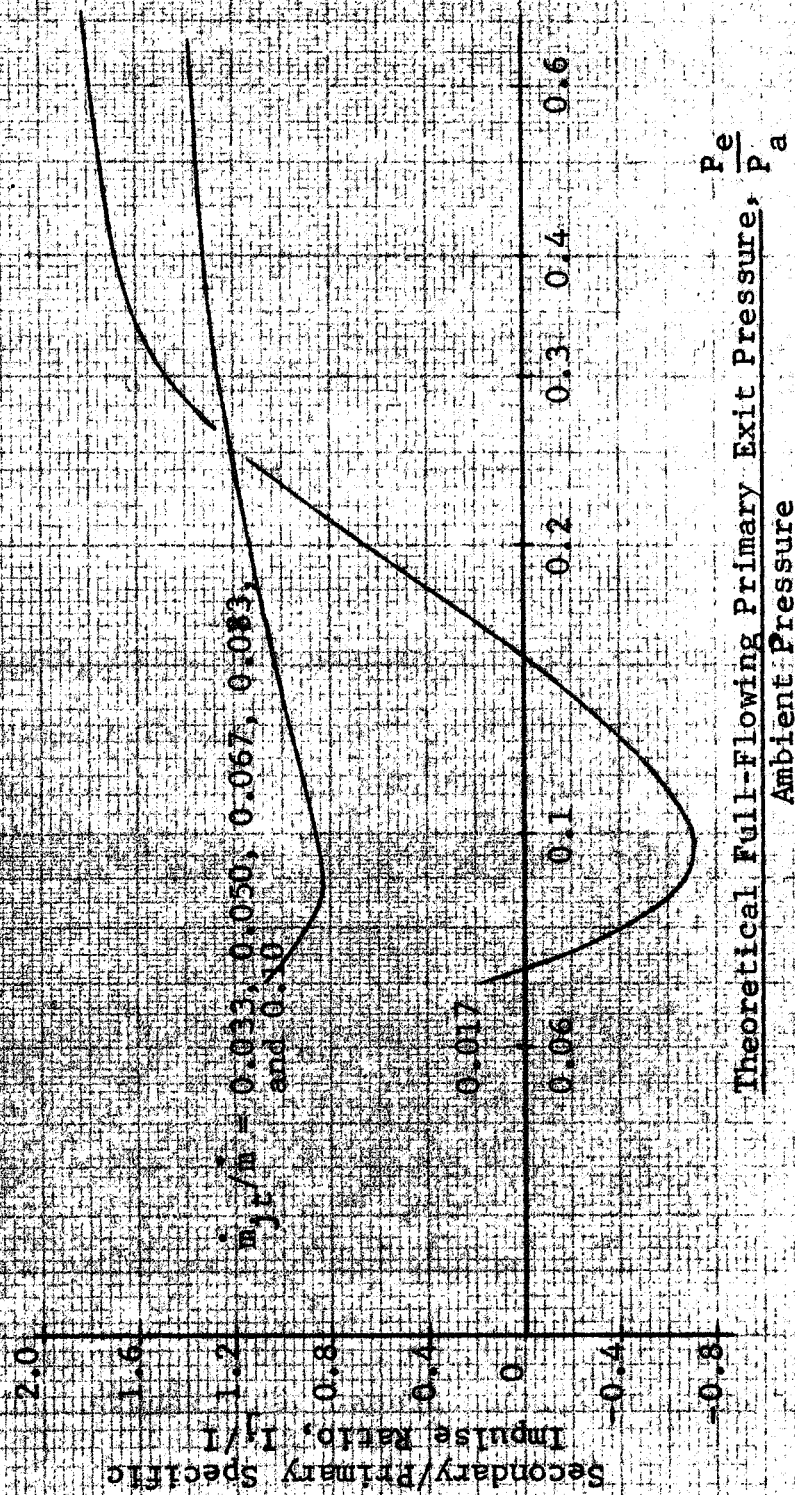ṁ=2.91 kg/sec P_e/P_a=0.63
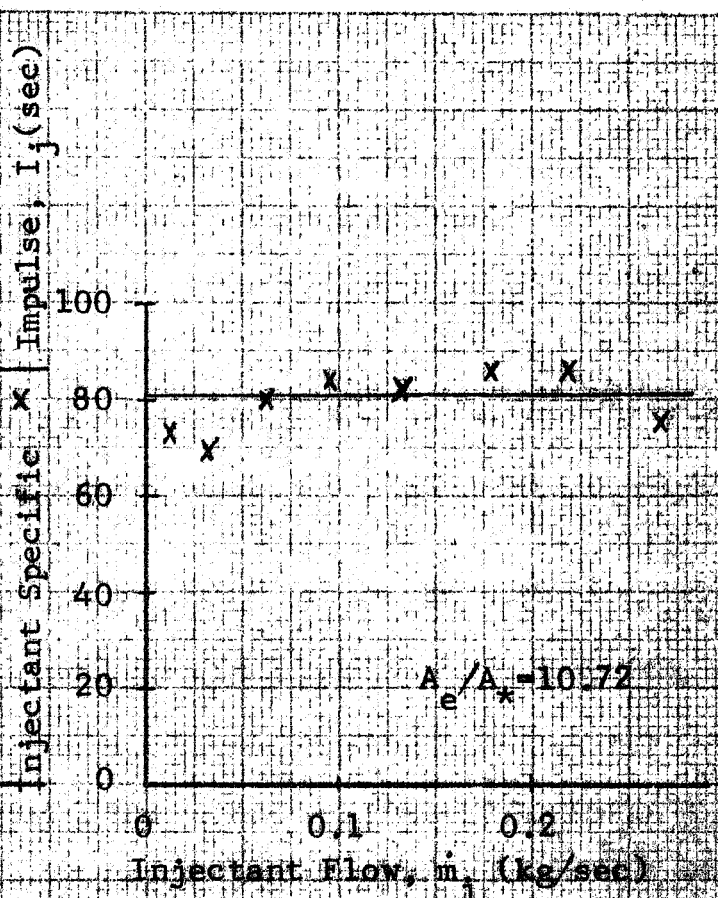
Fig. 3.31b   Test 40   I=60 sec
ṁ=3.07 kg/sec P_e/P_a=0.33
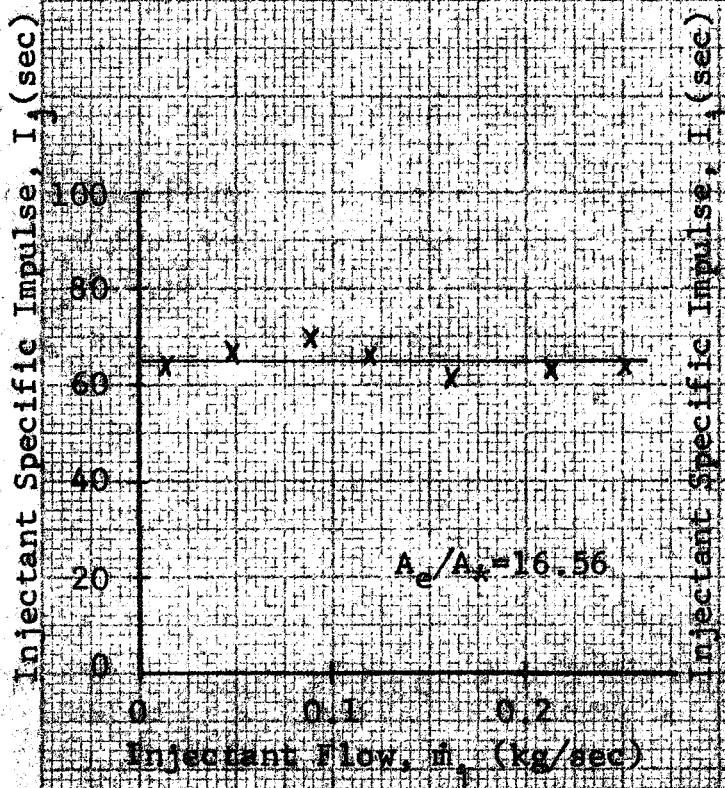
Fig. 3.31c   Test 61   I=56 sec
ṁ=2.89 kg/sec P_e/P_a=0.17

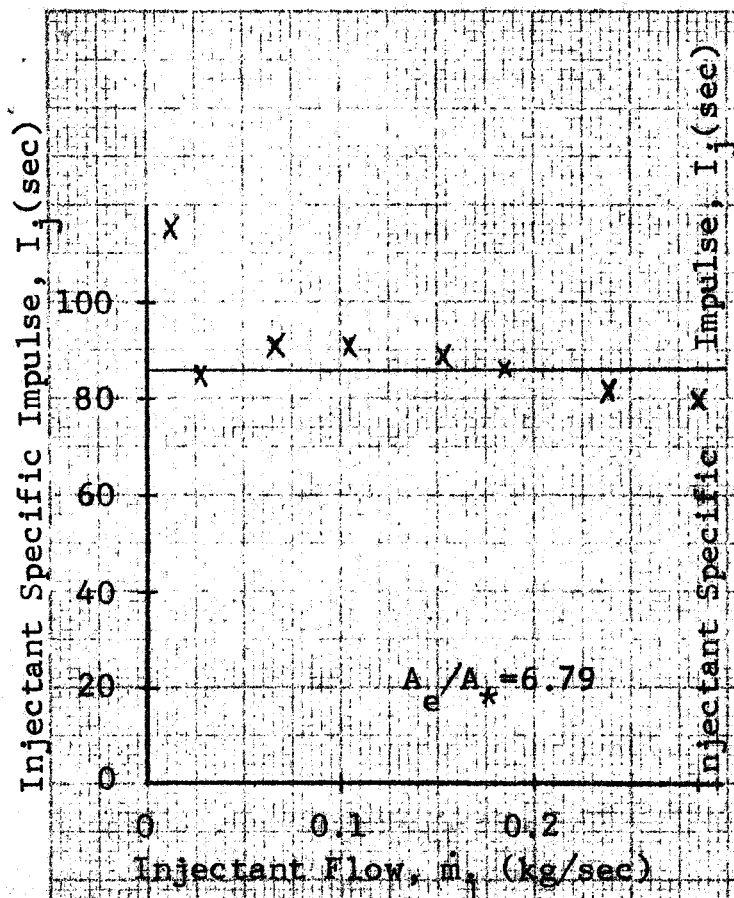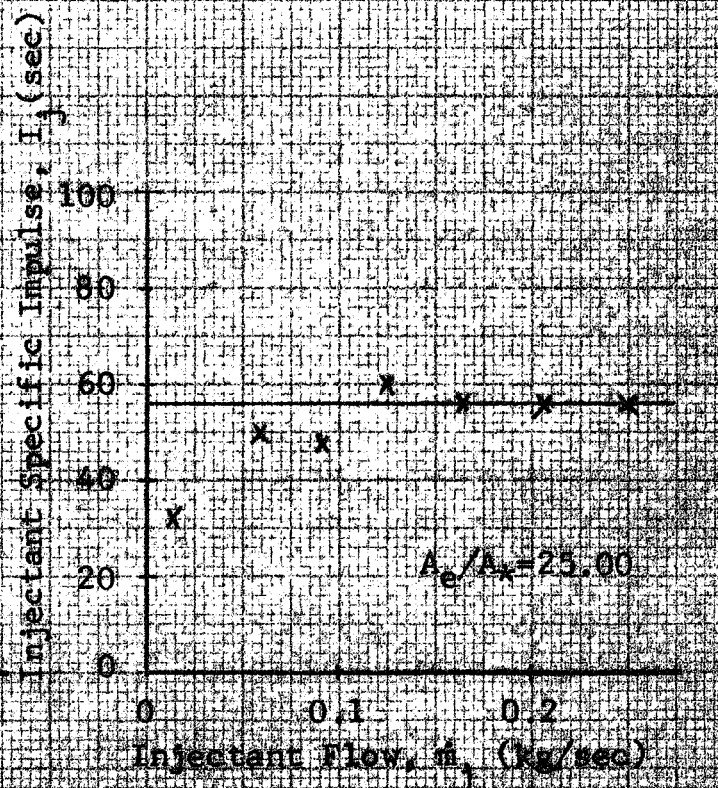Fig. 3.31d   Test 82   I=56 sec
ṁ=2.81 kg/sec P_e/P_a=0.09
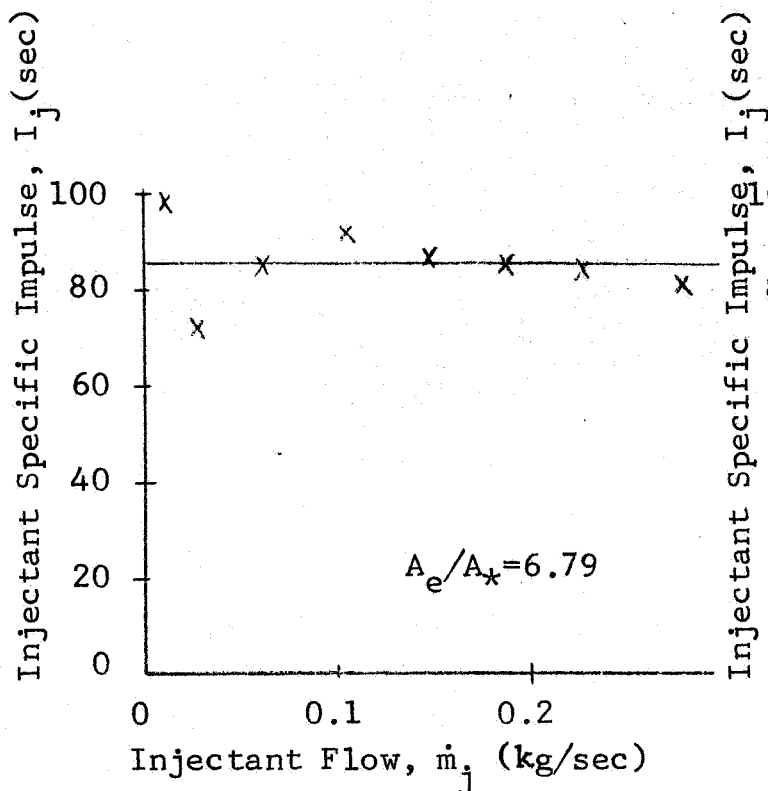
Fig. 3.32a Test 20 I=62 sec
$\dot{m}$=2.49 kg/sec P_e/P_a=0.55
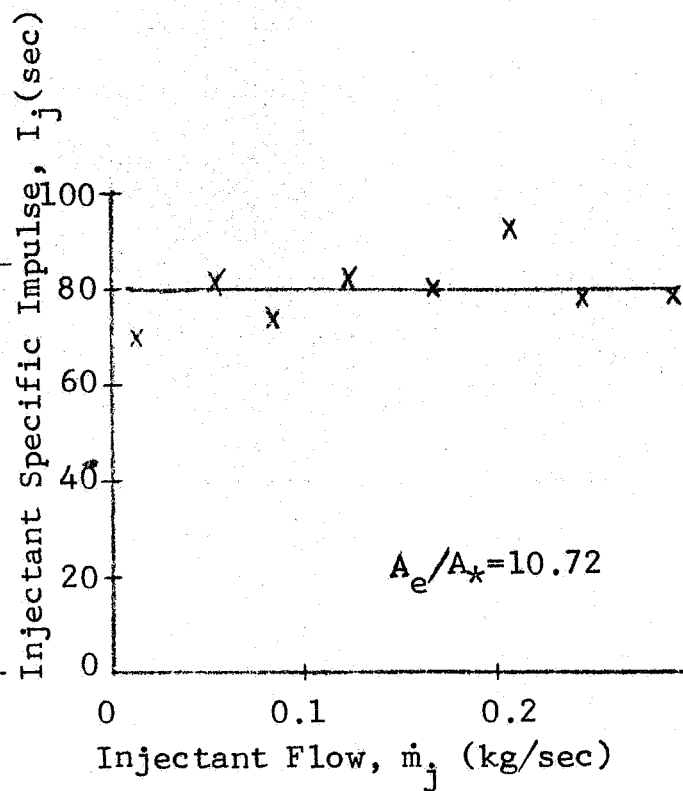
Fig. 3.32b Test 41 I=59 sec
$\dot{m}$=2.57 kg/sec P_e/P_a=0.28
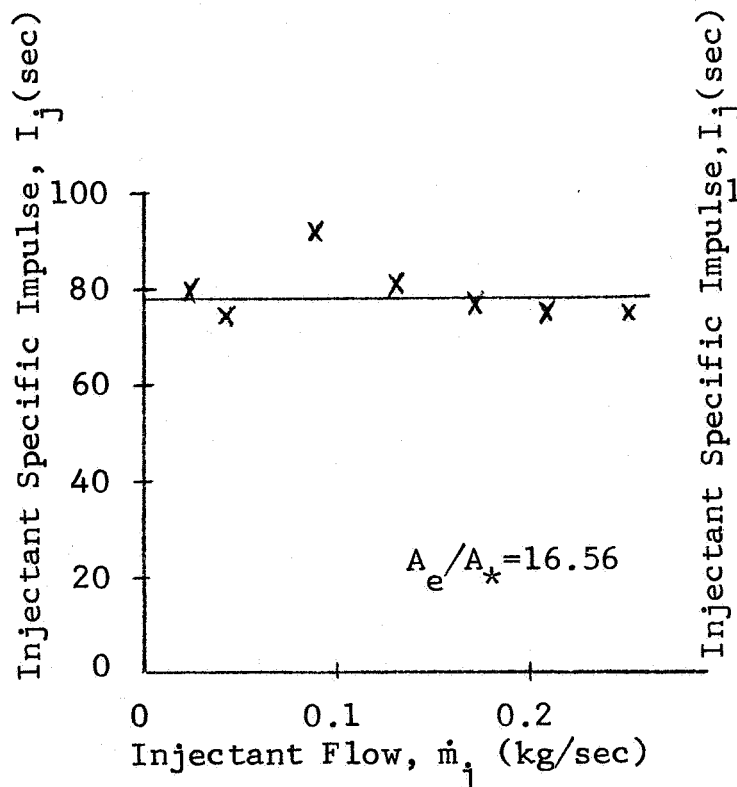
Fig. 3.32c Test 62 I=56 sec
$\dot{m}$=2.45 kg/sec P_e/P_a=0.15
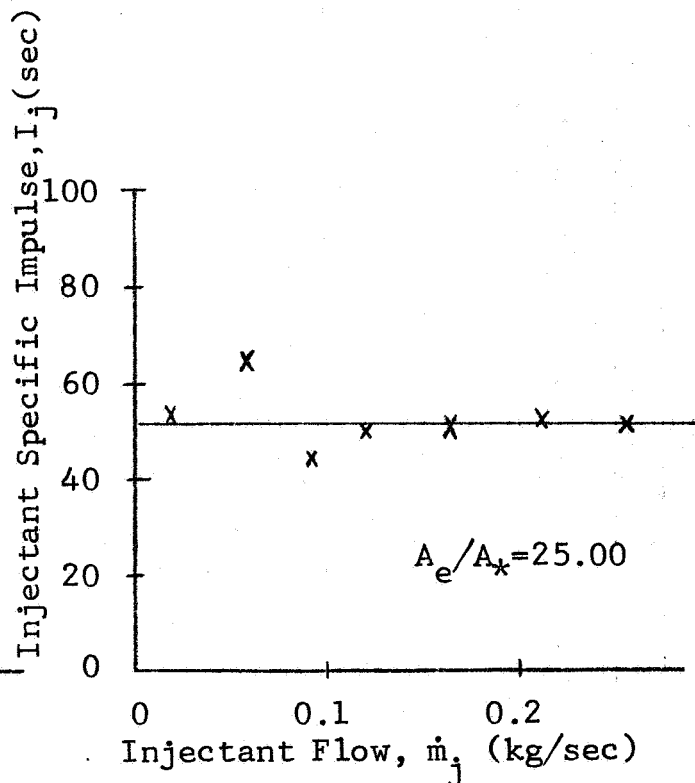
Fig. 3.32d Test 83 I=56 sec
$\dot{m}$=2.47 kg/sec P_e/P_a=0.08
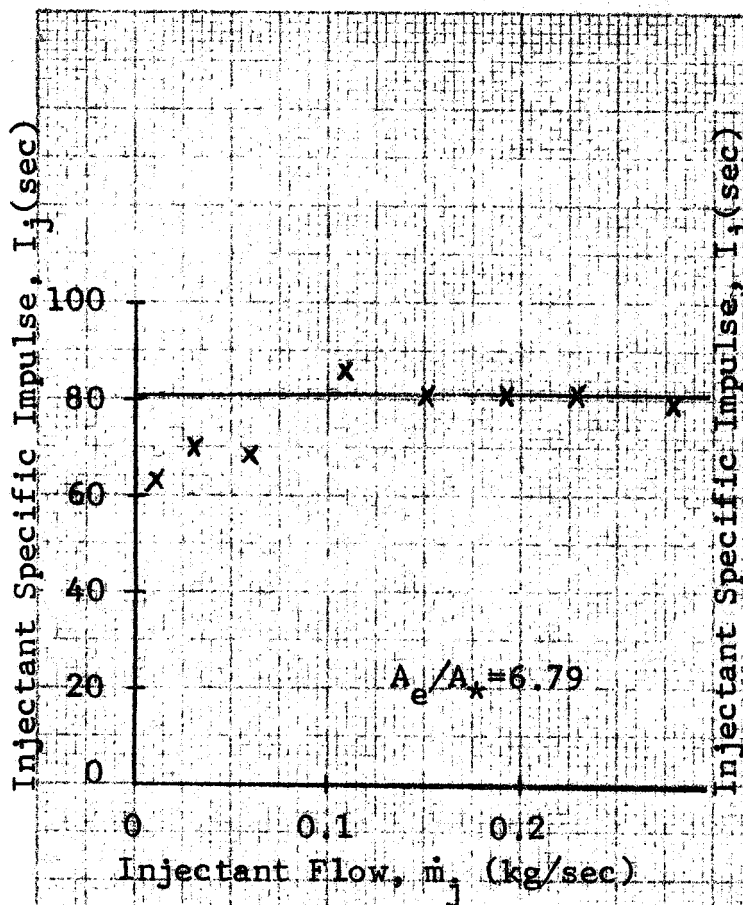
Fig. 3.33a Test 21 I=61 sec
ṁ=2.08 kg/sec P_e/P_a=0.47
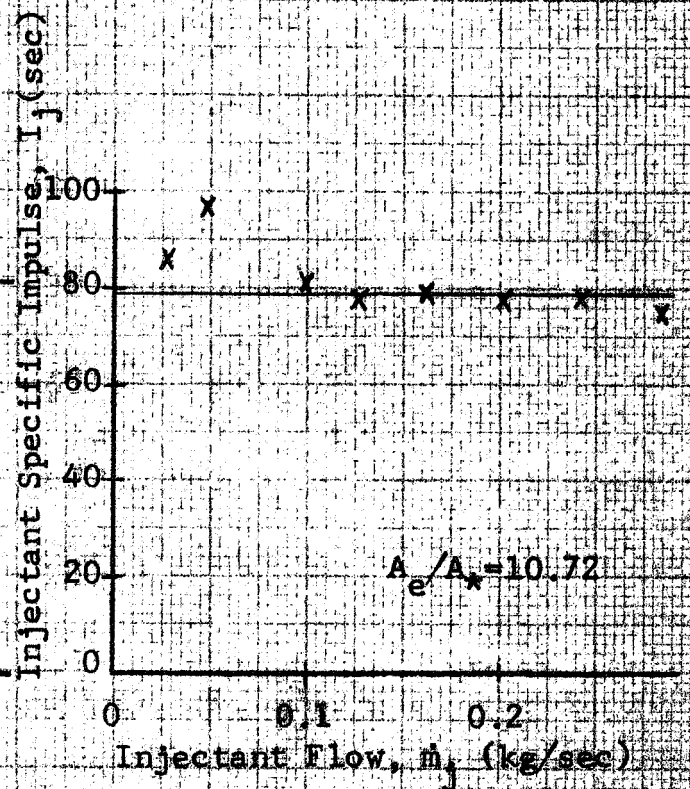
Fig. 3.33b Test 42 I=58 sec
ṁ=2.08 kg/sec P_e/P_a=0.24
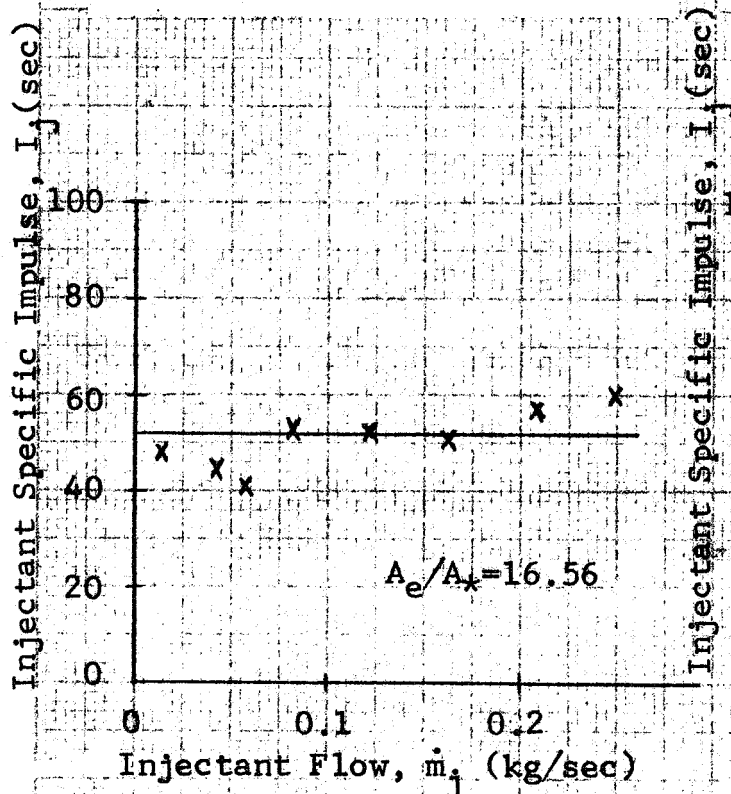
Fig. 3.33c Test 63 I=56 sec
ṁ=2.05 kg/sec P_e/P_a=0.125
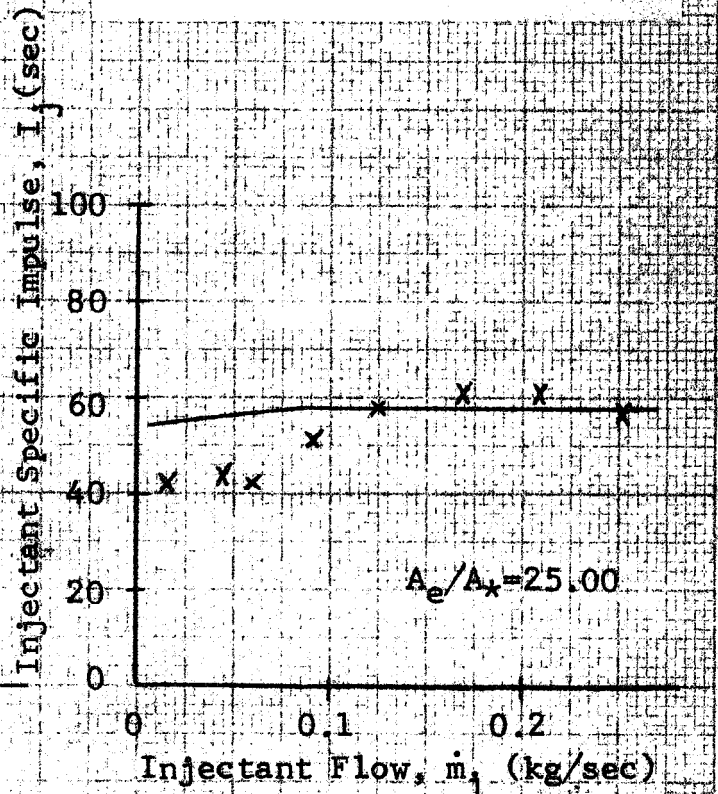
Fig. 3.33d Test 84 I=56 sec
ṁ=2.07 kg/sec P_e/P_a=0.07

Theoretical Full-Flowing Primary Exit Pressure, $\dfrac{P_e}{P_a}$ / Ambient Pressure
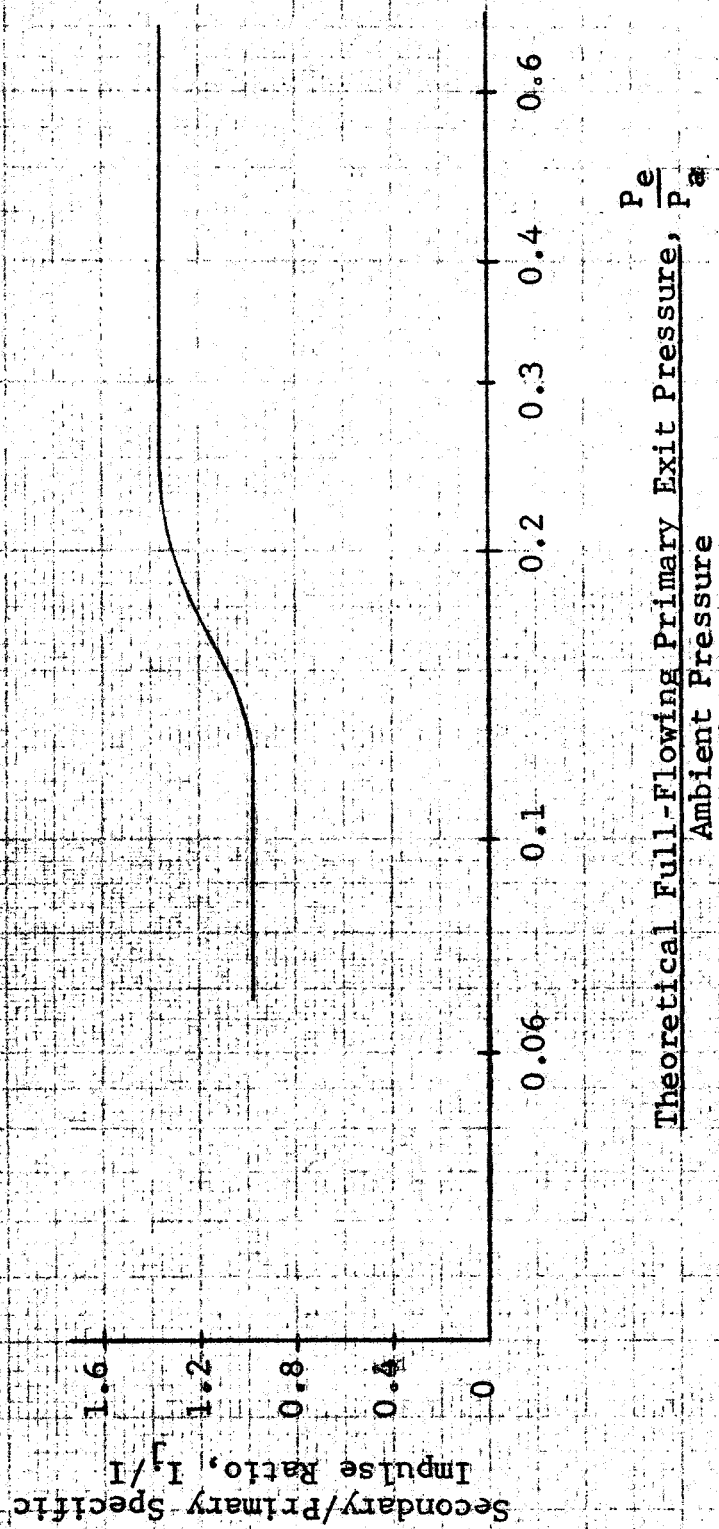
Figure 3.34 - Specific Impulse Characteristics For Single-Port Tests

SECTION 4

TEST RESULTS: SEPARATED-FLOW SHOCK STRUCTURE

4.1   Schlieren Tests

A two-dimensional model of gaseous SITVC was tested in the
Schlieren system shown in Figure 4.1. Design parameters and
Schlieren test outline are given in Figure 4.2. Photographs
of the sixteen test conditions appear in Figures 4.3 through
4.6. Test conditions 1 through 4 (Figure 4.3) correspond to
the flow structure occurring in the three-dimensional primary
nozzle extension 1. As the primary chamber pressure in the
Schlieren system is lowered, the degree of overexpansion of
primary nozzle extensions 2, 3, and 4 is simulated by test
conditions 5-8, 9-12, and 13-16 respectively. In test con-
ditions 13 through 16 (Figure 4.6), however, some problems
with the primary stream were encountered. When primary chamber
pressure becomes as low as it did in this case (less than six
times ambient), the flow stream in the diverging portion of the
nozzle tends to become unstable and non-symmetric. As a re-
sult, the photographs in Figure 4.6 do not present a true
representation of the flow structure of three-dimensional pri-
mary nozzle extension 4.

From measurements made on the Schlieren photographs for test conditions 1 through 12, a plot of accommodation height versus secondary/primary flow ratio is presented in Figure 4.7. Plots of secondary injection boundary layer separation point and the opposite wall separation point versus secondary/primary flow ratio are presented in Figure 4.8. Finally, shock angle measurements are given in Figure 4.9. Some observations can be made from these plots:

1. Accommodation heights for full-flowing or slightly over-expanded nozzles vary almost linearly with secondary flow rate.

2. With greater overexpansion, accommodation height is non-linear and significantly larger than for the full-flowing conditions.

3. Secondary injection boundary layer separation point moves slightly upstream with increased injection flow and with increased primary nozzle overexpansion.

4. The distance from the injector centerline to the secondary injection boundary layer separation point is more than double the accommodation height.

5. Flow separation point as observed on the wall opposite the injector moves downstream with increase of injected flow due to flow augmentation effects.

6. Shock angle increases slightly with increased injection flow and increases more significantly with increase in primary nozzle overexpansion

4.2 Shock Patterns

In each of the four primary nozzle extensions used in three-dimensional testing, ten pressure taps were drilled into the nozzle wall around one of the injection ports. Three were located directly upstream of the injection port, three in the radial plane through the injection ports, and four in a plane 0.1 inch (0.0019 meter) from the primary nozzle exit. These locations are tabulated in Figure 4.10.

The pressure taps were used to determine the shock outline on the nozzle wall. Figures 4.11 through 4.14 show the patterns produced in the four extensions. Each figure contains a full-scale development of the nozzle cone. Nominal primary flow conditions for all cases are 2.7 kg/sec flow rate and 4.2 x 10^6 newtons/meter^2 (600 psi) primary chamber pressure. For reference, the calculated location of 8 psia (55,200 nsma)

static wall pressure for a full-flowing primary nozzle is shown for extensions 2, 3, and 4. The shock patterns produced for three different secondary flow rates are shown on each development.

When the shock azimuths fall beyond the pressure taps near the instrumented port, the azimuths are located by using data obtained with the given flow rate coming from the opposite port.

Cross-plots of the shock apex locations and exit plane shock azimuths versus $\dot{m}_j$ are provided in Figures 4.15 and 4.16 respectively. Figure 4.15 correlates with the Schlieren observations in that the secondary injection boundary layer separation point moves upstream with increased injection flow and with increased primary nozzle overexpansion. Similarly, the Φ_e characteristics of Figure 4.16 support the Schlieren data regarding variation of shock angle with injected flow and overexpansion. Some other general statements can also be made in regard to the exit plane shock azimuth:

1. Under many test conditions, Φ_e exceeded 90°; therefore, some negative side force components were present.

2. At maximum $\dot{m}_j$ in extension 4, the shock from the

instrumented injection port seems to intersect with the opposite wall.

3. As degree of overexpansion increases, it becomes more difficult to determine exact shock patterns because of a tendency of the injected flow to spread out and "fill" the primary nozzle rather than create a sharply defined shock.

Further analysis of the shock pattern data in conjunction with the SITVC side force data of Section 3 is presented in Section 5.
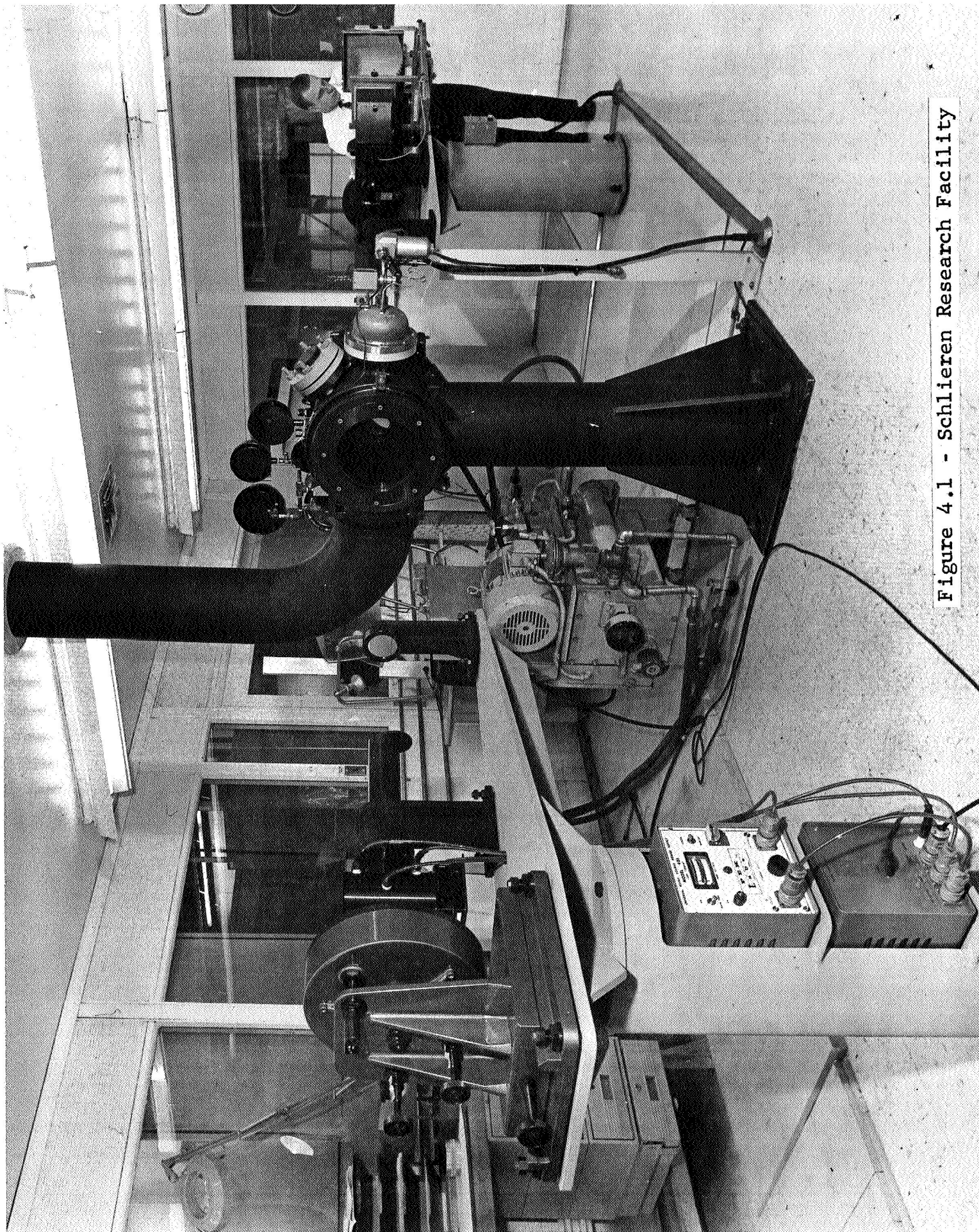
Figure 4.1 - Schlieren Research Facility

SCHLIEREN DESIGN PARAMETERS

PRIMARY NOZZLE

Half-cone angle = 15°
Exit/throat area ratio = 6.79   (Mach 3.5)

SECONDARY NOZZLE

Injection angle: perpendicular to primary axis
Injection position: primary nozzle X/L = 0.75
Throat area = 0.100 primary throat area
Half-cone angle = 15°
Exit/throat area ratio = 1.6875   (Mach 2)

SCHLIEREN TEST OUTLINE

Test Condition	Primary Chamber Pressure (10^3 nsma)	(psia)	Secondary Chamber Pressure (10^3 nsma)	(psia)	Resultant Secondary/Primary Flow Ratio
1	4140	600	----	---	0
2	4140	600	827	120	0.02
3	4140	600	2070	300	0.05
4	4140	600	4140	600	0.10
5	2080	301	----	---	0
6	2080	301	415	60.2	0.02
7	2080	301	1040	150.5	0.05
8	2080	301	2080	301	0.10
9	1090	158.6	----	---	0
10	1090	158.6	219	31.7	0.02
11	1090	158.6	547	79.3	0.05
12	1090	158.6	1090	158.6	0.10
13	596	86.5	----	---	0
14	596	86.5	119	17.3	≤ 0.02
15	596	86.5	298	43.25	0.05
16	596	86.5	596	86.5	0.10

FIGURE 4.2 - SCHLIEREN STUDY

1) $\dot{m}_j = 0$
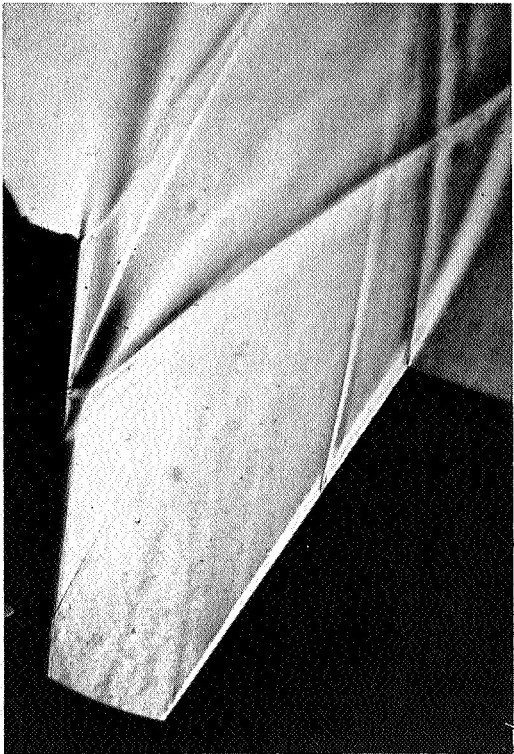
2) $P_{jc}/P_c = 0.20$; $\dot{m}_j/\dot{m} = 0.02$
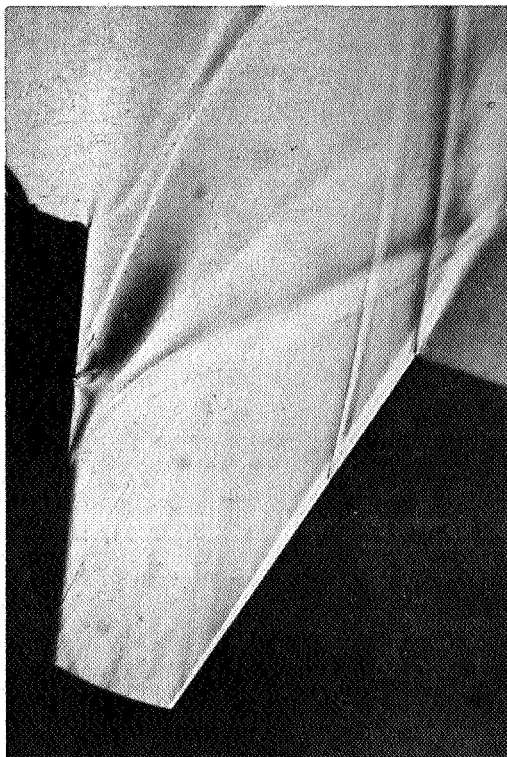
3) $P_{jc}/P_c = 0.50$; $\dot{m}_j/\dot{m} = 0.05$
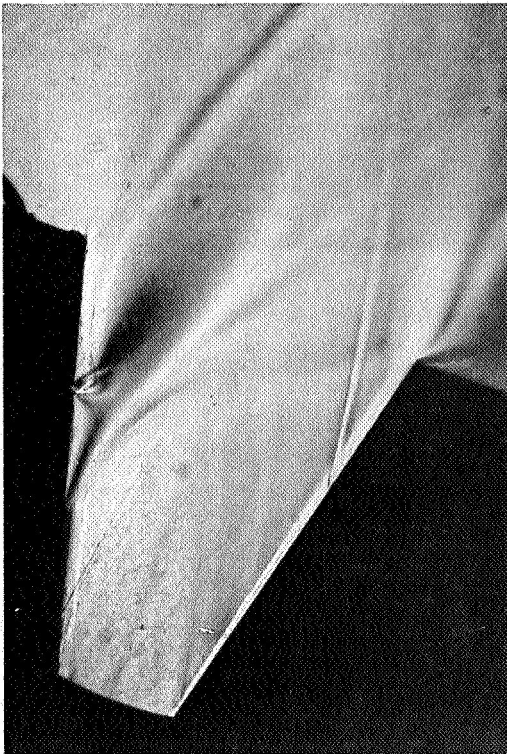
4) $P_{jc}/P_c = 1.00$; $\dot{m}_j/\dot{m} = 0.10$

$P_c = 4.14 \times 10^6$ nsma (600 psia

$P_e/P_a = 0.535$

FIGURE 4.3 SCHLIEREN PHOTOGRAPHS: TEST CONDITIONS 1 THROUGH 4
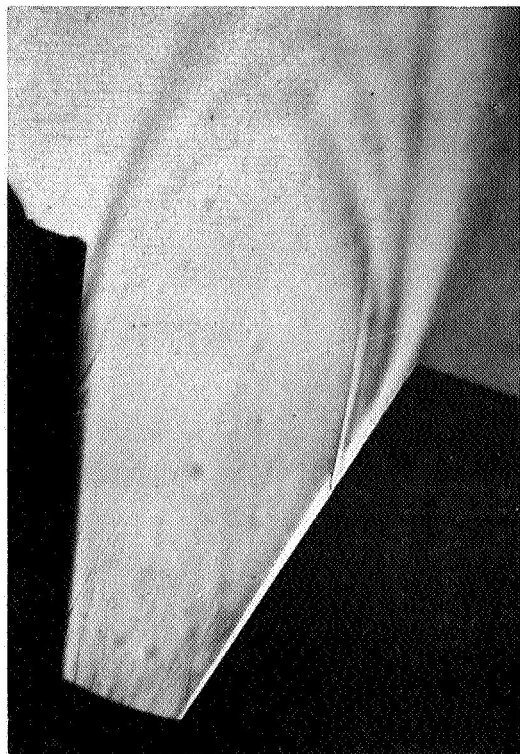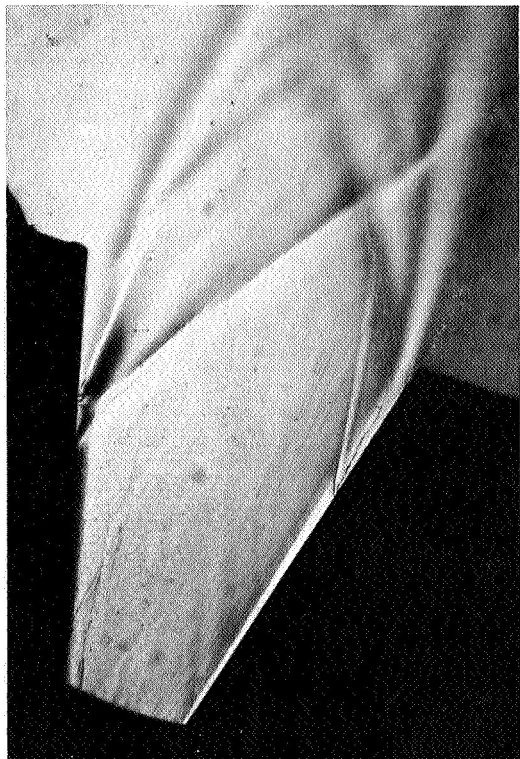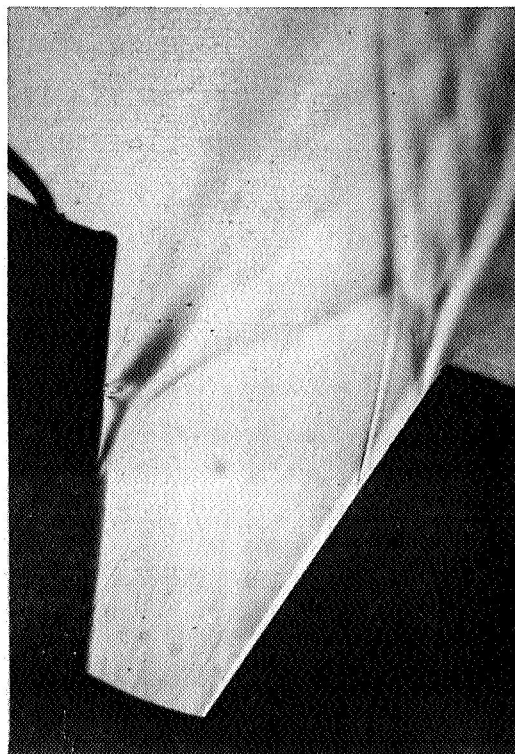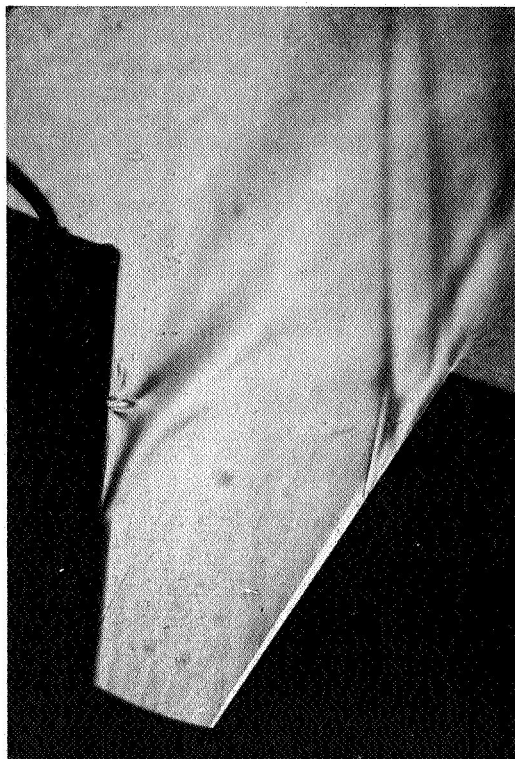
6) $P_{jc}/P_c = 0.20$; $\dot{m}_j/\dot{m} = 0.02$

8) $P_{jc}/P_c = 1.00$; $\dot{m}_j/\dot{m} = 0.10$

$P_c = 2.08 \times 10^6$ nsma (301 psia)

$P_e/P_a = 0.27$

5) $\dot{m}_j = 0$

7) $P_{jc}/P_c = 0.50$; $\dot{m}_j/\dot{m} = 0.05$

FIGURE 4.4 SCHLIEREN PHOTOGRAPHS: TEST CONDITIONS 5 THROUGH 8
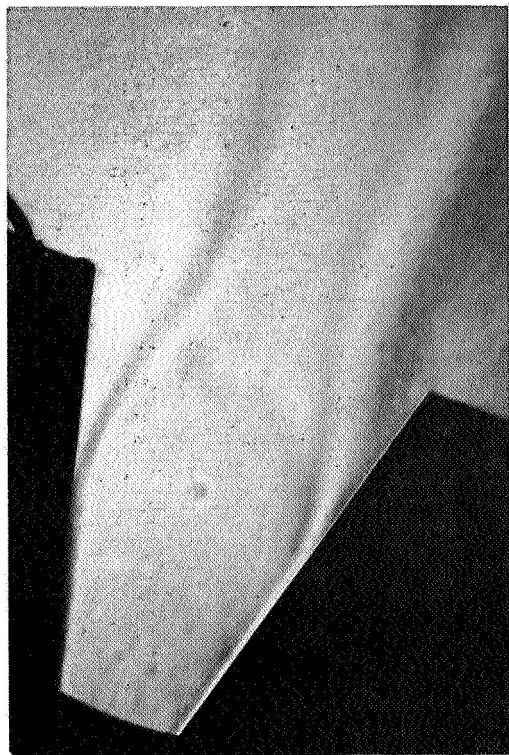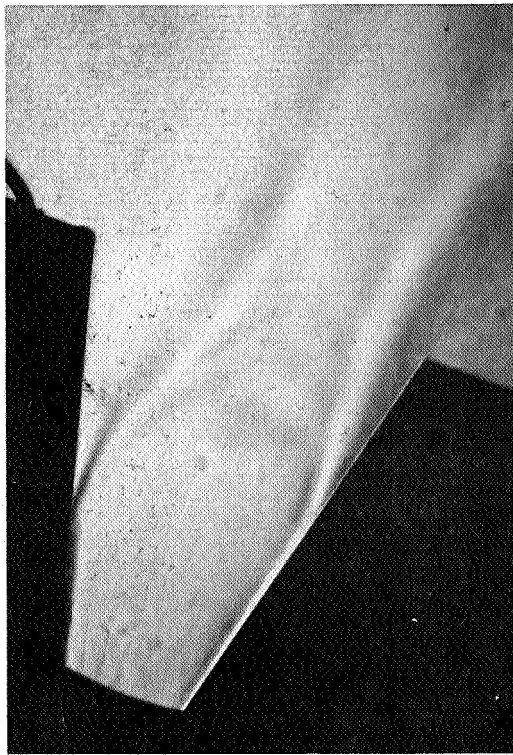
10) $P_{jc}/P_c = 0.2$; $\dot{m}_j/\dot{m} = 0.02$

12) $P_{jc}/P_c = 1.00$; $\dot{m}_j/\dot{m} = 0.10$

$P_c = 1.09 \times 10^6$ nsma (158.6 psia.

$P_e/P_a = 0.14$

9) $\dot{m}_j = 0$

11) $P_{jc}/P_c = 0.50$; $\dot{m}_j/\dot{m} = 0.05$

FIGURE 4.5 SCHLIEREN PHOTOGRAPHS: TEST CONDITIONS 9 THROUGH 12

14) $P_{jc}/P_c = 0.2$; $\dot{m}_j/\dot{m} \overset{<}{=} 0.02$
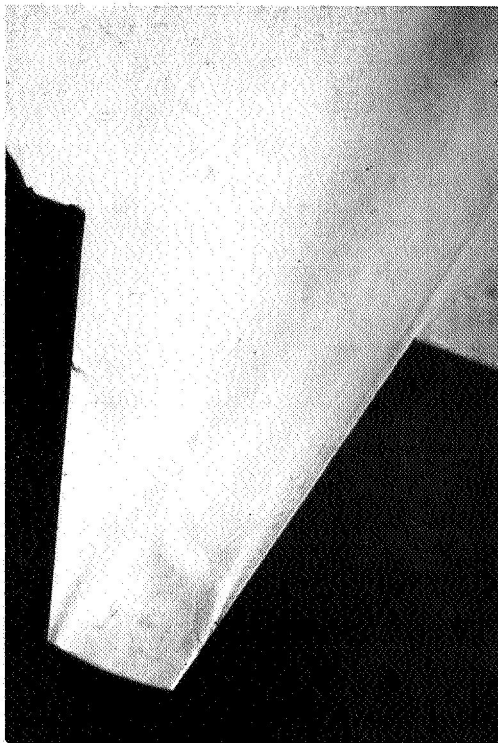
16) $P_{jc}/P_c = 1.00$; $\dot{m}_j/\dot{m} = 0.10$

$P_c = 0.596 \times 10^6$ nsma (86.5 psia)

$P_e/P_a = 0.08$

13) $\dot{m}_j = 0$

15) $P_{jc}/P_c = 0.5$; $\dot{m}_j/\dot{m} = 0.05$

FIGURE 4.6 SCHLIEREN PHOTOGRAPHS: TEST CONDITIONS 13 THROUGH 16

P_e/P_a	Symbol	Schlieren Test Conditions	Comparable Three-Dimensional Primary Nozzle Extension
0.535	⊙	1-4	1
0.27	▫	5-8	2
0.14	⬡	9-12	3
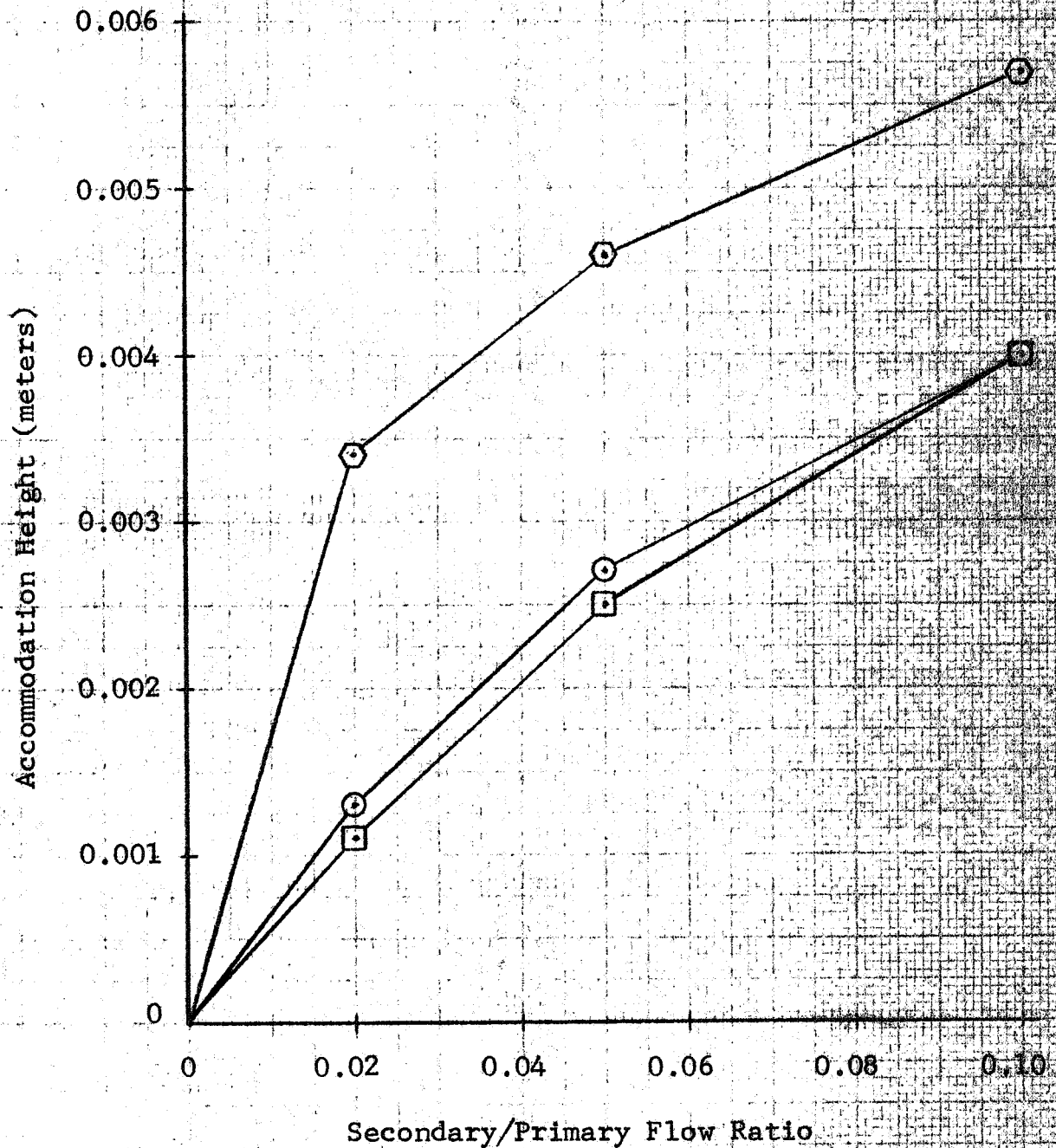
Figure 4.7 Schlieren Accommodation Height Versus Flow Ratio
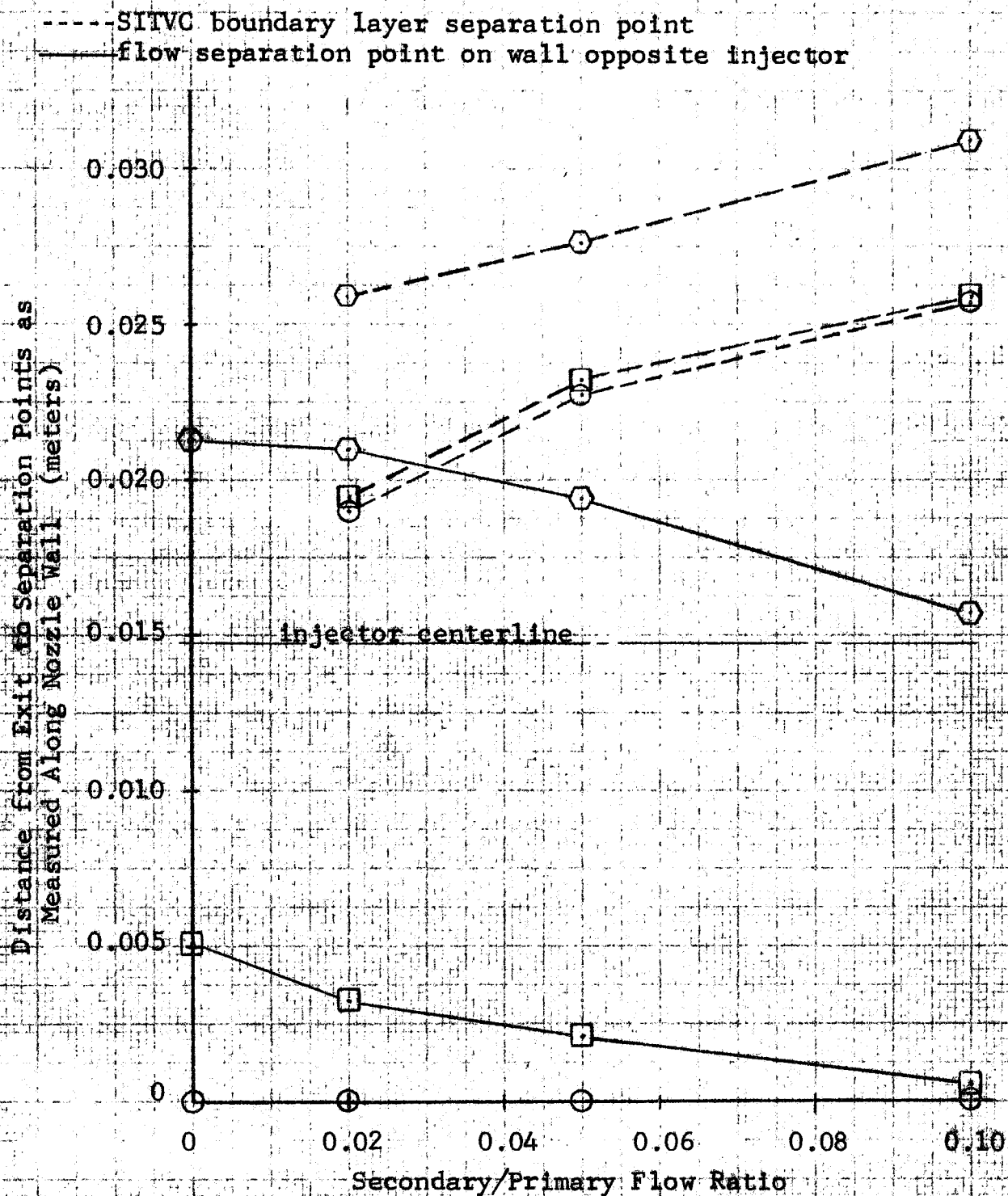
Figure 4.8 Schlieren Separation Points Versus Flow Ratio
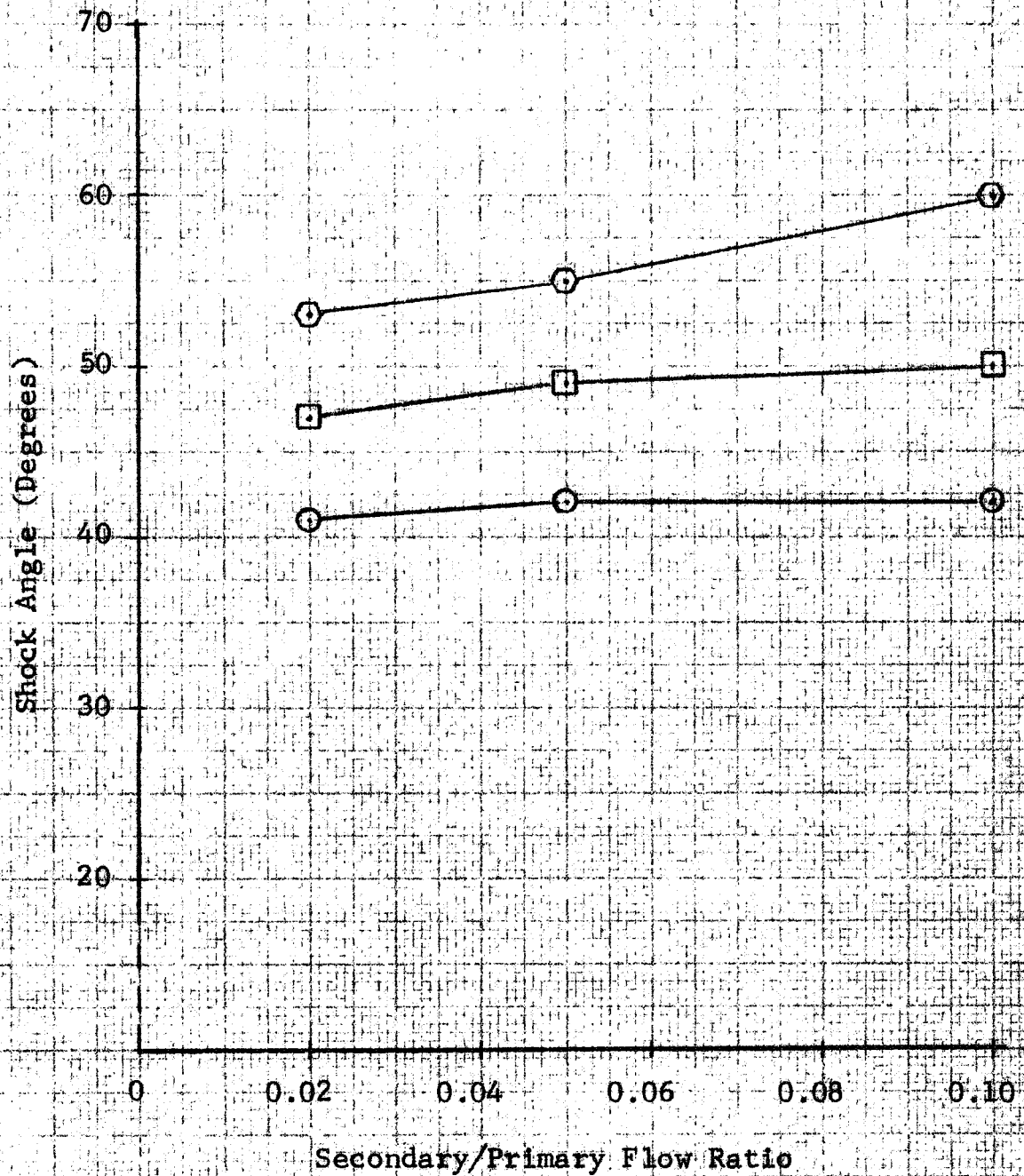
Figure 4.9 Schlieren Shock Angle Versus Flow Ratio

Pressure Tap No.	Azimuth	Nozzle Extension 1 Distance (meter)	Nozzle Extension 2 Distance (meter)	Nozzle Extension 3 Distance (meter)	Nozzle Extension 4 Distance (meter)
1	0°	+0.0190	+0.0314	+0.0371	+0.0429
2	0°	+0.0143	+0.0210	+0.0248	+0.0286
3	0°	+0.0095	+0.0105	+0.0124	+0.0143
4	30°	0	0	0	0
5	45°	0	0	0	0
6*	300°	0	0	0	0
7	330°	-0.0086	-0.0130	-0.0183	-0.0244
8	60°	-0.0086	-0.0130	-0.0183	-0.0244
9	285°	-0.0086	-0.0130	-0.0183	-0.0244
10	90°	-0.0086	-0.0130	-0.0183	-0.0244

Azimuths measured with respect to instrumented injection port.

Distances measured from injection plane parallel to primary axis; + represents upstream measurement, - downstream.

*Tap 6 in extension 1 is located at 305° azimuth.

Figure 4.10 Pressure Tap Locations
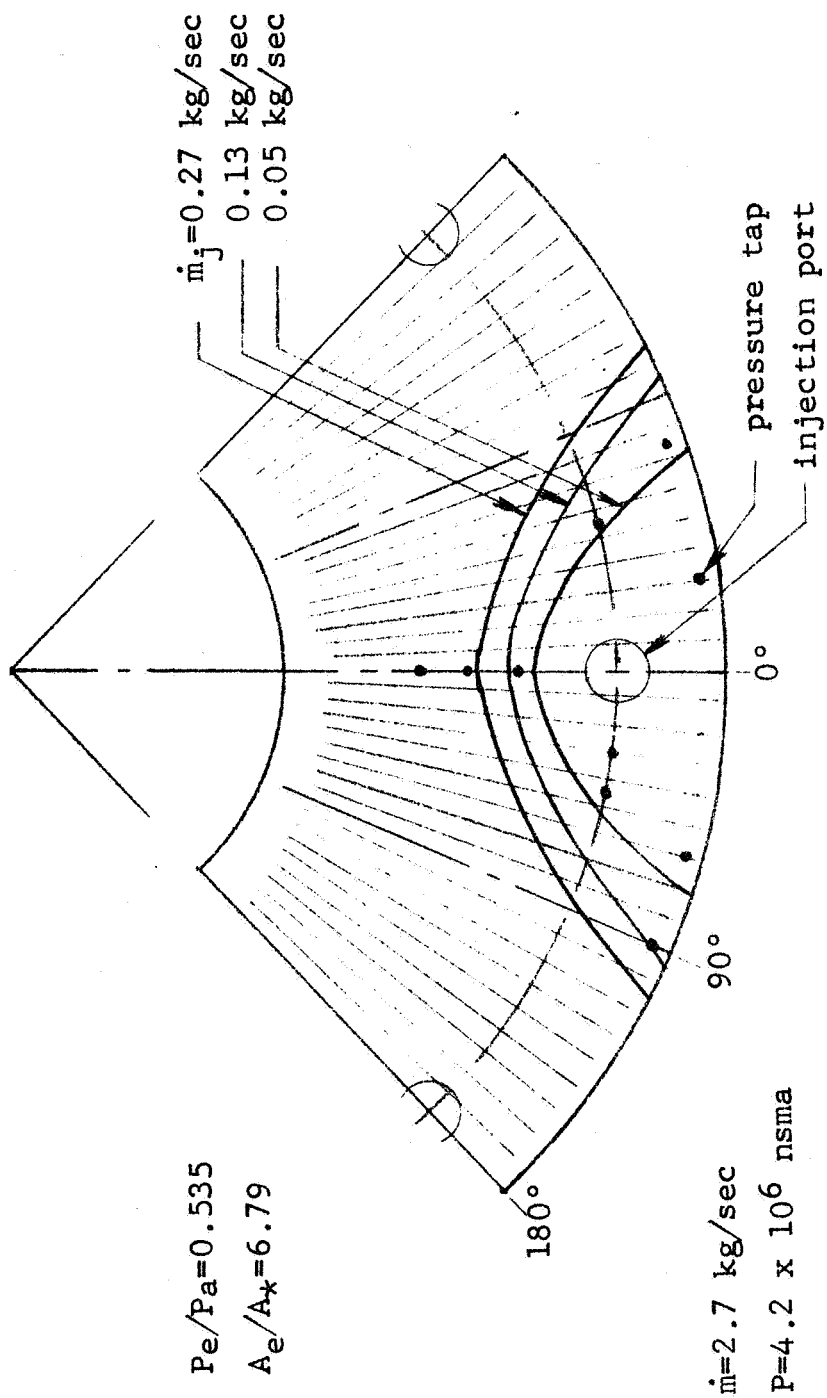
Figure 4.11 Extension 1 Shock Patterns

$P_e/P_a = 0.535$
$A_e/A_* = 6.79$

$\dot{m}_j = 0.27$ kg/sec
0.13 kg/sec
0.05 kg/sec

pressure tap
injection port

$0°$

$90°$

$180°$

$\dot{m} = 2.7$ kg/sec
$P = 4.2 \times 10^6$ nsma

$P_e/P_a = 0.27$

$A_e/A_* = 10.72$

$\dot{m}_j = 0.27$ kg/sec

0.13 kg/sec

0.05 kg/sec

55,200 nsma (8 psia)

0°

90°

180°

$\dot{m} = 2.7$ kg/sec
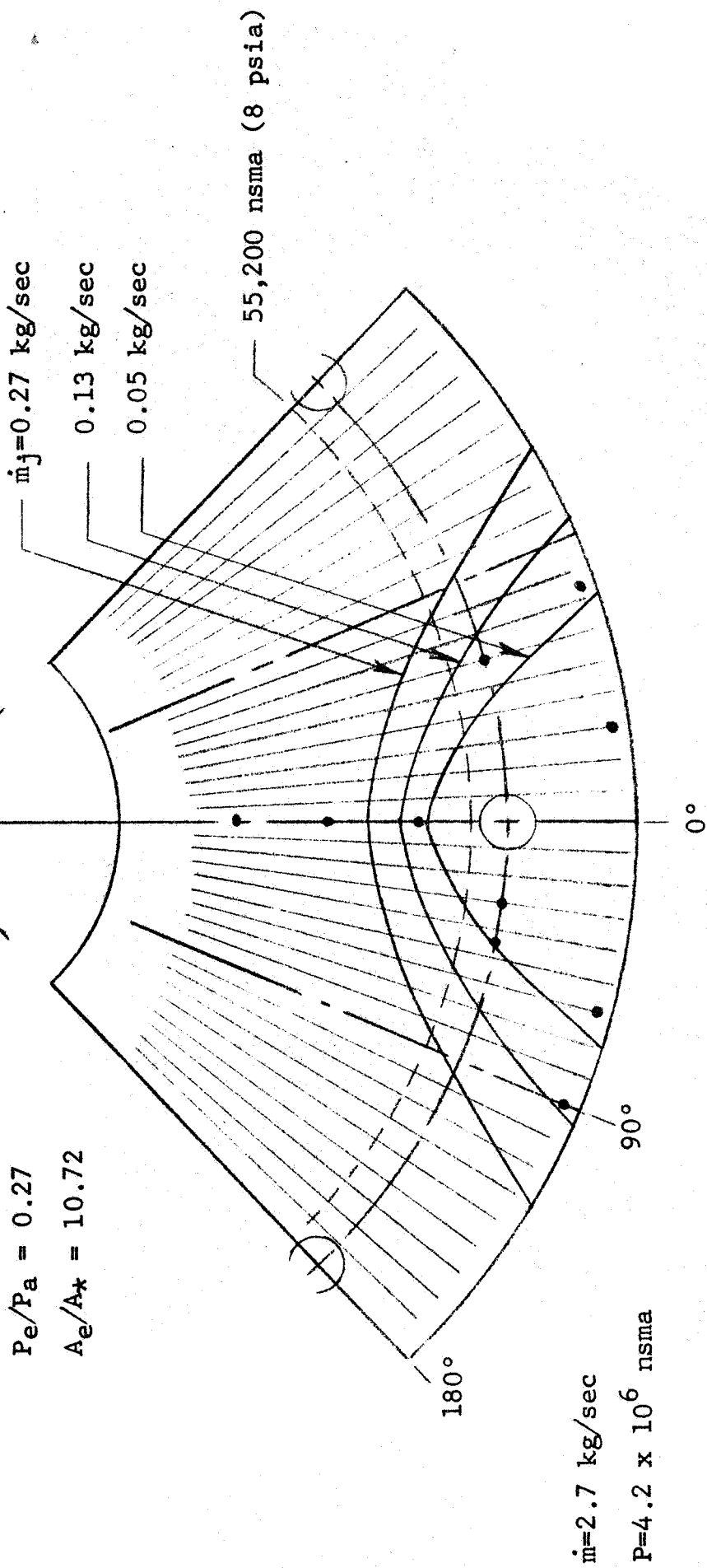
$P = 4.2 \times 10^6$ nsma

Figure 4.12 Extension 2 Shock Patterns

$\dot{m}_j = 0.27$ kg/sec

0.13 kg/sec

0.05 kg/sec

55,200 nsma (8 psia)

$\dot{m} = 2.7$ kg/sec

$P = 4.2 \times 10^6$ nsma

$P_e/P_a = 0.14$

$A_e/A_* = 16.56$

0°

90°

180°
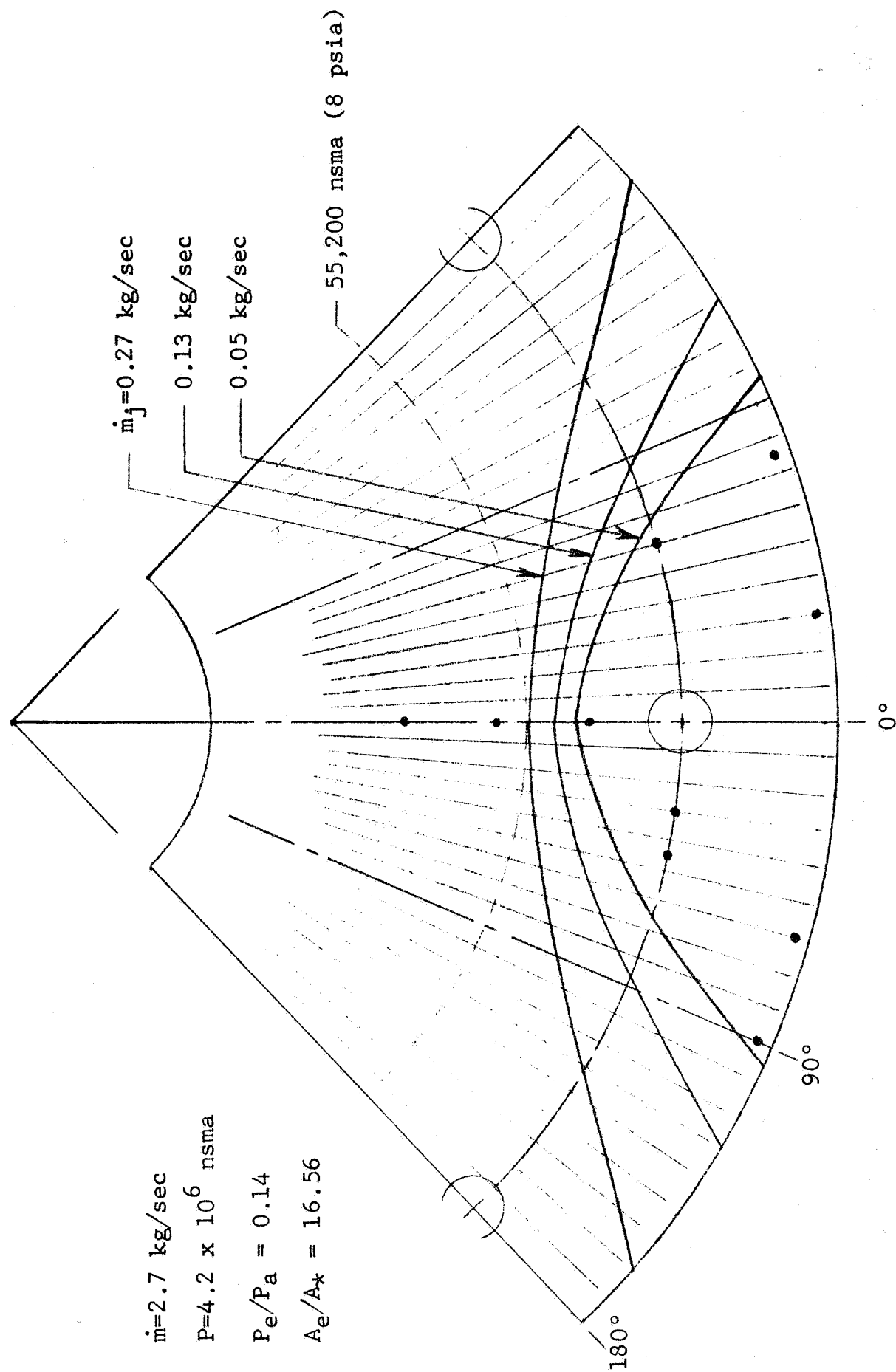
Figure 4.13 Extension 3 Shock Patterns

55,200 nsma (8 psia)

$\dot{m}_j=0.27$ kg/sec

0.13 kg/sec

0.05 kg/sec

$\dot{m}=2.7$ kg/sec

$P=4.2 \times 10^6$ nsma

$P_e/P_a = 0.08$

$A_e/A* = 25$

0°

90°

180°
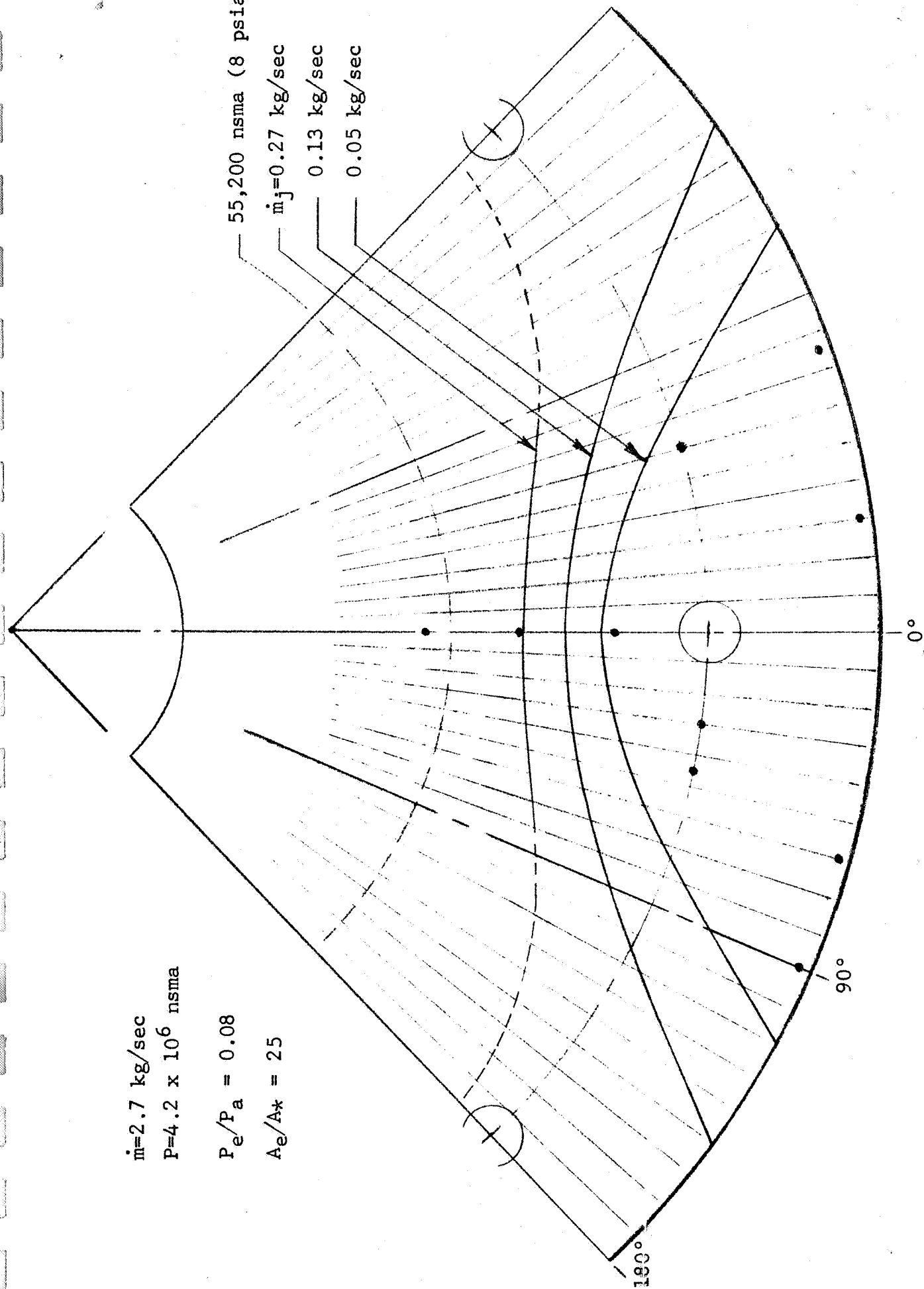
Figure 4.14 Extension 4 Shock Patterns

$\dot{m} = 2.7$ kg/sec

$P = 4.2 \times 10^6$ nsma

Exit Plane Shock Azimuth, Φ_e (Degrees)

Injector Flow Rate, $\dot{m}_j$ (kg/sec)

Figure 4.16 Exit Plane Shock
Azimuth Variation

P_e/P_a	A_e/A_*	Symbol	Extension
0.535	6.79	⊕	1
0.27	10.72	⊡	2
0.14	16.56	⬡	3
0.08	25.00	△	4

Distance Upstream of Injection Port of
Boundary Layer Separation Point as
Measured Along Nozzle Wall (Meter)

Injector Flow Rate, $\dot{m}_j$ (kg/sec)

Figure 4.15 Boundary Layer Separation
Point Variation

SECTION 5

DISCUSSION OF SEPARATED-FLOW RESULTS

5.1 Test Results Versus Predicted Values

In reviewing the test results, the most important factor to be considered is the exit plane shock azimuth Φ_e. Predicted values of Φ_e given in Section 2.2 are lower than those obtained in the tests (see Figure 4.16). Specifically, the predicted values in all but the most extreme case of primary nozzle overexpansion are less than 90°. Experimental data show Φ_e to be greater than 90° in most cases. The efficiency of the oblique shock to amplify the thrust vectoring of the secondary jet decreases as Φ_e reaches 90°. When Φ_e is significantly greater than 90°, some of the excess pressures generated on the primary nozzle wall actually oppose the force created by the secondary jet.

Some effects of this can be seen in the individual test results presented in Section 3. Tests with extensions 1 and 2 sometimes show a small decrease in specific impulse at the higher flow rates. Extensions 3 and 4 almost invariably show decreasing I_j with increasing secondary flow. It is interesting to compare the relatively simple characteristics produced in single-port testing (Figures 3.31, 3.32, and 3.33) with the two-port

characteristics of Figures 3.1 through 3.18. In two-port testing, the flow from the opposed port tends to interact and create complex results under separated-flow conditions.

Some observations can be made in attempting to correlate predicted shock parameters, Schlieren photographs, and experimental shock outlines. The two-dimensional Schlieren data and the experimental data show qualitative agreement in all comparable areas. These two sources can be used together to evaluate the mathematical model and its predicted shock outline. This evaluation can be applied, for example, to the relative shape and size of the shock outline. The actual shock was wider than anticipated but its apex was not as far upstream as expected: these two factors can be verified by comparing the shock locations of Figures 4.11 to 4.14 relative to the pressure taps which were to pick up the shock outline. It is interesting to note that the calculated values of accommodation height h presented in Section 2.1 are almost identical to the values for shock apex location provided by the test results of Figure 4.15. The Schlieren data of Section 4.1, however, indicated that the distance from injector centerline to shock apex was approximately double the accommodation height. The inference is that the injected nitrogen stream penetrated a lesser

distance into the primary stream than predicted by the half-circle approximation for secondary flow area A_4 of the mathematical model. Consequently, the secondary flow area must present a wider obstacle to the primary stream and cause a larger effective shock angle along the wall. This explains why the actual exit plane shock azimuth Φ_e was greater than predicted values for extensions 1 and 2.

In extensions 3 and 4, a somewhat different situation exists. The theoretical natural separation point of the primary stream is upstream of the shock apex. As the overexpansion condition becomes more extreme, the shock outline in fact becomes less clearly defined. The injected gas tends to fill in much of the region of the wall where the primary flow has separated from the wall. Consequently, the injected gas affects an even larger area within the primary nozzle, but it creates a relatively smaller change in the static pressures along the wall. The final result of this effect is a decrease in the injector thrust amplification produced by the shock mechanisms.

For all conditions tested in this program, the amplification of side force in the SITVC phenomenon is lower than predicted. The equation for theoretically determining side force (Section

2.3) predicted a specific impulse ratio of 1.68 (I_j/I = 104/62 = 1.68). Under full-flowing conditions obtained with extension 1, I_j/I = 86/62 = 1.39. With the separated flow conditions of extensions 2, 3, and 4, the specific impulse ratio diminishes to a level of approximately one.

For purpose of comparison, previous Vickers-NASA tests of normal (ε = 0°) warm gas injection into full-flowing hot gas primary streams produced a specific impulse ratio of 1.2. With a 20° injection angle, the specific impulse ratio for that system increased to 1.45. The data on injection angle presented in Section 6.2 of this report show that a specific impulse ratio of 2.0 can be achieved with cold gas injection into a cold gas primary stream.

Predicted and measured values of primary specific impulse are in agreement for the full-flowing conditions in extension 1. With the efficiency losses due to separated flow in the other extensions, primary specific impulse drops from 62 seconds to 56 seconds.

5.2 Review of NAS 1-4102 (Phase I) Results

As explained in Section 1.2, results obtained in contract NAS 1-4102 indicated an increase in secondary specific impulse

under separated-flow conditions. The present tests show a decrease. There is no reason to expect that the change in primary and secondary fluids would produce opposite effects. Instead, the cause of this apparent contradiction in test results is believed to be in the difference in test configurations.

The mixture of primary and secondary gases in the present tests was exhausted directly into the atmosphere. In the previous tests, however, an altitude cabin and diffuser were used to simulate altitude conditions. The diffuser entrance was placed approximately one centimeter from the primary nozzle exit. When the flow patterns produced by the injectors eroded the diffuser tube wall in critical areas, some of the flow leaving the primary nozzle escaped the diffuser and began to pressurize the cabin. It is now hypothesized that this escaping gas was the source of the increased thrust vector force.

Until results of the present tests showed that separated-flow SITVC itself does not produce magnified thrust vectoring forces, a different hypothesis had been developed to explain these magnified forces. Readings from pressure taps during the previous tests indicated a basic change in primary nozzle flow

pattern that suggested a "fluid amplifier" operation. It was
hypothesized that the injection port passing the larger amount
of flow "switched" the separated primary stream to the opposite
wall. Pressure taps near the injection port with greater flow
indicated a superposition of conventional shock pressures onto
ambient pressure whereas pressure taps on the opposite wall
indicated pressure expected of a full-flowing primary nozzle.
A technique of integrating the pressures on the nozzle wall
under both full-flowing and separated-flow conditions sub-
stantiated the increase in side force shown by the load cells
under separated-flow conditions.

These same static pressure characteristics can also be inter-
preted in a manner that supports the theory that escaping gas
produced the increase in side force. The static pressure
readings on the primary wall opposite the injector passing the
greater flow indicate that the primary stream was flowing
along that portion of the wall. Whenever gas escaped into the
altitude cabin, it was more likely to escape at this azimuth of
the primary nozzle exit and thus exert a reaction force on the
thrust stand in a direction the same as that intended with the
secondary injected gas. The pressure tap readings show the
location of this reaction force to be that portion of the

primary nozzle wall downstream of the injection port with the greater flow. In this affected area of the nozzle wall, the increase in static pressures relative to the pressures found under full-flowing conditions is uniformly distributed. The uniform level of pressure increase was of the same magnitude as the ambient pressure of the altitude cabin at that time. The fact that neither increased side force nor increased static pressures were found in the present series of separated-flow tests indicates that the static pressure increases superimposed on the shock pressures in the earlier tests were produced by reaction force of escaping gas rather than an intrusion of ambient pressure.

The original data had been examined for possible correlation between high TVC forces, escaping gas, and the rate of cabin pressurization. In the test performed January 12, 1966, at the Allegany Ballistic Laboratory, motion picture films taken through a window of the altitude cabin showed three definite occurrences of exhaust gas blowback into the cabin. Each of these three blowbacks was accompanied by both an increase in cabin pressure and a high TVC amplification factor. At no other time in this test did any cabin pressurization or high TVC forces occur. This evidence was weakened, however, by the

results of the two previous tests in the altitude cabin. In these tests, so much gas escaped into the cabin that smoke blocked the view of the test stand. The data did show that a rate of cabin pressurization such as 0.5 psi ($3450 \text{ n}/\text{m}^2$) per second was in general accompanied by side forces above those produced under design conditions of system operation. There were, however, situations of large side force without noticeable cabin pressurization. This was the key factor in the original belief that the side force increase was due to fluid amplifier effects rather than the escaping gas. The explanation is that the amount of gas sufficient to account for the maximum force increase would produce such a low pressurization rate—less than 0.02 psi ($138 \text{ n}/\text{m}^2$) per second—that it could not be read from the time plots of cabin pressure.

SECTION 6

OTHER TEST RESULTS

6.1 Frequency Response Tests

Tests 85, 86, and 87 determine the frequency response of the
SITVC fluid mechanism. Sinusoidal signals were applied to the
pneumatic valve at frequency intervals of five cps from five to
sixty cps. Figure 6.1 shows the results in terms of the side
force to differential injector chamber pressures ratio, $F_j/\Delta P_{jc}$,
relative to steady-state conditions. Testing was limited to
sixty cps due to the combined attenuation of the valve, gas
manifold volume between valve and injectors, and the fluid
mechanism itself. Some 25 and 30 cps data points were disre-
garded due to distortion in the chamber pressure sinusoidal
signals. The curve drawn through the given data points in
Figure 6.1 closely approximates the theoretical response of
a second order system with 40 cps resonance and 0.3 damping
ratio.

The above results are believed to be unaffected by thrust
stand dynamics. A simple check of thrust stand resonant fre-
quency was made by tapping the assembly at the injection plane.
The load cell traces on the oscillograph showed a resonant

frequency of 243 cps. Although some higher harmonics seemed to be superimposed, no frequencies below 243 cps could be detected.

The data obtained in previous contracts (NAS 1-4102 and NAS 1-2962; see references) indicated the SITVC fluid mechanism could be represented by a first-order transfer function with a corner frequency in excess of 35 cps. That testing, however, was performed on a thrust stand with a 25 cps resonant frequency. SITVC frequency response data were mathematically extracted from the load cell readings. The high amplitude ratio of measured side force to differential chamber pressures (as much as +25 decibels at 20 cps) was assumed entirely due to thrust stand resonance.

The positive decibels of SITVC frequency response encountered in the current tests were not expected; but no evidence that the positive frequency response was contributed by test or instrumentation components other than the SITVC fluid mechanism could be found. The possibility still remains, however, that some combination of the nitrogen supply system, primary and secondary hose stiffness when pressurized, secondary hose volume and configuration, and the location of the chamber pressure taps could have been responsible.

6.2 Varied Injection Angle Tests

The primary nozzle extension subassembly shown in Figure 6.2 was used to perform the varied injection angle tests. Geometry of the primary nozzle and the single injection nozzle is the same as that listed for extension 1 in Figure 1.1. The pivot point for the injector was placed as close as possible to the primary nozzle axis in order to maintain a relatively constant X/L ratio and to minimize the size of the hole required in the primary nozzle wall. The injector was set at eleven positions between -30° and 45° as tabulated in Figure 1.5. Results of the individual tests are given in Figures 6.3, 6.4, and 6.5. Figure 6.6 is a composite of all eleven tests.

Some observations can be made from these results:

1. At low flow rates in the extreme injection angle position—specifically -30°, $37\frac{1}{2}$°, and 45°—there may be some effect on injectant specific impulse produced by protrusion of an edge of the injector into the primary stream.

2. A decreasing specific impulse at high flow rates for $\varepsilon \geq 15°$ shows the degrading effect of having the exit plane shock azimuth exceed 90°.

3. An optimum injection angle based on specific impulse level, simplicity of assembly, and linearity of response appears to be $22\frac{1}{2}°$.

4. As the injection angle is turned upstream from 0° to 30°, the secondary specific impulse increases at a greater rate than the $1/\cos \varepsilon$ factor predicted in Section 2.3.
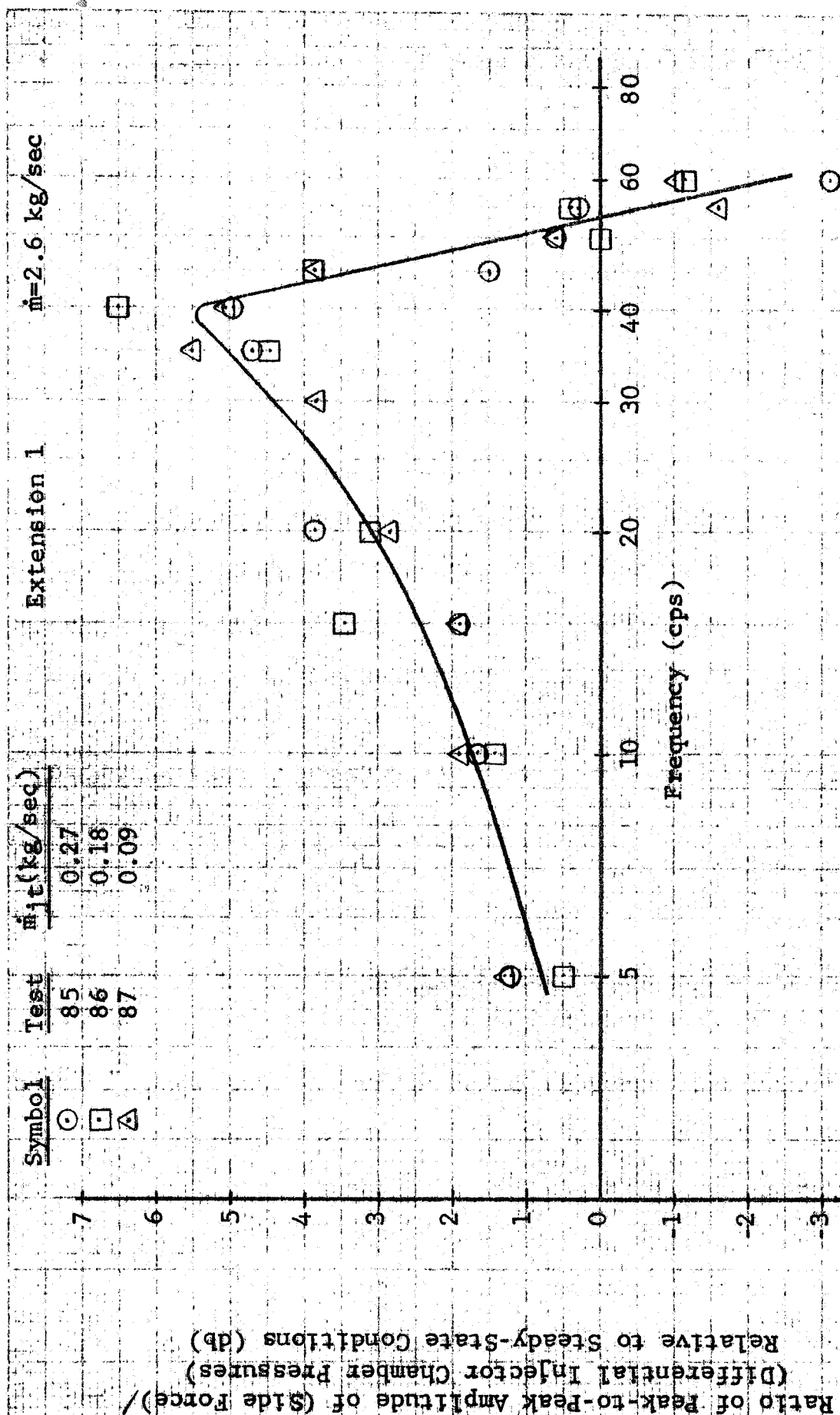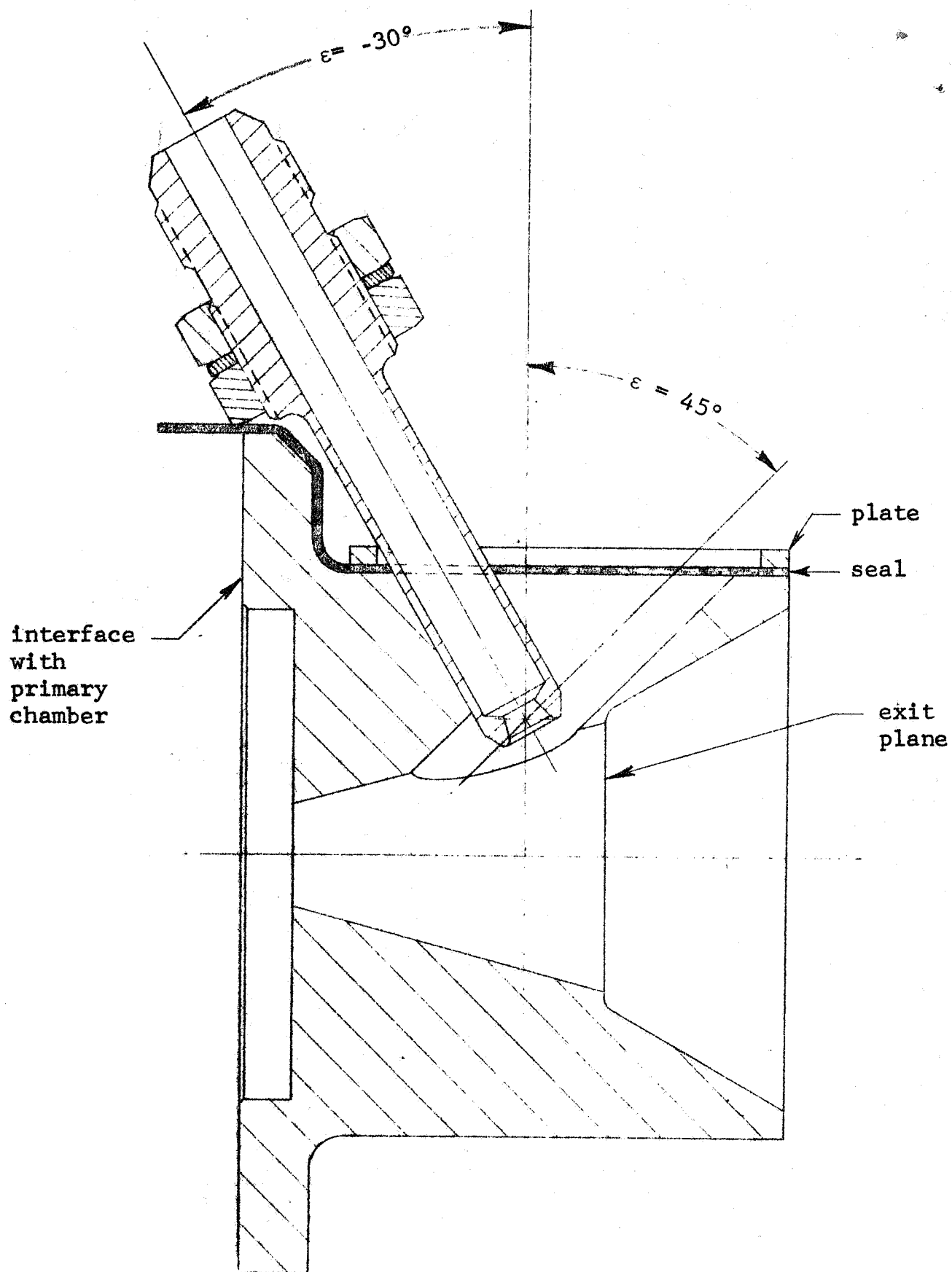
Figure 6.1 - SITVC Frequency Response

Figure 6.2   Full Scale Cross-Section of Primary Nozzle
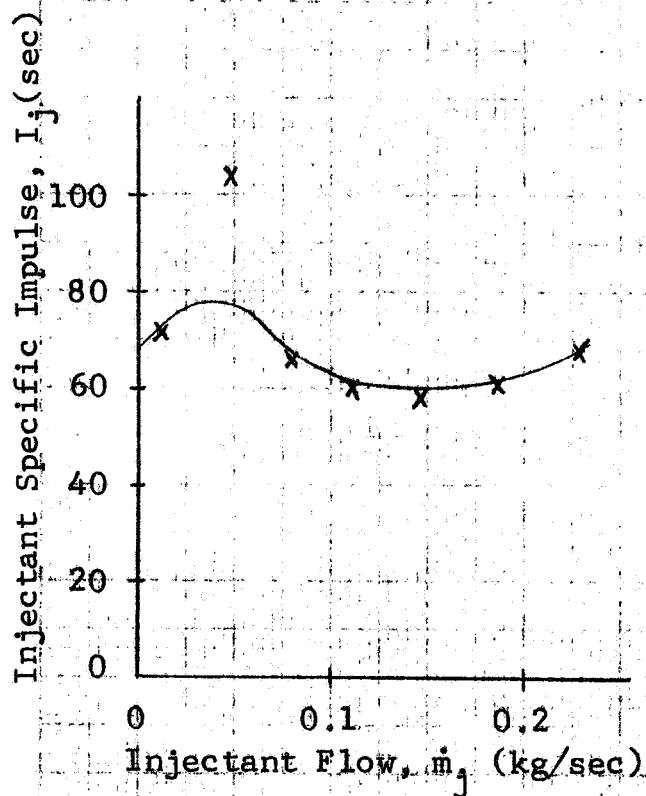Extension with Varied Injection Angle Subassembly

Figure 6.3a   Test 88
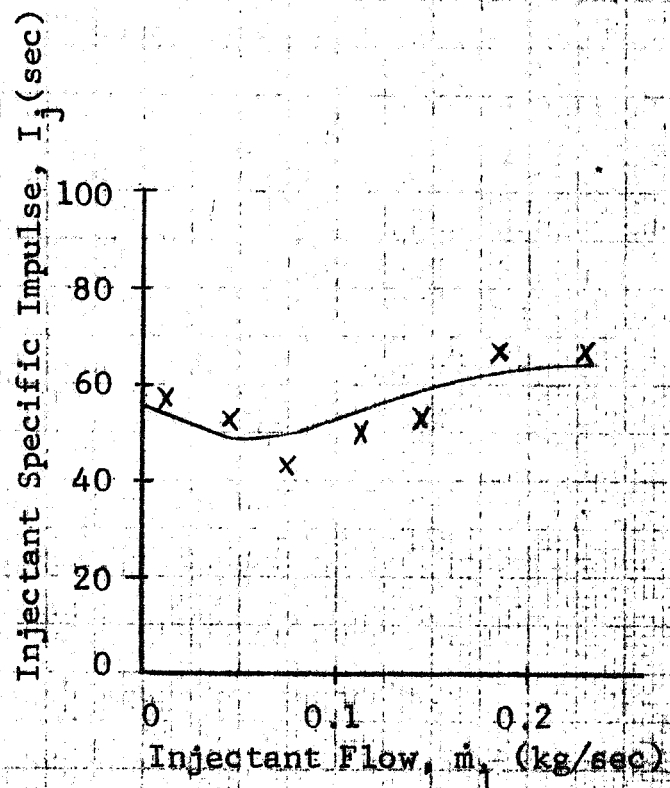$\dot{m}$=2.51 kg/sec ε= -30°
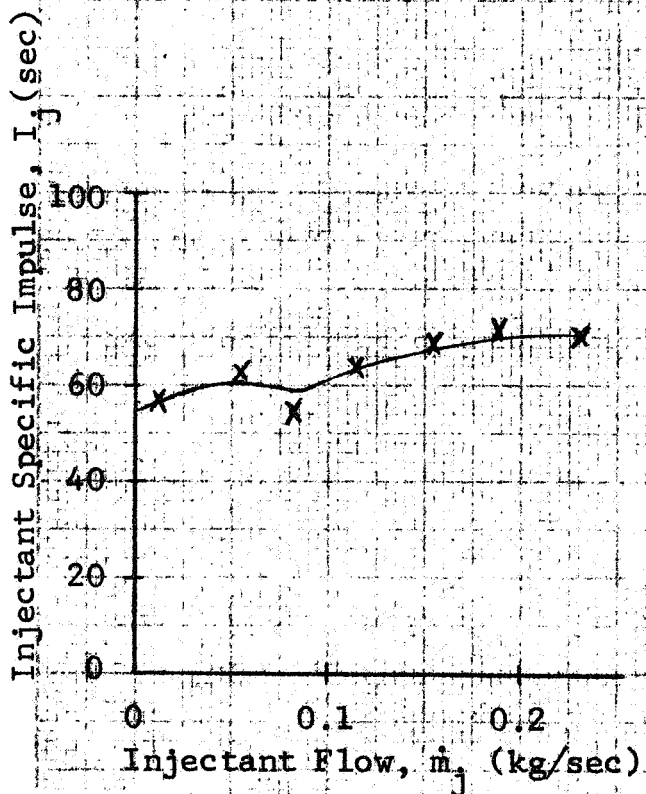
Figure 6.3b   Test 89
$\dot{m}$=2.60 kg/sec ε= -22½°

Figure 6.3c   Test 90
$\dot{m}$=2.60 kg/sec ε= -15°
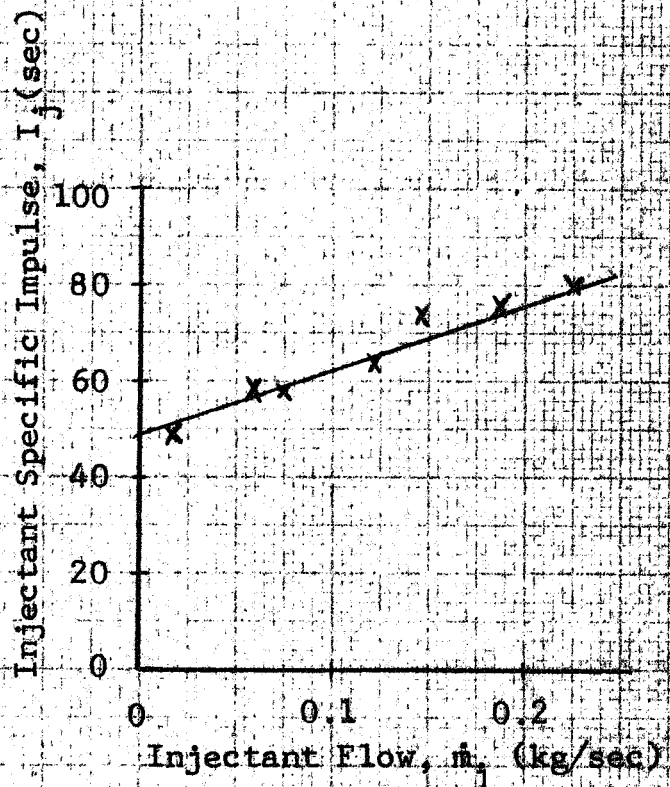
Figure 6.3d   Test 91
$\dot{m}$=2.46 kg/sec ε= -7½°
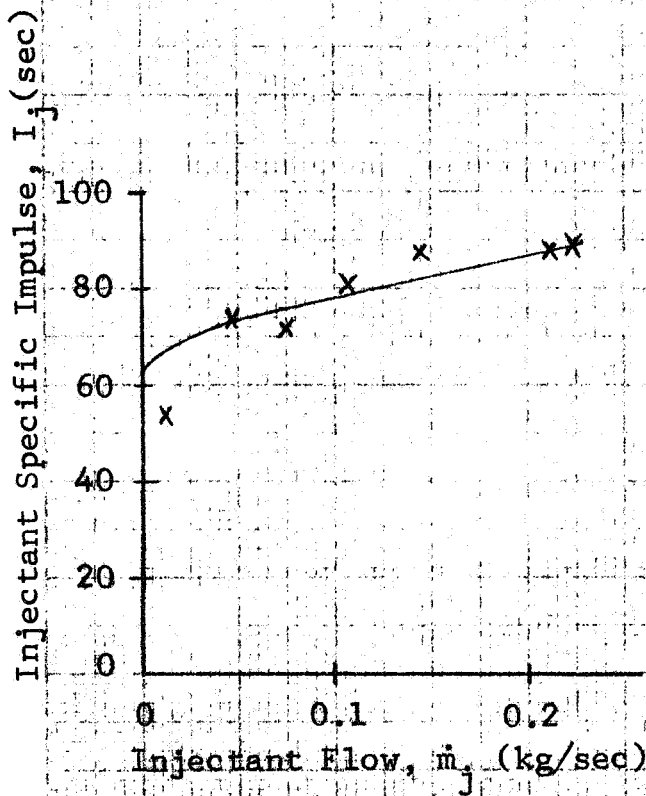
Figure 6.4a   Test 92
ṁ=2.24 kg/sec   ε= 0°
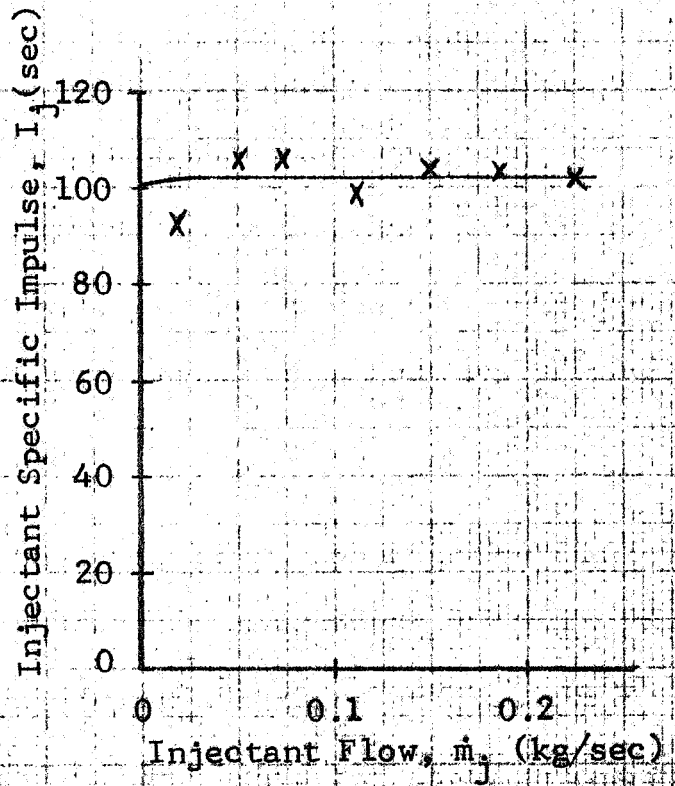
Figure 6.4b   Test 93
ṁ=2.45 kg/sec   ε= 7½°
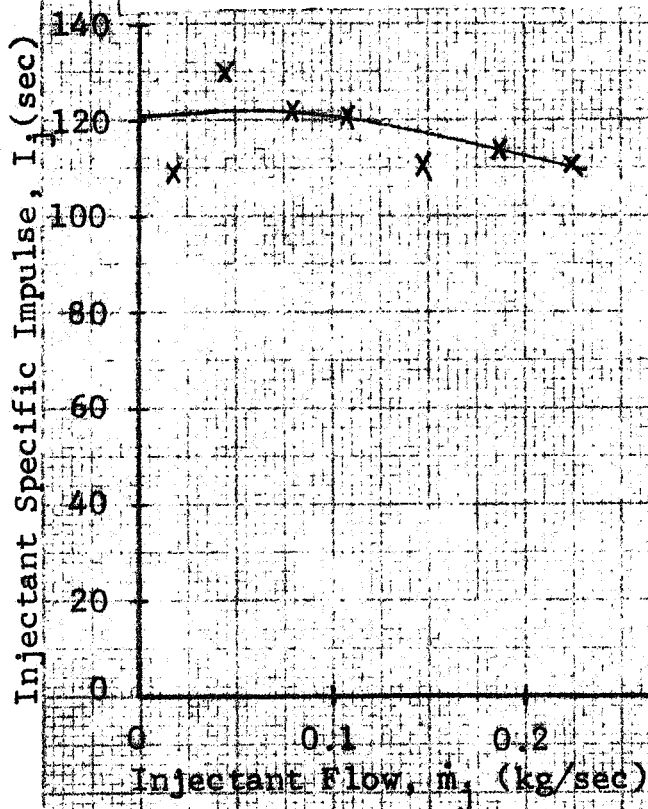
Figure 6.4c   Test 94
ṁ=2.65 kg/sec   ε= 15°
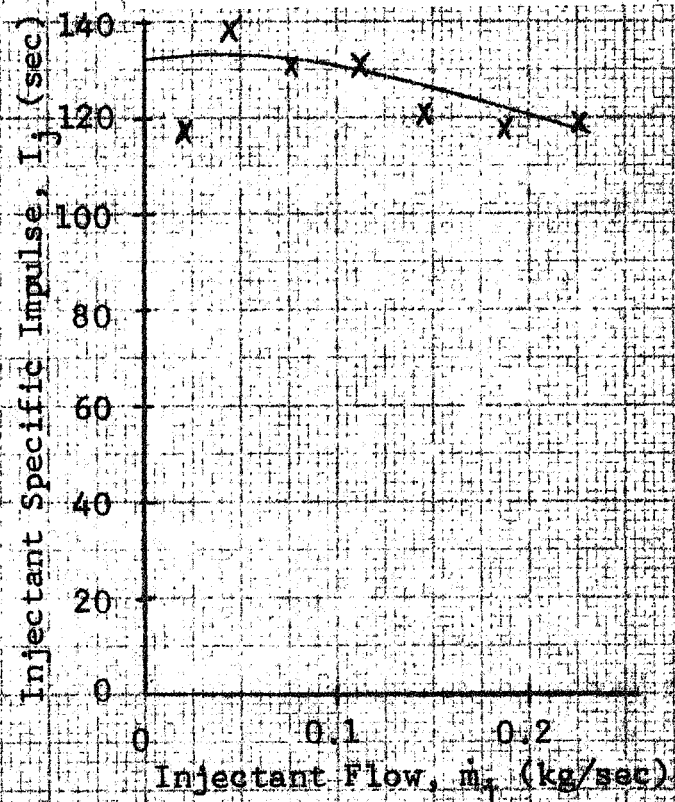
Figure 6.4d   Test 95
ṁ=2.51 kg/sec   ε= 22½°

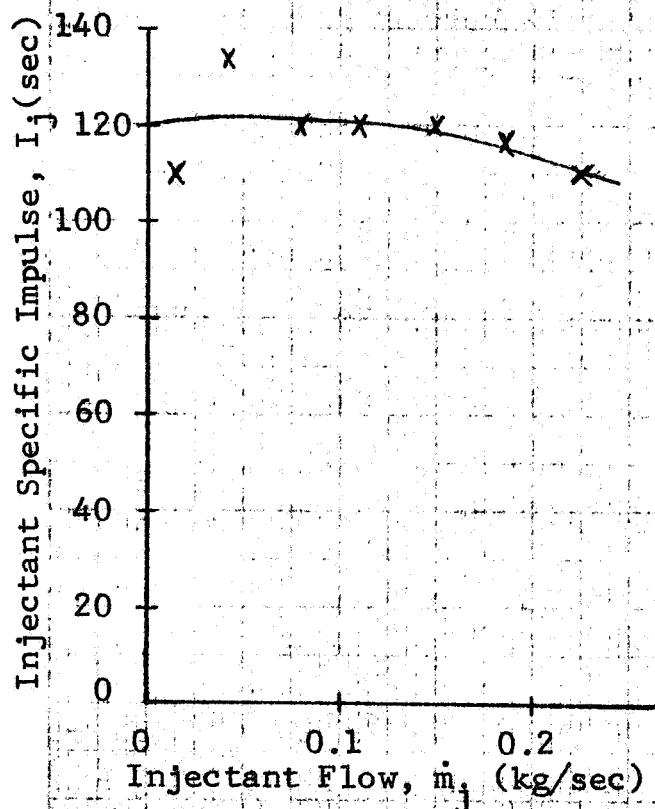Figure 6.5a   Test 96
$\dot{m}$=2.44 kg/sec ε= 30°
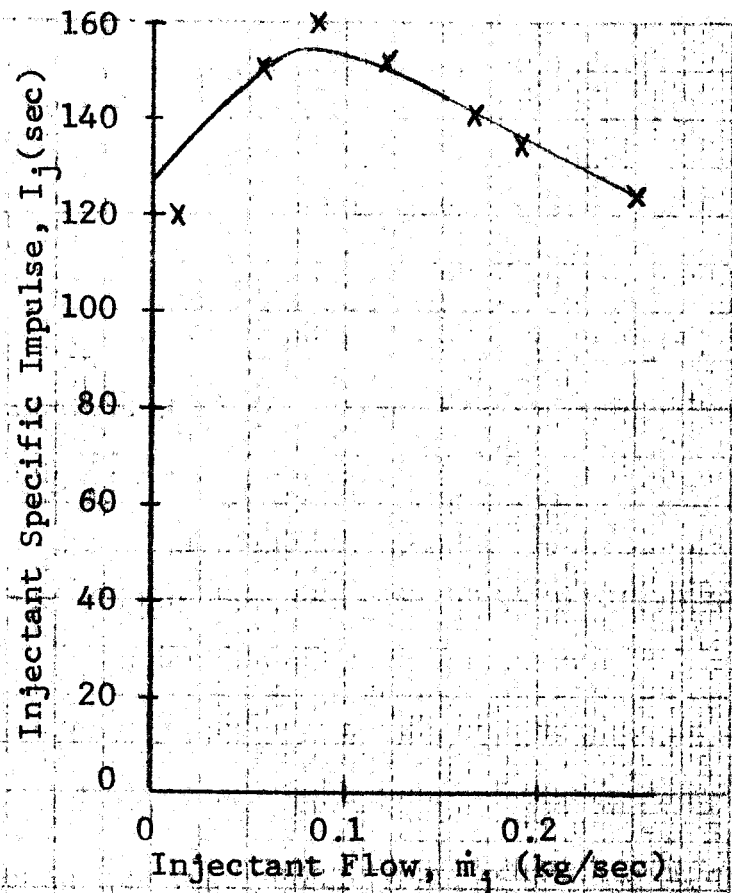
Figure 6.5b   Test 97
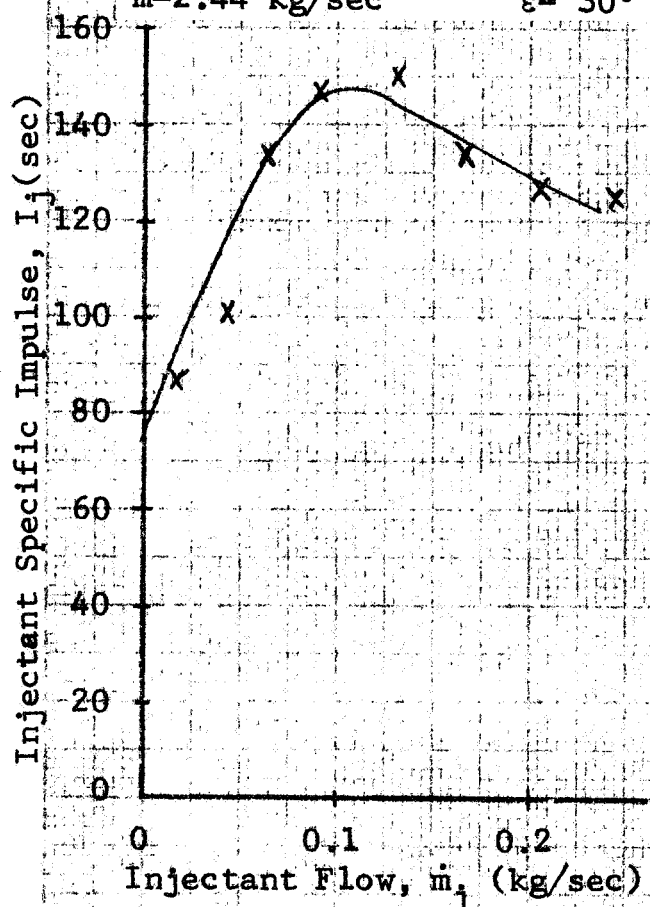$\dot{m}$=2.70 kg/sec ε= 37½°

Figure 6.5c   Test 98
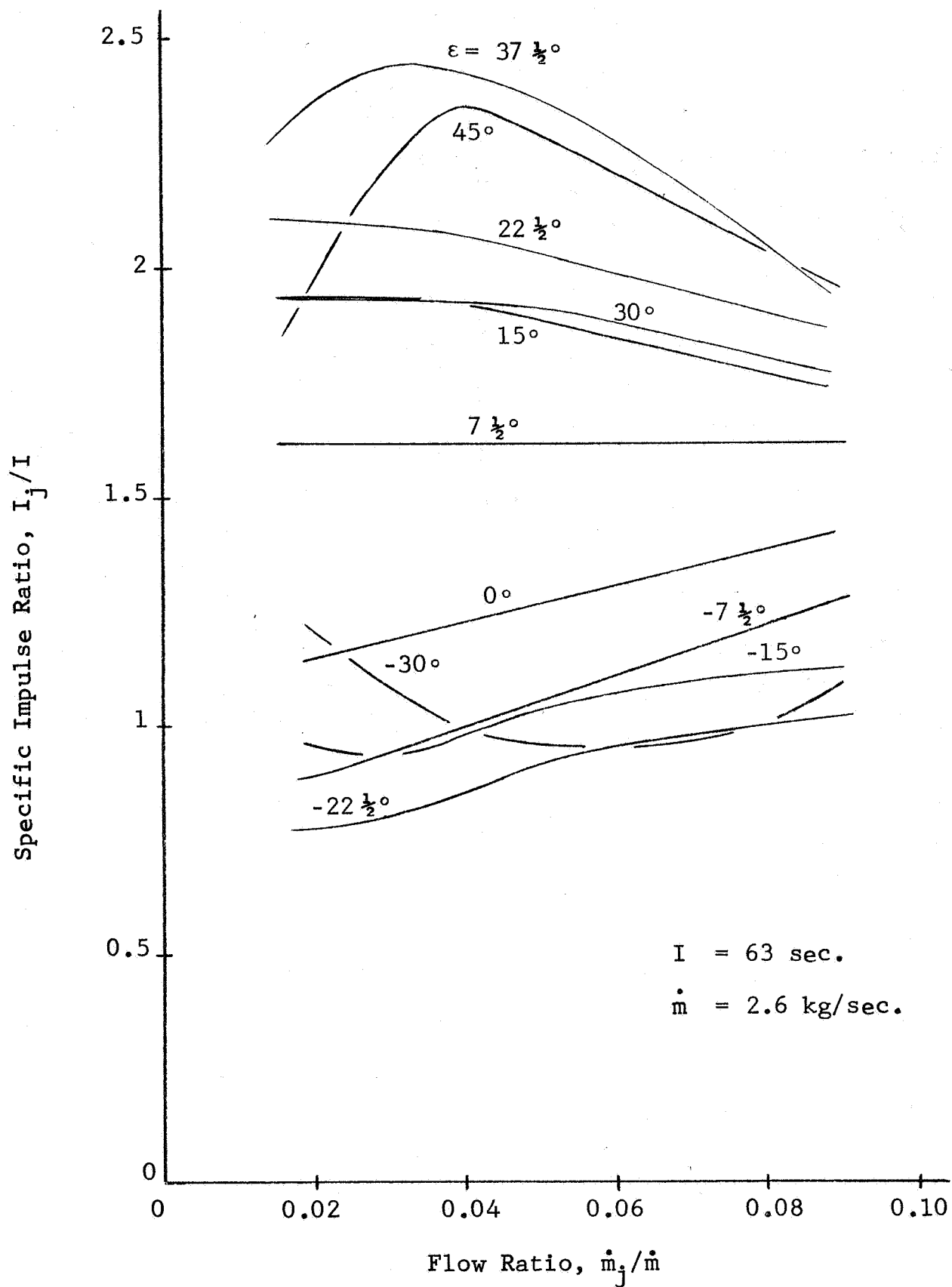$\dot{m}$=2.71 kg/sec ε= 45°

Figure 6.6 - Composite Results of Varied
Injection Angle Tests

SECTION 7

SUMMARY AND CONCLUSIONS

7.1 Separated-Flow SITVC

Test results with nitrogen gas in both primary and secondary

systems indicated a decrease in secondary specific impulse as the

primary nozzle expansion was increased to produce separated flow.

In all tests the secondary gas was injected normal to the pri-

mary nozzle axis at an X/L location of 0.75. When the secondary

injection came from one port only, secondary specific impulse

dropped from 86 seconds under full-flowing conditions to 52

seconds at the most extreme case of primary nozzle overexpansion

tested. When the injected gas came from two opposed injection

ports, nonlinear effects of shock wave interaction in the over-

expanded primary nozzle superimposed variations on the basic

results obtained with one port blocked.

In all conditions tested, and especially those with the greater

degree of flow separation, the effective shock azimuth at the

primary nozzle exit was larger than the value predicted by a

mathematical model. In fact, the exit plane shock azimuth

frequently exceeded 90° and caused a deterioration in the SITVC

amplification factor. In order to reduce the exit plane shock

azimuth, the injection ports should be located closer to the primary nozzle exit.

The salient conclusion derived from these tests is that gaseous secondary injection into an overexpanded primary nozzle does not produce sufficient side force amplification to compensate for the additional weight of the overexpanded nozzle. If the design of such a system is under consideration, however, the data cross-plots presented in Figures 3.19 through 3.30 and Figure 3.34 provide sufficient information for estimating the TVC force produced over a wide range of secondary flow and primary overexpansion conditions.

7.2 Frequency Response

A primary nozzle with sea-level expansion was tested with sinusoidal variation of the flow from opposed injection ports. The SITVC frequency response curve of Figure 6.1 indicates a second order system with 40 cps resonant frequency and 0.3 damping ratio.

7.3 Varied Injection Angle

A primary nozzle with sea-level expansion was tested at $7\frac{1}{2}°$ intervals of injection angle between 30° downstream and 45° upstream. Composite results are given in Figure 6.6. Of the

angles tested, an optimum injection angle based on specific impulse level, simplicity of assembly, and linearity of response appears to be $22\frac{1}{2}°$ upstream.

LIST OF REFERENCES

Ames Research Staff, "Equations, Tables, and Charts for Compressible Flow," NACA TR-1135, 1953.

Charwat, A. F., and Allegre, J., "Interaction of a Supersonic Stream and a Transverse Supersonic Jet," AIAA Journal, November, 1964, Volume 2, No. 11, pages 1965-1972.

Guhse, R. D., "An Experimental Investigation of Thrust Vector Control by Secondary Injection," NASA CR-297, September, 1965.

Hammit, A. G., and Murthy, K.R.A., "Approximate Solutions for Supersonic Flow Over Wedges and Cones," AFOSR TN59-304, Rep. 449 Princeton University, April, 1959.

Kallis, J. M., and Adelberg, M., "Recent Advances in the Fluid Dynamics of Gas Injection for Thrust Vector and Trajectory Control (u)," CPIA Publication 18A, AD 346945 Bulletin of the Interagency Solid Propulsion Meeting, July, 1963, pages 341-389, Confidential.

Smith, G. L., "Vortex Flow and Erosion in Rocket Nozzles Due to Warm-Gas Injection for Thrust Vector Control," NAS TN D-3241, Langley Research Center, February, 1966.

Vickers Division, Sperry Rand Corporation, "Proportional Solid Propellant Secondary Injection Thrust Vector Control Study," NASA CR-637, November, 1966.

Vickers Division, Sperry Rand Corporation, "Study of Proportional Solid Propellant S.I.T.V.C. Under Simulated Altitude Conditions," Contract No. NAS 1-4102 (Phase 1), June, 1966.

Vickers Division, Sperry Rand Corporation, "Analytical and Experimental Study of Altitude Compensation of a Rocket by Secondary Injection," NASA Contract No. NAS 1-4102 (Phase 2), June, 1966.

Wu, J. M., Chapkis, R. L., and Mager, A., "Approximate Analysis of Thrust Vector Control by Fluid Injection," ARS Journal, December, 1961, pages 1677-1685.